University of Alberta

Halogen and Stable Chlorine Isotope Analysis of Quartz Hosted Fluid Inclusions from Porphyry Cu Deposits

by

Taras Julian Nahnybida 

A thesis submitted to the Faculty of Graduate Studies and Research in partial fulfillment of the requirements for the degree of Master of Science

Department of Earth and Atmospheric Sciences

Edmonton, Alberta

Fall, 2006

Your file Votre référence
ISBN: 978-0-494-22330-7
Our file Notre référence
ISBN: 978-0-494-22330-7

ABSTRACT

Halogen ratios (Br/Cl) and $\delta^{37}Cl$ values have been determined for fluid inclusion leachates extracted from quartz veins from porphyry copper deposits in Butte, Montana, U.S.A, and Bingham Canyon, Utah, U.S.A. Analyzed samples were dominated by low-salinity parental magmatic fluid inclusions that were trapped as a single-phase aqueous fluid in the one-phase field of the $NaCl-H_2O$ system. Br/Cl from early pre-Main Stage and later Main Stage veins at Butte range from 0.60-1.88 x 10^{-3} M, and Br/Cl for quartz veins from the potassically altered host monzonite at Bingham range from 0.18-3.68 x 10^{-3}M. Butte $\delta^{37}Cl$ values range from –0.8 to -2.3 ‰, and $\delta^{37}Cl$ values for Bingham are lower ranging from –0.9 to –4.1 ‰. Resultant data indicate a juvenile source of salinity in parental hydrothermal fluids related to porphyry deposit formation, and suggest that a significant partitioning of ^{35}Cl and ^{37}Cl occurs between Cl-bearing silicates and NaCl-dominated aqueous brines.

ACKNOWLEDGEMENTS

The Natural Sciences and Engineering Research Council (NSERC) of Canada financially supported this thesis through Discovery operating grants to Sarah Gleeson (University of Alberta). Additional funding was provided by NSERC through a PGSM scholarship and extension, the University of Alberta through Walter H. Johns Memorial Scholarships, and the Department of Earth and Atmospheric Sciences through Graduate Teaching Assistantships, Intern Tuition Supplements, and the GL Cumming Memorial Scholarship.

I would like to thank Sarah Gleeson for taking a chance and considering me for this project from the beginning, as well as providing me with invaluable guidance, support, and knowledge necessary to complete this degree. I would also like to acknowledge Brian Rusk, Jeremy Richards, Tom Chacko, Larry Heaman, Karlis Muehlenbachs, Bob Luth, Len Waasenaar, Geoff Koehler, Thomas Stachel, Alex Wolfe, and Pat Cavell for providing extensive scientific guidance throughout this project. Geological samples for this study were provided in collaboration with Brian Rusk (Denver, USGS), Anthony Harris (University of Tasmania), and Kim Schroeder (Kennecott Utah Copper). Sarah Gleeson and Jeremy Richards generously provided access to their respective fluid inclusion laboratories at the University of Alberta for the collection of ion chromatographic and microthermometric data. In addition, continuous flow isotope ratio mass spectrometry was completed at the Stable Isotope Hydrology and Ecology Laboratory of Environment Canada in Saskatoon, Saskatchewan with the expertise of Len Wassenaar and Geoff Koehler.

A special thanks to Michael Schultz, Trevor MacHattie, Larry Amskold, Rajeev Sasidharan-Nair, James Scott, Paulina Gromek, and several others in the department who helped me realize there is more to being a graduate student then living in the lab. I would also like to thank Don Resultay and Mark Labbe for not only preparing my samples, but for also being there whenever I was in a bind. Most importantly, I would like to thank my family for their unconditional love, support, patience, and encouragement throughout my academic career.

TABLE OF CONTENTS

LIST OF TABLES

LIST OF FIGURES

CHAPTER 1
SCOPE AND INTENT OF STUDY

Chloride is the most abundant anion in hydrothermal systems, and is one of the dominant metal complexing-ligands in magmatic-hydrothermal ore deposits. The ultimate source of chloride in these systems is debatable; it may be derived from the mantle, from the crust, or from a mixture of the two sources. To advance our understanding of the formation of these deposits, we need to be able to distinguish between these end-members, and to understand the processes that form mineralizing brines. The only way to directly sample the chemistry of these paleofluids is to analyze fluid inclusions trapped in minerals formed within the hydrothermal system. The primary objective of this study was to develop a technique for the analysis of stable chlorine isotopes in fluid inclusion leachates, and to apply this method to quartz hosted fluid inclusions from porphyry copper deposits in order to constrain the source of chloride within these magmatic-hydrothermal systems.

In an effort to understand the processes that have formed mineralizing brines, a small number of studies have determined elemental halogen ratios (Cl, Br, and sometimes I) for hydrothermal minerals and fluid inclusions (Böhlke an Irwin, 1992; Banks et al., 2000a,b; Kendrick et al., 2001). More recent studies suggest that it may be possible to identify the source of chloride in the fluid inclusions by using stable chlorine isotopes (^{35}Cl and ^{37}Cl) as a tracer (Banks et al., 2000a,b). Previous work has shown that crustal chlorine (a reservoir dominated by the oceans and evaporite minerals) has a $\delta^{37}Cl$ value of 0‰ and the mantle has a value of +4.7 ‰ (Magenheim et al., 1995). Therefore, it may be possible to constrain the chloride source in the fluid, and to calculate the relative contributions from two end-members in a mixed system.

For this study, a bulk fluid inclusion geochemical study has been carried out on a suite of quartz veins from two separate porphyry copper deposits: Butte, Montana, U.S.A, and Bingham Canyon, Utah, U.S.A. The study focused on pristine magmatic fluids; therefore, by targeting drill core specimens from deep within the potassic zones of alteration, it has been possible to minimize the likelihood of supergene overprinting and to limit the analyses of multiple fluid inclusion generations. The resultant halogen and Cl-isotope data have yielded insight into both chloride source and process (e.g., crystallization of Cl-bearing phases) within these magmatic systems. Ultimately, this study shows the potential of Cl-isotopes to deduce the source of chloride and fluid history in these systems, as well as providing insight into the global geochemical cycle of chlorine.

CHAPTER 2
BACKGROUND AND LITERATURE REVIEW

2.1 Fluid Inclusion Theory

Fluid inclusions are a unique and invaluable geochemical tool, especially when trying to decipher the physical and chemical environments of ore deposition. Analyses of fluid inclusions are the only way to directly sample ancient mineralizing fluids, and associated ore elements, volatile constituents, and soluble salts (Roedder, 1984). Fluid inclusion microthermometry can also provide information regarding temperature, pressure, fluid density and composition. In particular, porphyry systems often have complex fluid histories, with multiple and overprinting mineralization events and alteration types. On a microscopic level, these distinct events can be represented by multiple generations of fluid inclusions in a single host crystal. In order to generate a viable interpretation of bulk geochemical data, it is essential to characterize the relative contributions of different fluid inclusion populations found within the sample material. In this case, the application of fluid inclusions requires careful petrographic and microthermometric studies to characterize a sample and to ascertain if the sample is appropriate for inclusion analyses (Bodnar, 1994). Thus, initial petrographic and microthermometric studies allow a specific paleofluid to be targeted with better certainty. The following sections briefly describe trapping mechanisms, characterization, and applications of fluid inclusions.

2.1.1 Fluid Inclusion Trapping

During the precipitation or recrystallization of a mineral from a fluid phase, small portions of the parental hydrothermal fluid can be trapped within surface irregularities of the host crystal. As the crystal continues to grow (or with renewed growth), these imperfections can be sealed forming fluid inclusions (e.g., Roedder, 1984). As described below (see section *2.1.2*), inclusions can be classified as primary, pseudosecondary, or secondary based on when the fluid was trapped relative to the growth of the host crystal. The fluid that is trapped may be liquid, vapor, or a supercritical fluid depending on the pressure-temperature (P-T) conditions and fluid systematics of the hydrothermal system (see section *2.2.1*). The composition of a trapped fluid can range widely in terms of chemical and volatile constituents, degree of salinity, or the presence of melt material (Bodnar, 1994). Fluid inclusions can also contain solid daughter phases that have precipitated from the trapped fluid during cooling (e.g. halite). Although most hydrothermal minerals contain fluid inclusions, the minerals typically studied include quartz, fluorite, phosphates, carbonates, and sulfides.

2.1.2 Fluid Inclusion Characterization

Primary inclusions are defined as those formed during the initial growth of a crystal, and can be captured in a variety of ways. Most commonly primary inclusions are located within a crystal

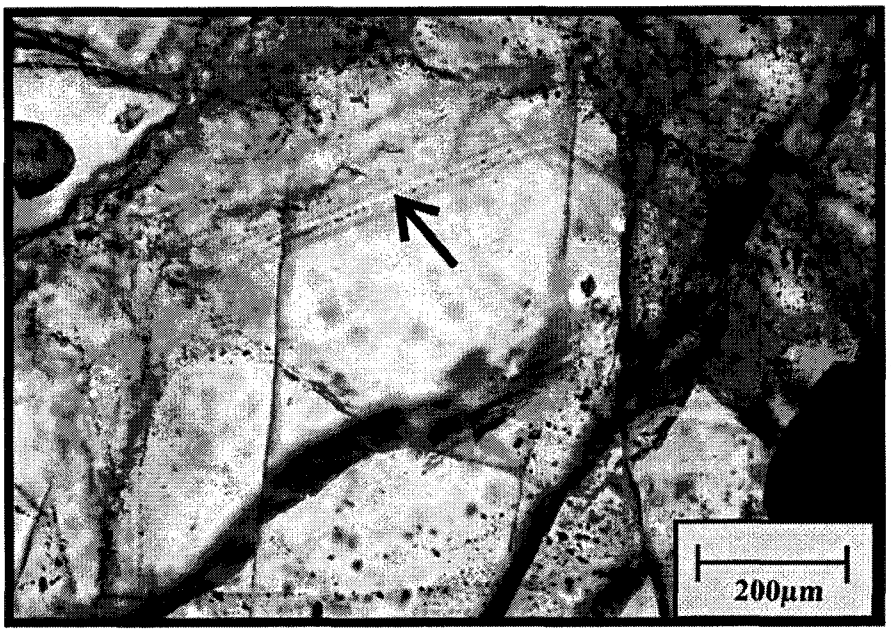

Figure 2-1: Primary fluid inclusions located along the growth planes of a quartz crystal at 100X magnification.

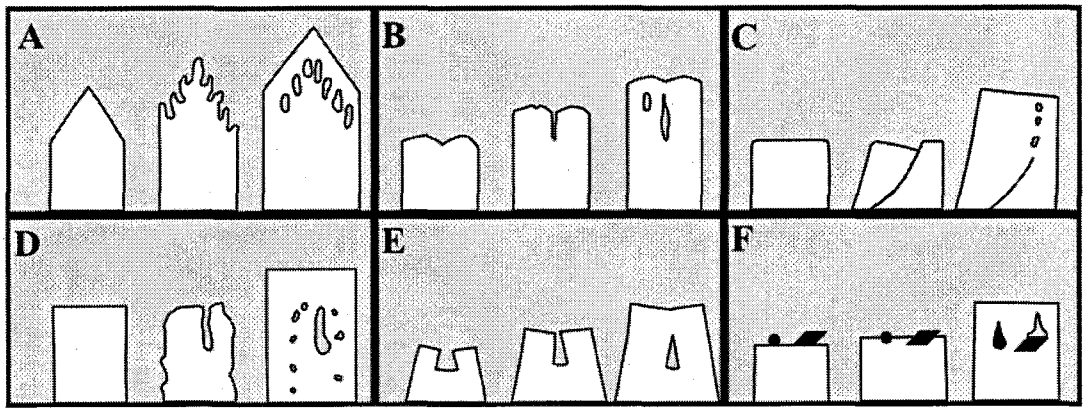

Figure 2-2: Various mechanisms for trapping primary fluid inclusions in crystals (modified after Roedder, 1984). (A) Dendritic growth is covered by solid growth. (B) Fluids are trapped as inclusions in between or at the centers of growth spirals. (C) A fracture that formed during crystal growth yields surface imperfection and trapping of inclusions. (D) Partial solution of a crystal yields a re-entrant and a curved crystal surface along which fluid inclusions are trapped when growth renews. (E) Sub-parallel growth of crystal blocks traps inclusions. (F) Any foreign particle on the surface of a growing crystal can be trapped as a solid inclusion, and fluid can be captured at the same time.

(intracrystalline) along growth zones or crystals voids (**Figure 2-1**). The imperfections that yield primary inclusions can result from rapid dendritic growth, spiraled or blocky growth patterns, or pits formed during the partial solution of a crystal (**Figure 2-2**; Roedder, 1984). Often, primary inclusions will display a negative crystal shape, but this is not always definitive of a primary origin (**Figure 2-3**). Pseudosecondary inclusions form when fractures develop and heal during the growth of a crystal; these trails of inclusions can be differentiated between secondary inclusions because they terminate at growth planes. In contrast, secondary inclusions represent the healing of fractures or any other process after the original growth of the crystal. Secondary inclusions are often distributed in planar arrays that cut across grain boundaries (**Figure 2-4**).

Using these petrographic guidelines, it is possible to classify a fluid inclusion assemblage. A fluid inclusion assemblage represents a group of inclusions that formed at approximately the same time during a specific trapping event (Goldstein and Reynolds, 1994). In other words, these inclusions contain a chemically similar fluid captured at roughly the same pressure and temperature. Examples of possible fluid inclusion assemblages include tight clusters of spatially related inclusions with a similar appearance (e.g., negative crystal shape, similar daughter minerals), inclusions trapped along growth planes, or trails of inclusions following annealed fractures (Goldstein and Reynolds, 1994). To further constrain the types of fluid inclusions contained with in a sample and whether or not a fluid inclusion assemblage is representative of a specific fluid event, microthermometric studies are required.

2.1.3 Fluid Inclusion Applications

Microthermometric studies are a fundamental non-destructive analytical technique applied to fluid inclusions (Roedder, 1984; Shepherd et al., 1985; Belkin, 1994). These studies involve controlled heating and cooling of fluid inclusions to constrain homogenization temperatures and fluid salinity, and rely on the assumption that fluid inclusions are closed systems. During cooling, differential shrinkage between a trapped single-phase fluid and the host crystal results in the formation of a contraction bubble (represented by a 2-phase inclusion at surface conditions). By heating the fluid inclusion until the bubble re-equilibrates back to a single phase, one can determine the minimum temperature of fluid trapping. This is defined as the homogenization temperature (Th) of the fluid inclusion. By combining the Th of a fluid inclusion and/or knowledge of fluid density with an estimated fluid pressure, the minimum trapping temperature is resolved using a phase diagram for the H_2O-NaCl system.

Fluid inclusion salinity is calculated by measuring melting temperatures (Tm) of ice, salt hydrates, or gas hydrates in the freezing cycle. For a pure H_2O-NaCl system, the temperature at which the last ice crystal melts is noted. This corresponds to a freezing point depression (Tm_{ice}), and salinities (up to 23.3 wt.% NaCl equivalent) can be calculated from experimental data (Bodnar and Vityk, 1994). In the case of CO_2-rich fluids (e.g., H_2O-CO_2-NaCl system), clathrate-melting temperatures (Tm_{clath}) must be measured (if clathrate is the last phase to melt) to derive salinity. In this

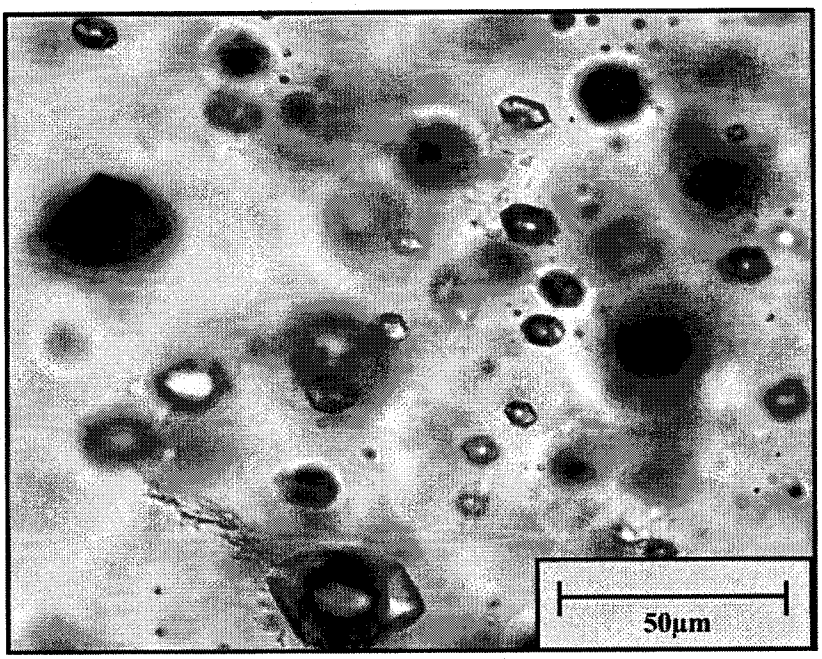

Figure 2-3: Primary intracrystalline intermediate density fluid inclusions from Bingham Canyon displaying negative euhedral crystal shape at 500X magnification.

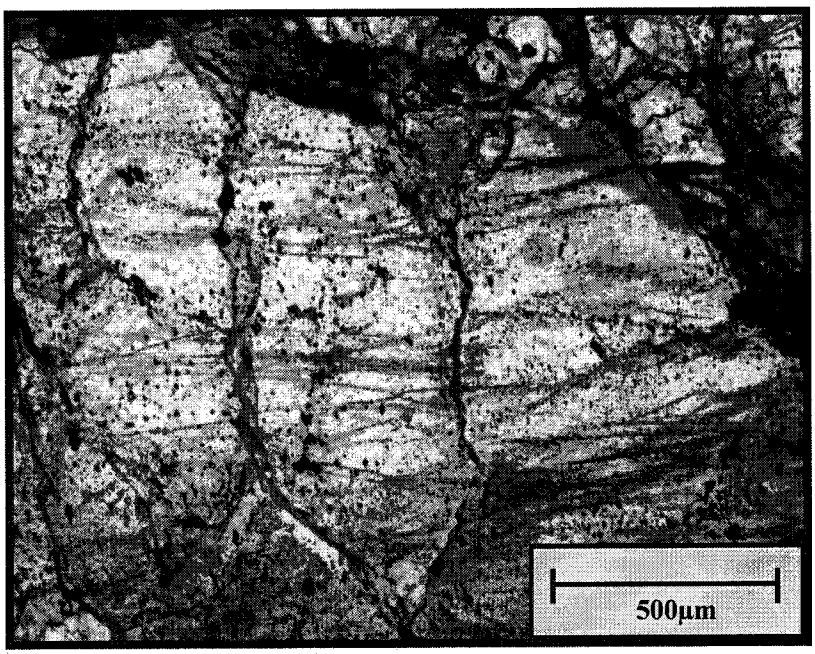

Figure 2-4: Secondary fluid inclusion trails that cut across grain boundaries in quartz from Bingham Canyon at 50X magnification.

case, computer-modeling programs can be used to calculate salinity (e.g., Bakker, 1997). Salinity for halite-bearing inclusions (>26.3 wt.% NaCl equivalent) can be determined by observing the melting temperature of halite daughters (Tm_{NaCl}) at high temperatures, and applying the appropriate solubility curve (Bodnar and Vityk, 1994). The results of the microthermometric studies carried out in this study are described in detail in **Chapter 4.**

2.2 Porphyry Copper Deposits

Porphyry copper deposits are a type of magmatic-hydrothermal deposit related to subduction-zone settings that typically host high tonnage, low-grade ore. These deposits are of great economic value, producing up to 50% of the world's copper, as well as notable amounts of gold, molybdenum, and silver (Hedenquist and Richards, 1998). Typically, these deposits are centered on porphyritic stocks rooted in deeper plutons of intermediate to felsic composition. Metals are transported by an exsolved magmatic fluid (see Section *2.2.1*), and metal solubility is a product of complexation with inorganic and organic ligands such as Cl^-, SO_4^{2-}, S^{2-}, NH_3^-, CO_3, acetate, and propionate (Wood and Samson, 1998). Although chloride is the dominant complexing-ligand in the aqueous phase, recent studies have suggested that a significant amount of metal transport is related to the contraction of a sulfide-rich vapor phase (Heinrich et al., 2004).

Lowell and Guilbert (1970) describe the idealized structure and associated hydrothermal alteration zones of porphyry deposits. The deep core is subject to early high temperature potassic alteration associated with biotite, K-feldspar, and magnetite mineral assemblages. Copper mineralization is largely associated with potassic alteration with Cu-Fe sulfide minerals concentrated in quartz stockwork veins and disseminations in the host rock. Progressing outwards from the core zones of sericitic alteration (quartz-sericite-pyrite), shallower argillic alteration (kaolinite-smectite-sericite-chlorite), and regionally extending propylitic alteration (epidote-chlorite-calcite) are commonly found (e.g. Lowell and Guilbert, 1970; Sillitoe, 1973; Gustafson and Hunt, 1975; Beane and Titley, 1981).

2.2.1 Exsolution and Phase Separation

During the evolution of a porphyry system, an initial homogeneous aqueous fluid of moderate salinity (2-10 wt% NaCl equivalent) is exsolved from the parental magma at pressures of 1 to 1.5 kbar, equivalent to 4-6 km depth at lithospheric pressure (Burnham, 1979; Cline and Bodnar, 1991; Hedenquist et al., 1998). This initial homogeneous fluid can be trapped in fluid inclusions near the base of the deposit (e.g., Bingham Canyon), although these types of inclusions are uncommon and usually restricted to deposits of unusual depth (e.g., Butte). As the magmatic fluid continues to ascend from the point of exsolution to the depth of porphyry stock emplacement and ore formation (2-3 km depth at a pressure of 0.5 kbar) it intersects its solvus forming immiscible liquid and vapor phases of

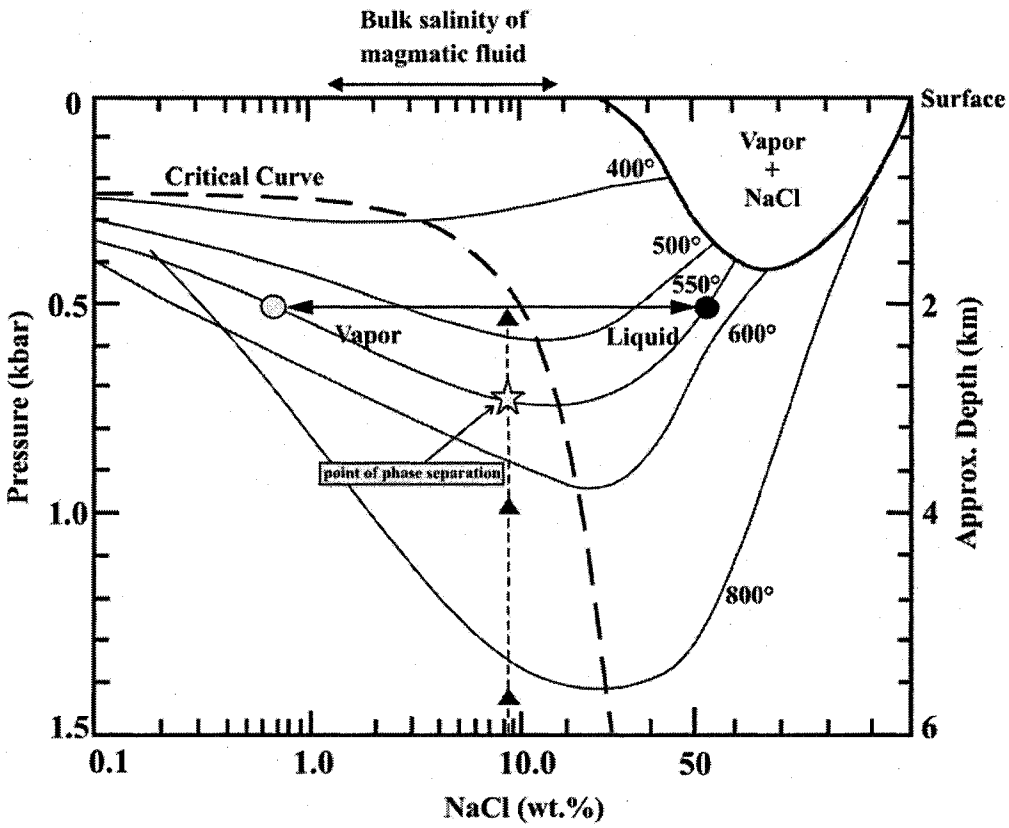

Figure 2-5: Phase diagram for the H_20-NaCl system (modified after Hedenquist and Richards, 1998 and references therein). A supercritical magmatic fluid with a bulk salinity of ~8.5 wt.% NaCl equivalent at 800°C will intersect its solvus (analogous to individual temperature isotherms) as it ascends to approximately 1.4 kbar. If this fluid cools to 550°C before ascending to this depth and pressure, it can rise to about 3 km depth (0.7 kbar) before separating into co-existing liquid and vapor phases. After further decompression to 0.5 kbar the compositions of the liquid and vapor phases evolve to salinities of ~55 wt.% NaCl equivalent and ~0.7 wt.% NaCl equivalent, respectively. Scale changes from logarithmic to linear at 10 wt.% NaCl.

contrasting density (**Figure 2-5;** Hedenquist and Richards, 1998). Thus, the co-existing hypersaline liquid-rich and low salinity vapor-rich fluid inclusions typically found within porphyry deposit minerals are representative of an un-mixed aqueous fluid involved with ore formation (**Figure 2-6**). For this study, quartz veins from porphyry deposits dominated by parental magmatic fluid inclusions, rather than the brine or vapor-rich end-members, have been chosen as the most suitable representatives for magmatic ore-forming brines.

In contrast, it may also be possible to exsolve a hydrosaline chloride liquid directly from the parent magma (Webster, 2004). This process is controlled by both the solubilities of chlorine and water in the silicate melt (less controlled by temperature and pressure), where the chlorine stability in a silicate melt depends on melt composition (e.g. the ratio of Cl/H_20 will determine the type of volatile phase that eventually exsolves; Webster, 2004). For subduction related calc-alkaline magmas, a hydrosaline chloride fluid should exsolve at a pressure of ~2 kbar (well below the usual depth of aqueous fluid exsolution). In addition, the exact timing of exsolution is controlled by SO_2 and CO_2 contents in the melt.

2.3 Previous Studies: Halogens and Chlorine Isotopes

A compilation of previous halogen and stable chlorine isotope data from fluid inclusions is provided in **Table 2-1**. Böhlke and Irwin (1992) measured halogen ratios using laser microprobe noble gas mass spectrometry in an attempt to determine characteristic signatures for magmatic, metamorphic, and geothermal aqueous systems. Results indicated that these systems had contrasting sources of fluid salinity, with the magmatic system (St. Austell) displaying intermediate Br/Cl ratios (0.85×10^{-3} M). The intermediate St. Austell value was suggested to be representative of magmatic volatiles. This idea was founded on a comparison between halogen ratios and published volcanic fumarole data. **Figure 2-7** depicts the comparison of Br/Cl for St. Austell and various volcanic fumarole condensates. Although there is significant scatter in the data, it was suggested that magmatic fluids may be characterized by Br/Cl less than that of seawater; specifically well defined between $0.5\text{-}1.0 \times 10^{-3}$ M. However, these data may not truly represent pristine magmatic-hydrothermal fluids. For example, fumarole data are not likely to be representative because of condensation and sublimation of various halide phases within fumarole conduits (Honda, 1970). Kendrick et al. (2001) reported a larger halogen data set for select porphyry deposits ranging between 0.87 to 1.87×10^{-3} M indicating that not all magmatic systems can be represented by the intermediate St. Austell value (**see Figure 2-7**).

There are two additional problems associated with using elemental halogen ratios to distinguish origins of salinity. The first issue is that unique halogen ratios do not necessarily exist since common processes in different settings can produce the same results. Secondly, the current database for halogen concentrations from fluid inclusions is lacking. Therefore, before making any further assumptions on magmatic signatures, we require more halogen data and additional geochemical constraints that avoid comparison with volcanic fumarole data.

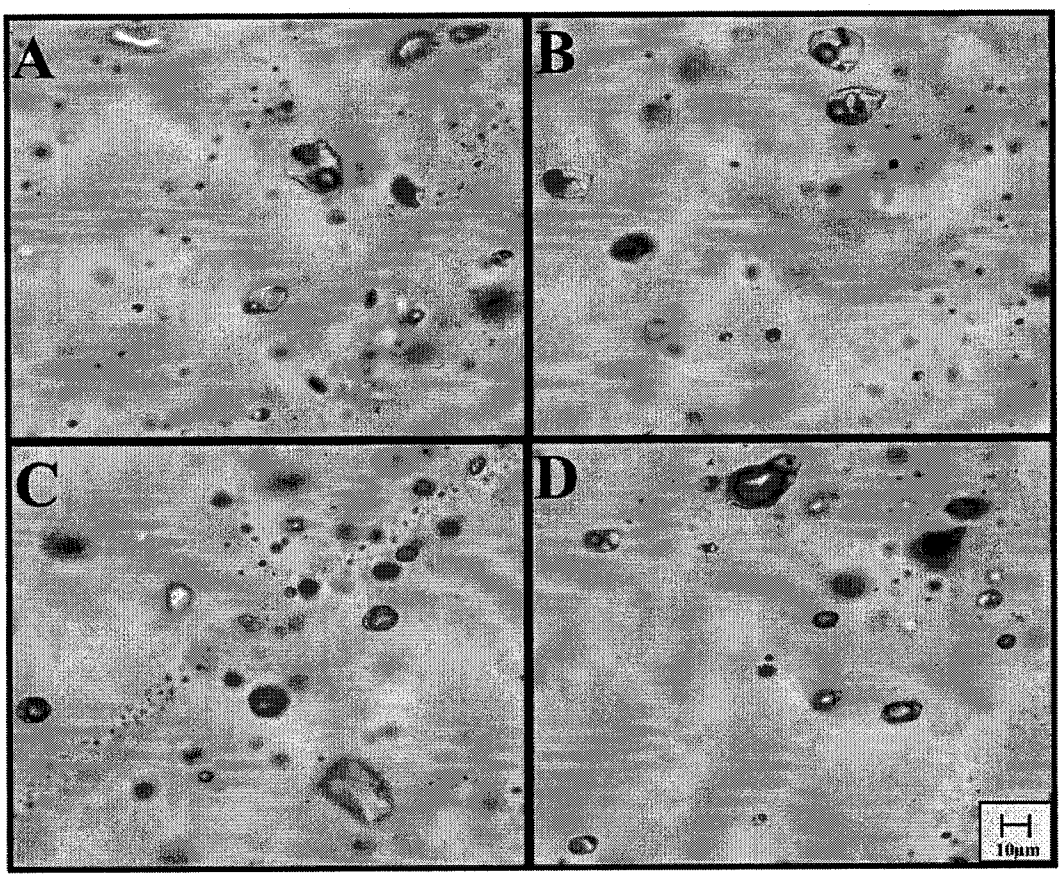

Figure 2-6: Polyphase brine (A, B) and vapor-rich fluid inclusions (C, D) from Bajo de la Alumbrera porphyry copper deposit. These phases formed when an exsolved homogeneous aqueous fluid ascended and intersected its solvus.

Table 2-1: Compilation of previous halogen and $\delta^{37}Cl$ fluid inclusion data for magmatic-hydrothermal systems.

Sample	Sample Description	Br/Cl ($x10^{-3}$ M)	$\delta^{37}Cl$ (‰)	References*
St.Austell (England)				
2320	quartz-tourmaline-topaz griesen	*0.85 ± 0.04*	-	[1]
St.Austell	quartz-tourmaline-topaz griesen	*0.68 ± 0.08*	-	[5]
Ascension Island (Atlantic Ocean)				
63-133-1	peralkaline granitic blocks (qtz, amph, kfd)	*1.65 ± 0.12*	-	[5]
63-133-4	peralkaline granitic blocks (qtz, amph, kfd)	*1.55 ± 0.22*	-	[5]
Capitan Pluton (New Mexico)				
W3-3	quartz vein in granite	0.22	-0.25 ± 0.09	[2]
MTE	quartz vein in granite	0.26	0.09 ± 0.09	[2]
CPU-2 (2)	quartz vein in granite	0.29	0.95 ± 0.09	[2]
BS (2)	quartz vein in granite	0.12	-0.33 ± 0.09	[2]
CM 242	quartz vein in granite	0.18	-0.24 ± 0.09	[2]
Cornubian Batholith (England)				
2320 (2)	quartz from quartz-tourmaline topaz rock	0.62	1.98 ± 0.09	[2]
H80-39 (2)	quartz from high temperature Sn-W vein	0.67	1.77 ± 0.09	[2]
SW84-20 (2)	quartz from high temperature Sn-W vein	0.49	1.69 ± 0.09	[2]
Butte (Montana)				
ER63-322	quartz vein + sulfide	*0.94 ± 0.21*	-	[5]
ER63-323	quartz vein + sulfide	*1.15 ± 0.23*	-	[5]
Bingham Canyon (Utah)				
BC5-A	quartz vein + molybdenite and chalcopyrite	*1.23 ± 0.02*	-	[3]
BC5-B	quartz vein + molybdenite and chalcopyrite	*1.33 ± 0.03*	-	[3]
BC5-C	quartz vein + molybdenite and chalcopyrite	*1.05 ± 0.01*	-	[3]
BC4	quartz vein in highly altered monzonite	*1.54 ± 0.01*	-	[3]
BC3	quartz veinlets+chalcopyrite and molybdenite	*1.87 ± 0.01*	-	[3]
BC2	quartz veinlet through equigranular monzonite	*1.17 ± 0.01*	-	[3]
B-1	quartz vein with chalcopyrite	-	0.3	[4]
B-2	quartz vein with chalcopyrite	-	0.8	[4]
ER63-207a	quartz + sulfide vein	*1.21 ± 0.14*		[5]
ER63-208	quartz + sulfide vein	*1.41 ± 0.24*		[5]
ER62-14	quartz + sulfide vein	*2.47 ± 0.50*		[5]
Ray (Arizona)				
R1	pyrite bearing quartz vein	*0.87 ± 0.01*	-	[3]
R3	pyrite bearing quartz vein	*0.91 ± 0.01*	-	[3]
Globe Miami (Arizona)				
GM3	chalcopyrite and pyrite bearing quartz vein	*1.01 ± 0.01*	-	[3]
GM4	pyrite bearing quartz vein	*1.00 ± 0.04*	-	[3]
Pinto Valley (Arizona)				
PV6	chalcopyrite bearing quartz vein	*1.06 ± 0.01*	-	[3]
PV1	pyrite bearing quartz vein	*1.37 ± 0.02*	-	[3]
Silverbell (Arizona)				
SB4	pyrite bearing quartz vein	*1.23 ± 0.01*	-	[3]
SB1(5)	pyrite and chalcocite bearing quartz vein	*1.24 ± 0.02*	-	[3]
SB8	quartz vein with pyrite	*1.45 ± 0.01*	-	[3]
SB6	quartz vein with pyrite	*0.94 ± 0.02*	-	[3]
SB P1	quartz vein with pyrite	-	0.1	[4]
SB K1	quartz vein with molybdenite	-	-0.7	[4]
Mission (Arizona)				
M3	skarn hosted chalcopyrite bearing quartz vein	*1.58± 0.01*	-	[3]
El Salvador (Chile)				
ES-86-1	quartz vein with pyrite	-	0.2	[4]
ES-86-3	quartz vein with chalcopyrite	-	-1	[4]
Panguna (Papua New Guinea)				
P-1	quartz vein with chalcopyrite	-	-0.5	[4]

*References: [1] Bohlke and Irwin (1992), [2] Banks et al. (2000b), [3] Kendrick et al. (2001), [4] Eastoe et al., (1989), [5] Irwin and Roedder (1995). *Italics* denote numbers reported originally as mean Br/Cl ($x10^{-3}$ M).

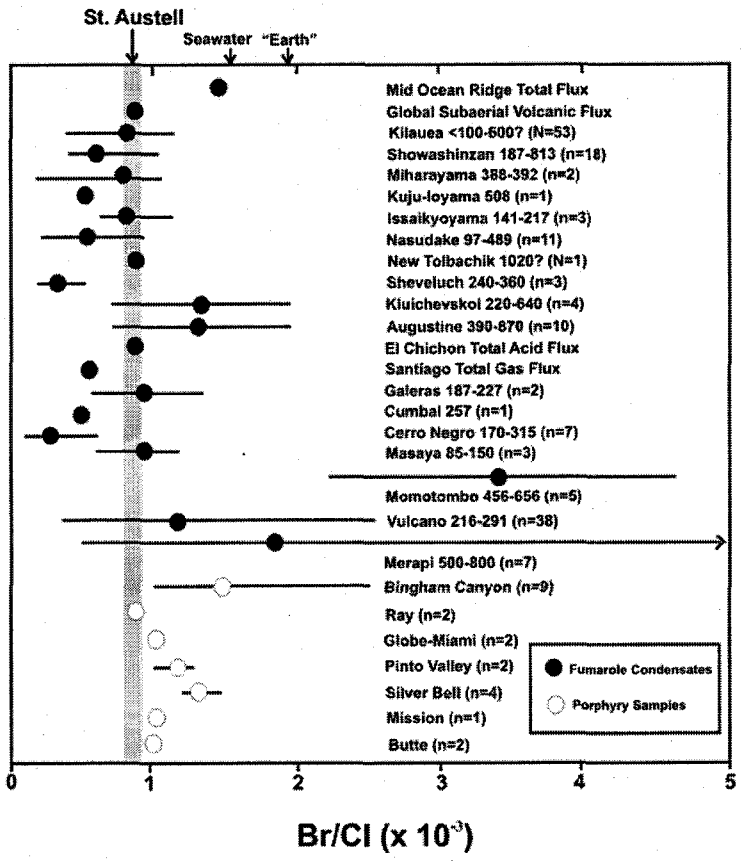

Figure 2-7: Br/Cl ratios in selected volcanic fumarole condensates in comparison to St.Austell data (grey shaded region) and various porphyry copper deposits (modified after Bohlke and Irwin, 1992). Bars indicate ranges of values reported; solid dots and open circles represent sample means; fumarole temperatures reported in (°C); number of samples (n) provided for each locality. Fumarole data is from Bohlke and Irwin (1992) and references therein. Porphyry data is from Irwin and Roedder (1995); Kendrick et al. (2001).

Eastoe et al. (1989) carried out the first stable chlorine isotope study on fluid inclusions from hydrothermal minerals, obtaining $\delta^{37}Cl$ values via gas source mass spectrometry (GSMS). The initial GSMS technique was problematic because it resulted in the analysis of multiple fluid inclusion populations as samples up to 500 g of quartz were crushed, and analytical precision was limited to ± 0.2‰. Nonetheless, the study reported a range in $\delta^{37}Cl$ values from –0.7 to 0.8 ‰ for 7 quartz vein samples from El Salvador, Silver Bell, Panguna, and Bingham Canyon porphyry deposits. Some variations in isotopic compositions within single deposits were attributed to different sources of chlorine for the early magmatic-hydrothermal and later meteoric-hydrothermal veins. The low $\delta^{37}Cl$ values of early fluids were hypothesized to represent a late stage partitioning of chloride between aqueous fluids where bonding was ionic and Cl-bearing silicates where bonding was covalent (Eastoe et al., 1989). The measurements from the Bingham Canyon deposit were distinct with $\delta^{37}Cl$ values of 0.3 and 0.8 ‰. The authors suggested that a component of local Cl-bearing formation waters in the system could be a source of high $\delta^{37}Cl$ brines. The conclusion of this study was that measurable fractionation of chlorine isotopes occurs in hydrothermal fluids, and that $\delta^{37}Cl$ data may eventually provide a strong constraint on the formation of porphyry copper deposits.

Eastoe and Guilbert (1992) acquired more data for the Bingham Canyon, Silver Bell, and Panguna deposits using a modified isotope ratio technique (GSMS) with improved precision. Similar to Eastoe et al. (1989), the results for the three deposits had $\delta^{37}Cl$ ranging from -0.1 to 0.4 ‰. Bingham Canyon had $\delta^{37}Cl$ ranging from 0.1 to 0.3 ‰ with the exception of one sample averaging -0.5 ‰. The new values were consistent with the previously reported 0.3 ‰ value, although the 0.8 ‰ value was not reproduced. It was suggested that negative values might represent the condensate of a $\delta^{37}Cl$ vapor enriched in the lighter isotope. For Panguna, three results were reported with consistent values of 0.2 ‰. Early and late veins from Silver Bell were again tested producing ranges of -0.1‰ to 0.4‰ and 0.2 to 0.3 ‰ respectively. Again, these values were similar to the results of Eastoe et al. (1989), although the lowest value of -0.7 ‰ for the early stage veins was not reproduced. Overall, it was concluded that the studied porphyry copper systems were characteristically slightly enriched in $\delta^{37}Cl$ relative to seawater. Ultimately, however, it is difficult to interpret the results of these studies as the large sample masses used (250-500 g) contained multiple generations of fluid inclusions.

In an attempt to further characterize a "magmatic" signature, recent studies have returned to analyzing stable chlorine isotopes by thermal ionization mass spectrometry (Banks et al., 2000a, b). The TIMS approach eliminated the sample size problem by requiring only 2 μg of Cl in the leachate, but the precision of the procedure was reduced to ± 0.2 ‰ (Xiao and Zhang, 1992; Magenheim et al., 1994; Xiao et al., 1995). Banks et al. (2000a,b) further improved the TIMS technique to increase the precision to ± 0.06 ‰ using 10 μg of Cl, and analyzed seven fluid inclusion leachates representing the magmatic-hydrothermal phase of mineralization from the Cornubian Batholith in Southwest England (Banks et al., 2000a,b). This study found the $\delta^{37}Cl$ value to be enriched by +1.9 ‰ suggesting a mixture of mantle and crustal chlorine within the ore deposit. **Figure 2-8** provides a summary of the

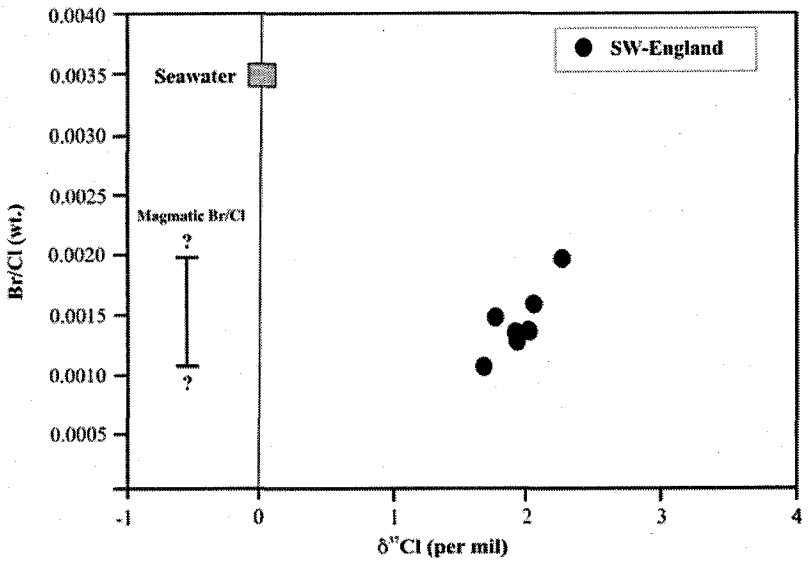

Figure 2-8: $\delta^{37}Cl$ vs. Br/Cl wt. for high temperature magmatic fluid inclusions from SW-England batholith (modified after Banks et al., 2000b). The range of magmatic Br/Cl ratios is for modern volcanic fumaroles.

Southwest England batholith data. The chlorine mixing assumptions are based on studies of unaltered MORB that produced an average value for mantle chlorine of 4.7 ‰ (Magenheim et al., 1995). Banks et al. (2000a,b) concluded that because the high temperature fluids from Southwest England have a magmatic signature in terms of $\delta^{18}O$, δD, and Br/Cl it was reasonable to suggest that $\delta^{37}Cl$ values around +2 ‰ are magmatic. Again, the problem with this study is that the Br/Cl fumarole data are assumed to represent a typical magmatic signature (refer to **Figure 2-8**). Thus, the results of this paper provide only preliminary constraints for determining a characteristic magmatic signature using halogen ratios and stable chlorine isotopes.

CHAPTER 3
SAMPLE MATERIAL AND ANALYTICAL METHODS

3.1 Chlorine Isotopes: Analytical History

Initially, stable chlorine isotopes (^{35}Cl and ^{37}Cl) have been determined using the isotope ratio technique (Kaufman et al., 1984; Long et al., 1993; Eggenkamp et al., 1995). This procedure involves precipitation of chloride as silver chloride salt (AgCl), reaction with iodomethane (CH_3I) to methyl chloride (CH_3Cl), and the measurement of CH_3Cl by gas source mass spectrometry (GSMS). The most recent modifications to the technique report a precision of ± 0.06 ‰ (Musashi et al., 1998). A minimum of 1 mg of Cl is required for analysis, and therefore is most effective in situations where large samples are available (e.g., $\delta^{37}Cl$ in natural waters).

In the case of fluid inclusions, paleofluids are released by crushing and leaching of the host mineral (Shepherd et al., 1985; Banks et al., 2000c; Gleeson, 2003), and the resultant leachate is then analyzed for isotopic compositions. The initial GSMS studies of stable chlorine isotopes in fluid inclusions were problematic because of the large amount of Cl required for $\delta^{37}Cl$ determinations (Eastoe et al., 1989; Eastoe and Guilbert, 1992). Significant amounts of host quartz (up to 500 g) had to be crushed to liberate enough fluid inclusion Cl; therefore, the obtained $\delta^{37}Cl$ for most samples was an average of multiple fluid inclusion populations in the sample. Thus, an alternative method was required in order to restrict analyses to a single fluid inclusion population.

The alternative method that was developed involved the measurement of the Cs_2Cl^+ ion by thermal ionization mass spectrometry (TIMS) (Xiao and Zhang, 1992; Magenheim et al., 1994; Xiao et al., 1995). The TIMS approach eliminated the sample size problem by requiring only 2 μg of Cl in the leachate, but the precision of the procedure was reduced to ± 0.2 ‰. Banks et al. (2000a,b) further improved the TIMS technique to increase the precision to ± 0.06 ‰ using 10 μg of Cl. A recent cross-calibration study of worldwide seawater samples compared the GSMS and TIMS techniques, and results indicate that the two techniques are in agreement for $\delta^{37}Cl$ values between – 4.4 ‰ to + 6.0 ‰ (Godon et al., 2004). In addition, Godon et al. (2004) also confirm the reproducibility of using Standard Mean Ocean Water (SMOC) as a universal reference standard for stable chlorine isotope analysis (e.g. Kaufman et al., 1984).

Recently, a new gas source technique has been developed using continuous flow isotope ratio mass spectrometry (CF-IRMS) (Wassenaar and Koehler, 2004). In comparison to original GSMS, the CF-IRMS approach now allows measurement of $\delta^{37}Cl$ in substantially smaller samples (<0.2 mg AgCl) with a precision of ± 0.06 ‰, and therefore provides an alternative to using TIMS for $\delta^{37}Cl$ determinations in fluid inclusions. For the current study, stable chlorine isotopes in fluid inclusions were analyzed using a modified CF-IRMS technique applicable to fluid inclusion leachates.

3.2 Sample Material

Quartz veins for fluid inclusion analysis were obtained from deep drill core sampling various alteration zones from Butte, Montana, and Bingham Canyon, Utah. These samples were provided in collaboration with Brian Rusk (USGS, Denver) and Kennecott Copper (Utah). A general summary of the sample localities is provided in **Table 3-1**, and more detailed geological descriptions are presented in **Chapter 5**. All of these deposits have been described by other workers and the samples come with good field and paragenetic frameworks (Meyer et al., 1968; Smedes, 1973; Moore and Nash, 1974; Brimhall, 1977; Lanier et al., 1978; Brimhall, 1980; Moore, 1978; Waarnars et al., 1978; Bowman et al., 1987; Irwin and Roedder, 1995; Kendrick et al., 2001; Rusk and Reed, 2002, Rusk et al., 2004). Microthermometric data and characterization of fluid inclusion populations for some of these samples have been previously reported (e.g. Rusk, 2003; Rusk et al., 2004), but for several samples these data were lacking and some microthermometry was carried out as part of this study (see **Chapter 4** and **Appendix D**).

3.2.1 Butte, Montana

Hand sample and drill core fragments from Butte included quartz veins from both the pre-Main Stage and Main Stage mineralization. Pre-Main Stage samples included quartz-molybdenite veins with potassic alteration selvages, and quartz-pyrite-sericite veins from the zone of pervasive sericitic alteration. Main Stage veins included central (quartz-enargite-covellite-pyrite) and peripheral (galena-sphalerite-rhodochrosite-quartz) samples. Nine samples in total were provided by Brian Rusk (USGS, Denver). These samples came with well-constrained petrographic descriptions and microthermometric data (Rusk, 2003; Rusk and Reed, 2002; Rusk et al., 2004). These data were further confirmed by additional petrographic and microthermometric studies in this project (see **Chapter 4** and **Appendix D**). A brief description of each sample is provided in **Table 3-2**, and more detailed descriptions are found in **Chapter 4** and **Appendix A**.

3.2.2 Bingham Canyon, Utah

Drill core slabs from Bingham Canyon were provided by Kennecott Copper (Utah), and included quartz - molybdenite and quartz - pyrite - sericite veins from the host monzonite and main-mineralizing quartz monzonite porphyry (QMP). Sixteen samples were obtained from deep in the pit ranging from 998 to 5079.5 feet in depth, and primarily sampled the potassic alteration zone. Only 12 samples yielded enough suitable quartz material for further analysis. One sample from the QMP was subject to intermediate argillic overprinting. These samples did not come with any direct previous petrographic or microthermometric constraints, and these had to be carried out as part of this study (see **Chapter 4** and **Appendix D**). A brief description of each sample is provided in **Table 3-2,** and more detailed descriptions are found in **Chapter 4** and **Appendix A**.

Table 3-1: Summary of sampled porphyry deposits.

Deposit	*Age*	*Location*	*Description*	*References**
Butte *(Montana)*	Tertiary *(~60 Ma)*	Porphyry Cu-Mo and base metal lode deposit hosted within the Butte quartz monzonite at the southern end of the Boulder Batholith.	Formed at unusually great depth relative to most porphyry deposits. Pre-Main Stage mineralization is typical porphyry copper mineralization with chalcopyrite and molybdenite in narrow quartz-dominated veins. Later Main Stage mineralization overlies and overprints the deeper porphyry mineralization, with meter-scale fissure veins bearing Cu, Pb, Zn, Mg, As, and Ag.	[1], [2]
Bingham Canyon *(Utah)*	Mid-Tertiary *(~39 Ma)*	Porphyry Cu-Mo deposit located in the central Oquirrh Mountains.	Typical porphyry mineralization and alteration associated with a hydrothermally altered igneous complex that intruded into late Paleozoic sedimentary rock. Eocene Bingham stock is the major host with quartz-veinlets bearing chalcopyrite and molybdenite. Mineralization also found in the Jordan and Commercial Limestone beds of the Bingham Mine formation.	[3], [4], [5], [6]

*References: [1] - Brimhall (1977), [2] - Rusk et al. (2004), [3] - Lanier et al. (1978), [4] - Moore (1978), [5] - Warnaars et al. (1978), [6] - Kendrick et al. (2001).

Table 3-2: Summary of quartz vein samples from Butte and Bingham Canyon.

Deposit	Sample	Host Rock	Alteration Zone	Vein Type
Butte (Montana)	*CZ1*	quartz monzonite	mainstage	quartz+pyrite+enargite+covellite
	AL2	quartz monzonite	mainstage	quartz+sphalerite+rhodochrosite+galena
	X3564	quartz monzonite	mainstage	quartz+sphalerite+rhodochrosite+galena
	11172-1871	quartz monzonite	potassic	quartz+molybdenite
	11172-3740	quartz monzonite	potassic	quartz+molybdenite
	11052-6215	quartz monzonite	sericitic	quartz+pyrite+sericite
	11052-7025	quartz monzonite	sericitic	quartz+pyrite+sericite
	11135-3740	quartz monzonite	potassic	quartz+minor sulfide
	Modoc-10649	quartz monzonite	-	quartz+sulfide+sericite+feldspar
Bingham Canyon (Utah)	*D415.2829.5*	monzonite	potassic	quartz+sulfide+ faint feldspar
	D415.2936	monzonite	potassic	quartz+sulfide+feldspar
	D415.2982.5	monzonite	potassic	quartz+sulfide
	D415.3025	monzonite	potassic	quartz+sulfide
	D415.3050	monzonite	potassic	quartz+sulfide
	D420.4710	monzonite	potassic	quartz+molybdenite
	D420.5079.5	monzonite	potassic	quartz+sulfide+zeolite
	D430.3639	monzonite	potassic	quartz+molybdenite+pyrite
	D430.3768	monzonite	potassic	quartz+molybdenite
	D162.2991	monzonite	potassic	quartz+molybdenite
	D162.3367	monzonite	potassic	quartz+molybdenite
	D152.2655	quartz monzonite porphyry	intermediate argillic	quartz only

3.3 Microthermometry

Initially, petrographic and microthermometric studies were carried out on double-polished fluid inclusion wafers for all sample veins and selected fluid inclusion assemblages as defined by Goldstein and Reynolds (1994). Microthermometric data were collected using a Linkam THMSG 600 heating and freezing stage, and thermocouples were calibrated at –56.6 °C, 0.0 °C, 374.1 °C, and 573.4 °C using synthetic fluid inclusion standards. Reported temperature measurements have an accuracy of ± 0.1 °C on cooling runs, and for heating runs within ± 1 °C. Microthermometric methods and results are described in more detail in **Chapter 4**, and raw data are presented in **Appendix D**.

3.4 Grain Preparation

Quartz veins were isolated from the host rock using a small rock saw, and subsequent sample material was crushed using an iron mortar and pestle. Crushing was carried out carefully in order to avoid loss of sample material either by grain jumping or powdering. Systematic steps of crushing and sieving allowed the reduction of grain size fraction to 1-2 mm, and pure quartz grains were picked under a binocular microscope to produce a clean mineral separate. Grains were placed in dilute nitric acid and heated on a hot plate just below boiling overnight to eliminate any surface contamination (Gleeson, 2003). Multiple cycles of rinsing and heating with de-ionized water removed trace nitric acid using pH as a proxy for neutral acidity. To remove residual moisture and ensure complete dryness, grains were dried overnight in an oven at 40-50 °C. Resultant grains were re-picked to remove any remnant contamination, weighed, and then stored in clean screw-top vials.

3.5 Crush-Leach

The crush-leach process liberates fluid inclusion contents (Shepherd et al., 1985; Banks and Yardley, 1992; Banks et al., 2000a; Gleeson, 2003), and yields the leachate necessary for halogen and Cl-isotope analysis. The concentration of a particular element in the leachate is the function of both the number of fluid inclusions in the sample, and the salinity of the fluid inclusions. The samples in this study often yielded low-salinity leachates because samples were dominated by abundant low-salinity parental magmatic fluids (see **Chapters 2** and **4**). Because this approach is a bulk technique, ideally it is better to analyze a small portion of a well-characterized sample. As discussed below, the amount of de-ionized water added during preparation was adjusted to produce a concentrated leachate rather than increasing sample size. For details regarding sample size and leach volume see **Appendix C**.

For each sample, 1-2 g of clean quartz grains were crushed to a powder of flour consistency using an agate mortar and pestle. To limit the loss of grains by jumping, a fabric or plexiglass guard was placed over the mortar. The powder was transferred to a 15 ml narrow mouth screw-top vial using a funnel, and 2-5 ml of de-ionized water was added. Fluid inclusion contents were re-dissolved by agitating the vial, and left overnight to allow residual silica to settle out. The leachate was further purified using a 3 ml syringe fitted with a 13 mm disposable syringe filter of 0.2 μm pore size to

remove any particulate matter. The filtered leachate was then transferred to a clean 15 ml screw-top vial and stored in a fridge to avoid any potential evaporation.

3.6 Ion Chromatography

Ion chromatography involves the separation of ions by ion-exchange resins in a chromatographic column, and is the only current technique for routinely analyzing anion species in fluid inclusion leachates. Leachate samples were analyzed for F^-, Cl^-, NO_2^-, Br^-, NO_3^-, PO_4^{-3}, and SO_4^{-2} at the University of Alberta using a Dionex DX600 ion chromatograph linked to PeakNet chromatography workstation software. The ion chromatograph was fitted with an AS-14 analytical column. In order to conserve sample leachate for $\delta^{37}Cl$ analysis, a micro-sampling tray and 1.5 ml chromatography vials were used to limit the amount of leachate required for anion analysis (~100 μL). Standards of various concentrations were prepared using a Dionex seven anion standard solution, and were used to quantify the areas under conductivity peaks (Gleeson, 2003). Replicate samples and check standards were run to determine analytical precision and accuracy (**Appendix C**). Detection limits for both Cl^- and Br^- are reported at 0.003 ppm (Gleeson, per. comm.).

Several crushes produced low salinity leachates, resulting in Br concentrations below detection limits (< 0.003 ppm) and Cl concentrations below suitable levels for silver chloride (AgCl) precipitation (< 2 ppm). More saline leachates (higher Br and Cl levels) were obtained by re-crushing sample material and adjusting de-ionized water contents from 2-5 ml to 1 ml. Based on the internal heterogeneity of the samples studied, it was not possible to reproduce identical fluid inclusion leachates for most samples (specifically for Br^- concentrations; see **Appendix C**). Because the crush-leach process is a bulk technique and sample size must be kept to a minimum, the poor external reproducibility most likely reflects a variance in the amount or distribution of fluid inclusions sampled during each separate crush. Thus, for samples with multiple crushes, Br/Cl ratios are reported as average values (see **Chapter 5**). This procedure is comparable to similar fluid inclusion studies carried out by Böhlke and Irwin (1992), Irwin and Roedder (1995), and Kendrick et al. (2001).

3.7 AgCl Preparation

The same leachate analyzed for halogens by ion chromatography was used for Cl-isotope analysis. Chloride in the fluid inclusion leachate was isolated for CH_3I reaction by precipitating out AgCl as described by Long et al. (1993) and Wassenaar and Koehler (2004). The leachate was transferred to a 50 ml volumetric flask, and volumetrically corrected to 50 ml by adding de-ionized water. The ionic strength of the solution was increased by adding 2 ml of 1M KNO_3, and then acidified by adding 1ml of 5 % (v/v) HNO_3. This solution was heated to 85 °C on a hot plate, and then 1 ml of 0.5 M $AgNO_3$ was added to precipitate AgCl. Samples were vacuum filtered through pre-weighed 0.7 μm glass fiber (GF) filters to isolate the AgCl precipitate. The sample beaker and filter were rinsed with a 0.2 vol. % HNO_3 solution. The AgCl filters were then placed on watch glasses, and

dried in an oven in the dark at 60 °C overnight to ensure complete dryness. Filters were weighed to determine quantitative AgCl yield (calculated gravimetric yields ranged between 90-99 %), and placed inside amber or foil wrapped 10 ml glass serum vials to prevent photo-dissociation (Long et al., 1993). The vials were sealed using butyl septum stoppers (ø = 20 mm) and aluminum open seal caps. Standards were prepared using the same methodology (200 µL of Ocean Scientific Internal Stock Atlantic Seawater and G-10953 east coast seawater).

3.8 CH_3I Reaction

CH_3I reaction and quantitative conversion of AgCl precipitate to CH_3Cl gas was carried out using the iodomethane reaction as described by Wassenaar and Koehler (2004), at the Stable Isotope and Ecology Laboratory of Environment Canada in Saskatoon, Saskatchewan. Stopper sealed amber or foil wrapped glass serum vials containing sample AgCl on GF filters were evacuated using a rotary vacuum pump to <0.001 atm through a 21 G needle coupled to a high vacuum manifold. 150 µL of liquid CH_3I was directly injected through the stopper into the evacuated vials using a 21G needle and syringe. The samples vials were then placed in a convective oven, and allowed to react for 48 hours at 85 °C to ensure complete reaction of AgCl to CH_3Cl. Previous blank runs with vials containing fresh filters or only CH_3I injection and no filters yielded no CH_3Cl (Wassenaar and Koehler, 2004).

3.9 CF-IRMS: CH_3Cl Analysis

CH_3Cl analysis via CF-IRMS was carried as described by Wassenaar and Koehler (2004). Between 150-700 µL of gas in the reaction vial containing both residual CH_3I and CH_3Cl was drawn into a 1000 µL gas-tight syringe and injected into a packed Porapak GC column through a sample injection port. The specific amount of gas drawn relied on the original yield of AgCl contained on the filter paper. The sample CH_3Cl peak was chromatographically separated from CH_3I and introduced via helium stream in the IRMS through an open split. The $\delta^{37}Cl$ values were obtained using a GV Instruments Isoprime IRMS. Data collection and normalization was carried out using Isoprime MassLynx instrument control software. The $\delta^{37}Cl$ value of sample Cl was calculated by measurement of CH_3Cl at m/z 52/50 compared to a reference injection of research grade MeCl (99.99 %). With routine IRMS source-tuning parameters, the target AgCl sample size for successful $\delta^{37}Cl$ determination was ~0.2 mg. Multiple injections of 100% CH_3Cl have yielded a repeatability (±SD) of ± 0.06 ‰ for $\delta^{37}Cl$ analyses (n =10)(Wassenaar and Koehler, 2004). To correct CH_3Cl $\delta^{37}Cl$ values relative to the SMOC reference, standards were prepared using 200 µL of Ocean Scientific Internal Stock Atlantic Seawater and G-10953 seawater (internal east coast seawater standard; see section **3.7**). There was no significant difference between the $\delta^{37}Cl$ values of both seawater samples. As described above (section **3.1**), this agrees with the use of global seawater as suitable reference material (e.g. Kaufman et al., 1989; Godon et al., 2004). The Atlantic seawater used for this study was assumed to have a $\delta^{37}Cl$ of 0 ‰ with respect to SMOC.

CHAPTER 4
FLUID INCLUSION PETROGRAPHY AND MICROTHERMOMETRY

4.1 Introduction

In order to generate a viable interpretation of bulk geochemical data, it is essential to characterize the spatial and temporal variability of different fluid inclusion populations found within the sample material. Porphyry Cu deposits often have complex fluid histories with multiple and overprinting mineralization events and alteration types; on a microscopic level these distinct events can be represented by multiple generations of fluid inclusions with in a single host crystal. Furthermore, recent cathodoluminescence studies reveal complex growth histories for quartz veins and associated fluid inclusions from Bajo de la Alumbrera, Butte, and Bingham Canyon (Rusk and Reed, 2002; Harris et al., 2004; Redmond et al., 2004; Landtwing et al., 2005). In this case, the application of fluid inclusions requires careful petrographic and microthermometric studies to ascertain if a sample is appropriate for bulk fluid analysis (e.g., Bodnar, 1994). Current microthermometric measurements and petrographic observations of fluid inclusion assemblages were used to identify the dominant fluid inclusion populations within each sample vein, and in turn to define the salinity budget in produced leachates. In total, twenty-one quartz vein samples from Butte and Bingham were selected for fluid inclusion petrography, and ~475 inclusions were analyzed microthermometrically.

4.2 Fluid Inclusion Petrography

Fluid inclusion petrography was carried out on doubly polished fluid inclusion wafers to characterize frequency of inclusions, size of inclusions, the spatial variability among inclusions, and inclusion type. Most samples contained hundreds to thousands of inclusions per cubic centimeter, ranging in size from <2 μm to 50 μm in diameter. Petrography focused on selected fluid inclusion assemblages (FIA) as defined by Goldstein and Reynolds (1994), and consisted of groups or clusters of intracrystalline inclusions displaying negative crystal shape with similar liquid to vapor ratios. In most samples, there is little direct evidence to confirm whether the inclusions are primary, pseudosecondary, or secondary. In general, inclusions located along euhedral growth zones are rarely observed, and secondary inclusion trails are present but are not the dominant inclusion type. Necking and leaking is suggested in many samples where clusters of irregularly shaped inclusions display variable liquid to vapor ratios. Thus, microthermometric data present the most reliable method to characterize the dominant fluid inclusion population within a sample vein, and to access whether FIA were trapped at the same time from the same fluid.

4.2.1 Butte Inclusions

Butte pre-Main Stage and Main Stage fluid inclusions types are categorized as B35, B60, B85, B15H, B20, and $B20_{(MS)}$ following the classification scheme of Rusk (2003). These inclusions

are distinguished based on the phases present at room temperature, where "B" refers to bubble and the associated number indicates the average volume percent bubble. The letter "H" refers to the presence of a halite daughter mineral. B20 inclusions are sub-divided between pre-Main Stage (B20) and Main Stage populations ($B20_{(MS)}$). Populations of B35, B60, and $B20_{(MS)}$ inclusion types dominate fluid inclusion leachates in this study, with rare amounts of B15H inclusions present in most samples (**Figure 4-1**). These inclusions are inferred to represent an aqueous, low-salinity, parental magmatic fluid that has not experienced fluid un-mixing.

B35 inclusions dominate the salinity budget (>90%) in two pre-Main Stage quartz-molybdenite veins (11172-1871 and 11172-3740) from the potassic zone of alteration. B35 inclusions are defined by 30-50 vol.% vapor bubble at room temperature, typically display negative euhedral to rounded subhedral crystal shape, and range in size from <2 μm to 20 μm in diameter. Some B35 inclusions contain an opaque daughter and/or a translucent daughter mineral that is not halite. Opaque inclusions are commonly triangular in shape, and are most likely chalcopyrite (Rusk, 2003). B35 assemblages are identified as clusters of intracrystalline inclusions within a single quartz grain or scattered across multiple quartz grains. B35 inclusions are rarely observed as secondary inclusion trails that cut across grain boundaries.

B60 inclusions are dominant (>90%) in two quartz veins from the zone of pervasive sericitic alteration (11052-6215 and 11052-7025), and one barren quartz vein with a potassic alteration envelope (11135-4967). B60 inclusions are defined by 50-70 vol.% bubble vapor at room temperature, are negative crystal to roughly equant (rounded rectangular) in shape, and can contain either opaque or translucent daughter minerals (not halite). Typically, B60 inclusions range in size from <2 μm to 30 μm in diameter. Similar to B35 inclusions, B60 assemblages are either clustered within single grains or scattered across multiple grains, and are rarely located along secondary inclusion trails.

$B20_{(MS)}$ inclusions were studied in quartz veins from the central and peripheral zones of Main Stage mineralization (CZ-1, AL2, and X3564). Sample CZ-1 is from the central zone, and is dominated by enargite, covellite, pyrite, and quartz. AL2 and X3564 are from the Main Stage periphery, and are dominated by galena, sphalerite, rhodochrosite, and quartz. $B20_{(MS)}$ inclusions contain 10-30 vol.% vapor bubble at room temperature, and are either rectangular, equant, or irregular in shape. No daughter minerals were observed in $B20_{(MS)}$ inclusions. Typically, $B20_{(MS)}$ inclusions range in size from <2 μm to 20 μm in diameter. $B20_{(MS)}$ assemblages are poorly defined as scattered inclusions across multiple grains, or located along linear secondary inclusion trails that cut across grain boundaries. Similar inclusions were observed in one quartz vein sample from the late Modoc intrusion and are further sub-divided as $B20_{(MOD)}$ inclusions.

4.2.2. Bingham Canyon Inclusions

Late quartz-molybdenite and quartz-pyrite-sericite veins from Bingham are dominated by intermediate density fluid inclusions (**Figure 4-2**; Redmond et al., 2004; Landtwing et al., 2005).

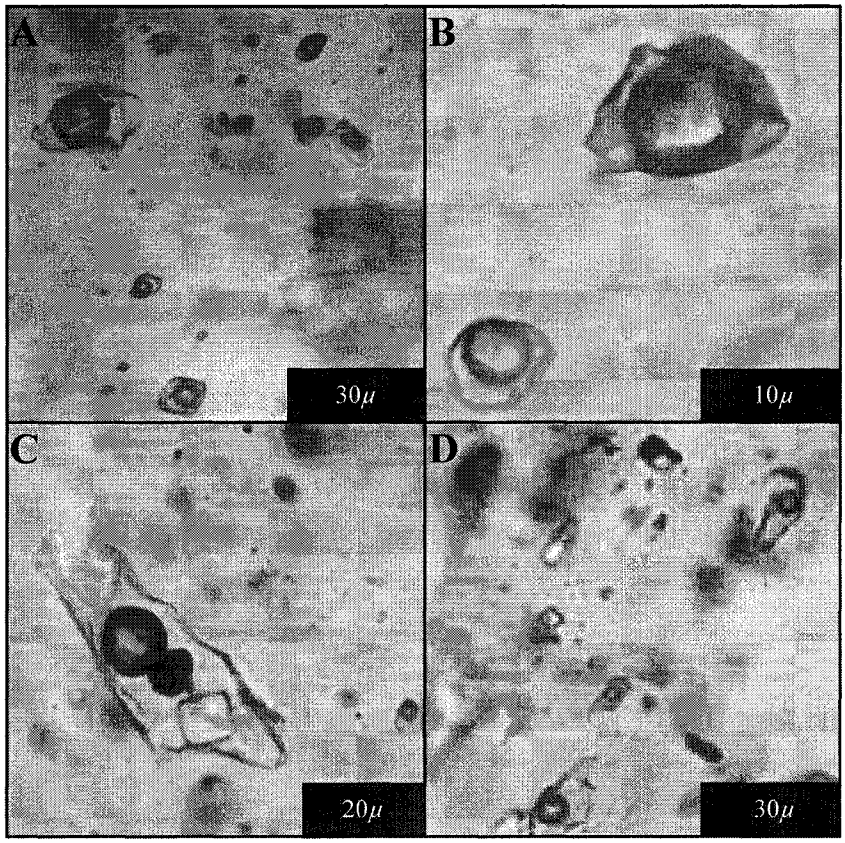

Figure 4-1: B35 (A), B60 (B), B15H (C), and $B20_{(MS)}$ fluid inclusion types at Butte.

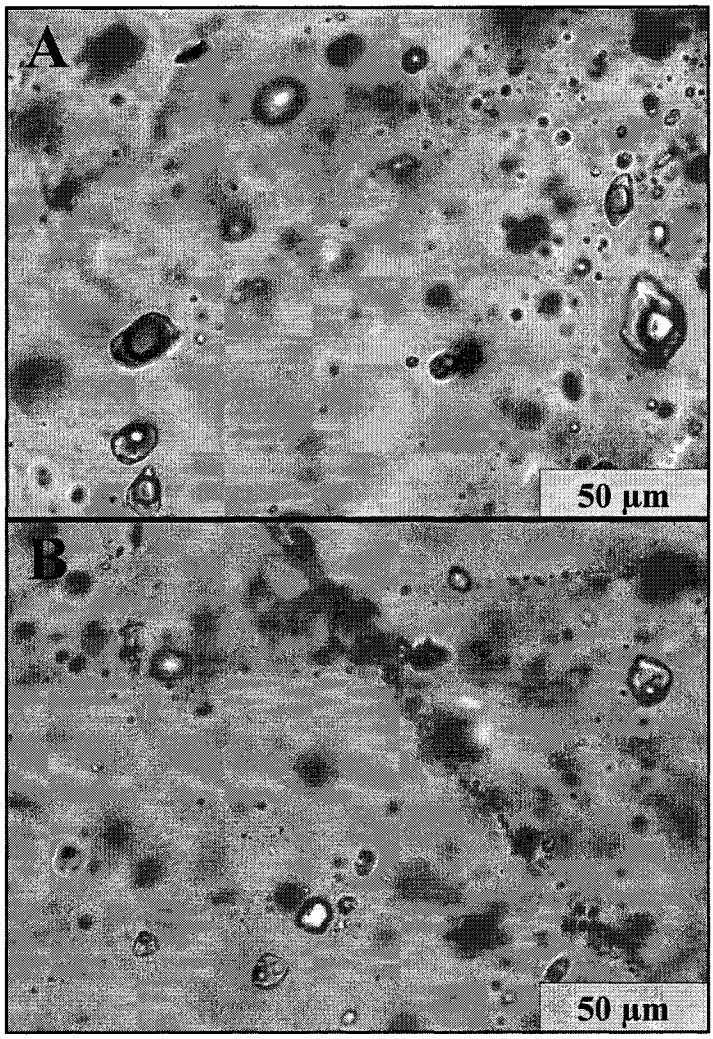

Figure 4-2: Intermediate density (A) and brine (B) fluid inclusion types at Bingham Canyon.

Previous studies of intermediate density inclusions are limited (Redmond et al., 2004), and these inclusions appear to be restricted to the deep areas of the deposit. These inclusions are inferred to represent an aqueous, low-salinity, parental magmatic fluid that has not experienced fluid un-mixing. Redmond et al. (2004) suggest that there is a critical depth at 500m below the QMP ore body were intermediate density inclusions can be found, and that vapor-rich and brines inclusions are rare below this point. Samples in this study support these findings in that vapor-rich and brine inclusions (or boiling trails) are rare in sampled quartz veins from deep within the potassic zone of alteration.

Intermediate density inclusions are dominant (>95%) in late quartz-molybdenite and quartz-pyrite-sericite veins from the potassic zone of alteration, along with rare brine and vapor-inclusions. Intermediate density inclusions are defined by 30-50 vol.% bubble vapor at room temperature, display euhedral to rounded subhedral negative crystal shape, and can contain either a small triangular opaque (e.g. chalcopyrite) or a translucent daughter mineral that is not halite. Typically, intermediate density inclusions range in size from 2 μm to 50 μm in diameter. Intermediate density assemblages are identified as clusters of intracrystalline inclusions within a single quartz grain or scattered across multiple quartz grains, located along euhedral growth zones, or occasionally observed as either pseudosecondary inclusion trails that are confined within grain boundaries or secondary inclusion trails that cut across grain boundaries.

Brine inclusions were most abundant in one quartz vein from the QMP that was subject to intermediate argillic overprinting, and this vein displayed a heterogeneous distribution of roughly equal amounts of intermediate density and brine inclusions. In addition, two quartz-pyrite-sericite veins (D415.2936 and D415.2982.5) contained a high abundance of 2-phase (liquid + vapor) inclusions that were either variably scattered throughout the veins or located along secondary inclusion trails. Typically, these inclusions were <2 μm in diameter, and homogenized to liquid at temperatures below 180 °C.

4.3 Microthermometry

Microthermometric data was collected using a Linkam THMSG 600 heating and freezing stage, and thermocouples were calibrated at –56.6 °C, 0.0 °C, 374.1 °C, and 573.4 °C using synthetic fluid inclusion standards. Reported temperature measurements have an accuracy of ± 0.1 °C on cooling runs, and for heating runs within ± 1 °C. Ice and halite melting temperatures were observed at a rate of no more than 0.5 °C/minute, and homogenization temperatures were observed at a rate of 5 °C/minute. Heating cycles of 5°C were used to determine the melting temperature of clathrate in CO_2-bearing inclusions, narrowing the range of clathrate dissolution to within ± 0.5 °C. Current microthermometric studies were applied only to characterize the dominant fluid inclusion populations within each sample vein, and were not applied to determine pressure-temperature conditions of vein formation. Raw microthermometric data are provided in **Appendix D.**

4.3.1 Butte Microthermometry

Results of current microthermometric studies are similar to previous studies for Butte (Rusk, 2003; Rusk et al., 2004). Liquid CO_2 was not observed in any inclusion types, although cooling to –30 to –35 °C formed clathrate in some B60 inclusions. For these inclusions, salinity estimates were calculated using the equations presented by Diamond (1992). Histograms for ice and clathrate melting temperatures, homogenization temperatures, and salinity for B35, B60, and $B20_{(MS)}$ inclusions are presented in **Figures 4-3**, **4-4**, and **4-5** respectively. **Figure 4-6** depicts a comparison of salinity and homogenization temperature for all inclusion types.

Ice melting was observed in B35 inclusions between –2.1 to –4.1 °C, corresponding to salinities in the range of 4-7 wt.% NaCl equivalent. All B35 inclusions homogenize to liquid between 330-350 °C with an average of 345 ± 1 °C, and inclusions within individual assemblages typically homogenized within ± 10 °C of one another.

B60 inclusions typically formed clathrate upon cooling. Clathrate melting temperatures were observed between 5.8 to 7.8 °C, corresponding to a range in salinity of 4-8 wt.% NaCl equivalent. For inclusions that did not form clathrate upon cooling, ice melting temperatures were observed between –2.8 to –2.9 °C, corresponding to a range of salinity between 4-6 wt.% NaCl equivalent. In comparison to B35 inclusions, B60 inclusions homogenize to vapor or critically at slightly higher temperatures between 360 to 390 °C with an average of 373 ± 1 °C (**Figure 4-6**). For inclusions that homogenized by critical behavior, the vapor bubble was observed to remain at a constant size during heating until gradually fading away over a span of 5 °C.

Ice melting was observed in $B20_{(MS)}$ and $B20_{(MOC)}$ inclusions between –0.3 to –4.1 °C, corresponding to salinities in the range of 1-5 wt.% NaCl equivalent. All $B20_{(MS)}$ and $B20_{(MOC)}$ inclusions homogenize to liquid between 200-350 °C, with an average of 270 ± 1 °C. In general, $B20_{(MS)}$ inclusions from peripheral Main Stage quartz veins had lower homogenization temperatures (200-288 °C) than central Main Stage $B20_{(MS)}$ inclusions (267-346 °C; **Figure 4-6**). Homogenization temperatures for $B20_{(MOD)}$ inclusions were similar to central Main Stage $B20_{(MS)}$ inclusions ranging from 266 to 376 °C.

4.3.2 Bingham Microthermometry

Results of current microthermometric studies are similar to previous studies for Bingham (Redmond et al., 2004). Liquid CO_2 was not observed in any intermediate density inclusions, although cooling to –30 to –35 °C formed clathrate in almost all inclusions. For these inclusions, salinity estimates were calculated using the equations presented by Diamond (1992). Measured melting temperatures in six inclusions of –56.6 ± 0.1°C in which a solid phase formed upon cooling indicate CO_2 is the predominant gas. Microthermometric data are presented for both intermediate density and co-existing brine inclusions where applicable. Histograms for halite and clathrate melting temperatures, homogenization temperatures, and salinity for intermediate density and brine inclusions

are presented in **Figures 4-7** and **4-8** respectively. **Figure 4-9** depicts a comparison of salinity and homogenization temperature for all inclusion types.

Intermediate density inclusions typically formed clathrate upon cooling. Clathrate melting temperatures were observed between 2.4 to 9.4 °C, corresponding to a range in salinity of 1-13 wt.% NaCl equivalent. For inclusions that did not form clathrate upon cooling, ice melting temperatures were observed between –1.4 to –2.1 °C, corresponding to a range of salinity between 2-4 wt.% NaCl equivalent. Intermediate density inclusions homogenize to vapor or by a pseudocritical behavior (Bodnar, 1994) at temperatures between 350 to 470 °C with an average of 385 ± 1 °C.

Halite melting was observed in brine inclusions between 231-306 °C, corresponding to salinities in the range of 34-39 wt.% NaCl equivalent. Brine inclusions homogenize to liquid or by halite dissolution at temperatures between 220 to 370 °C, with an average of 312 ± 1 °C. For inclusions that homogenize by halite dissolution, reported salinities are underestimated by up to 3 wt.% NaCl equivalent (Bodnar and Vityk, 1994).

4.4 Summary

Current microthermometric measurements and petrographic observations of fluid inclusion assemblages were used to identify the dominant fluid inclusion populations within each sample vein, and in turn to define the salinity budget in produced leachates. **Table 4-1** summarizes the relative abundance of fluid inclusion types within sampled quartz veins based on petrographic observations, and the resultant halogen and chlorine isotope data for the associated fluid inclusion leachates (presented in **Chapter 5**).

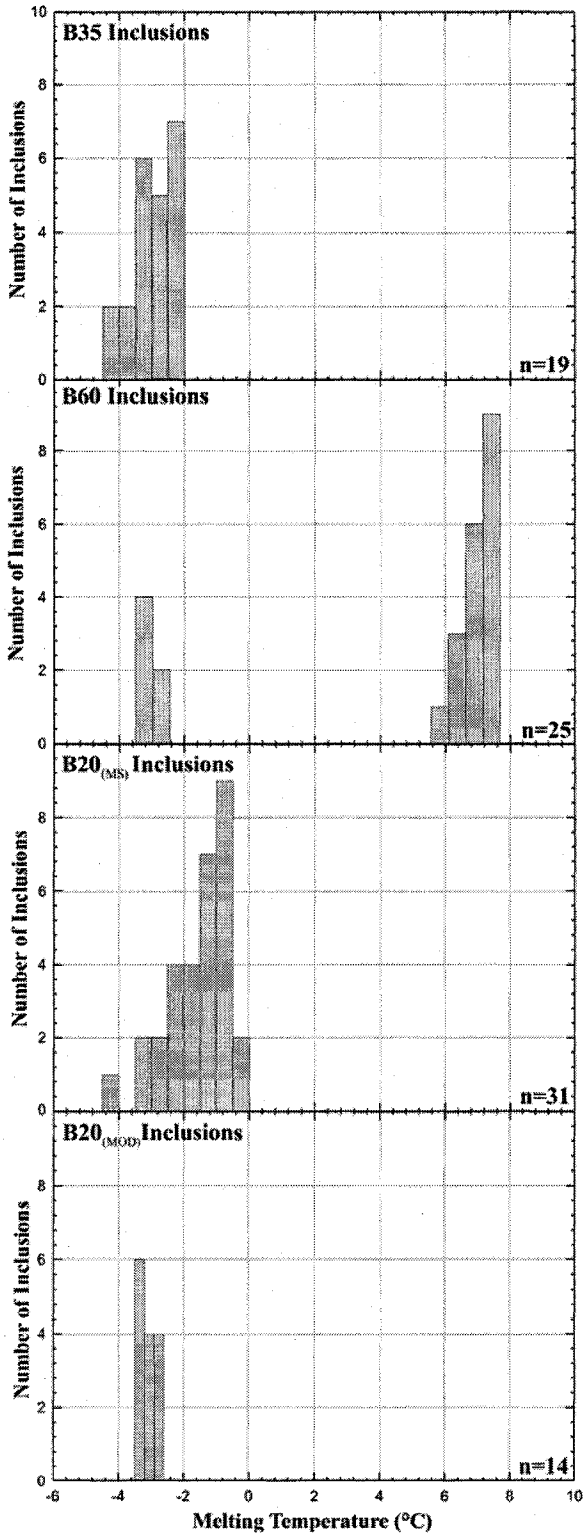

Figure 4-3: Melting Temperature of ice in B35, B60, $B20_{(MS)}$, and $B20_{(MOD)}$ inclusions from Butte. Clathrate melting temperatures are only reported for B60 inclusions, and occur above 0°C.

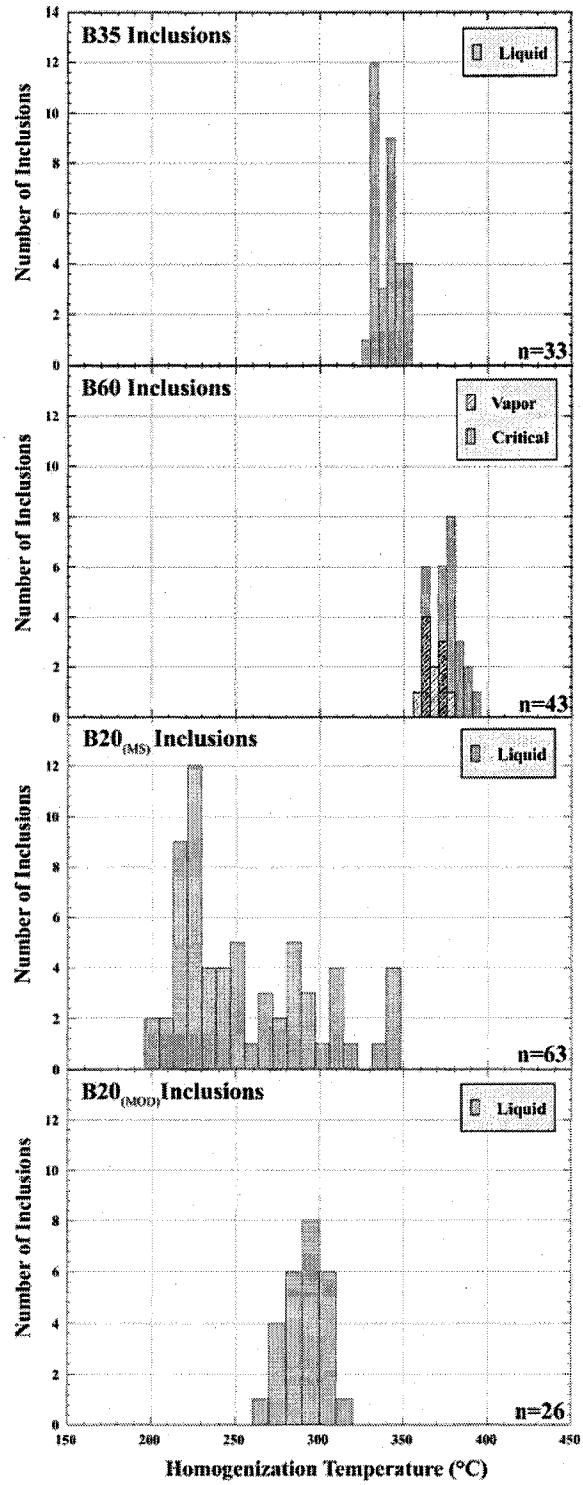

Figure 4-4: Homogenization temperatures for B35, B60, $B20_{(MS)}$, and $B20_{(MOD)}$ inclusions from Butte.

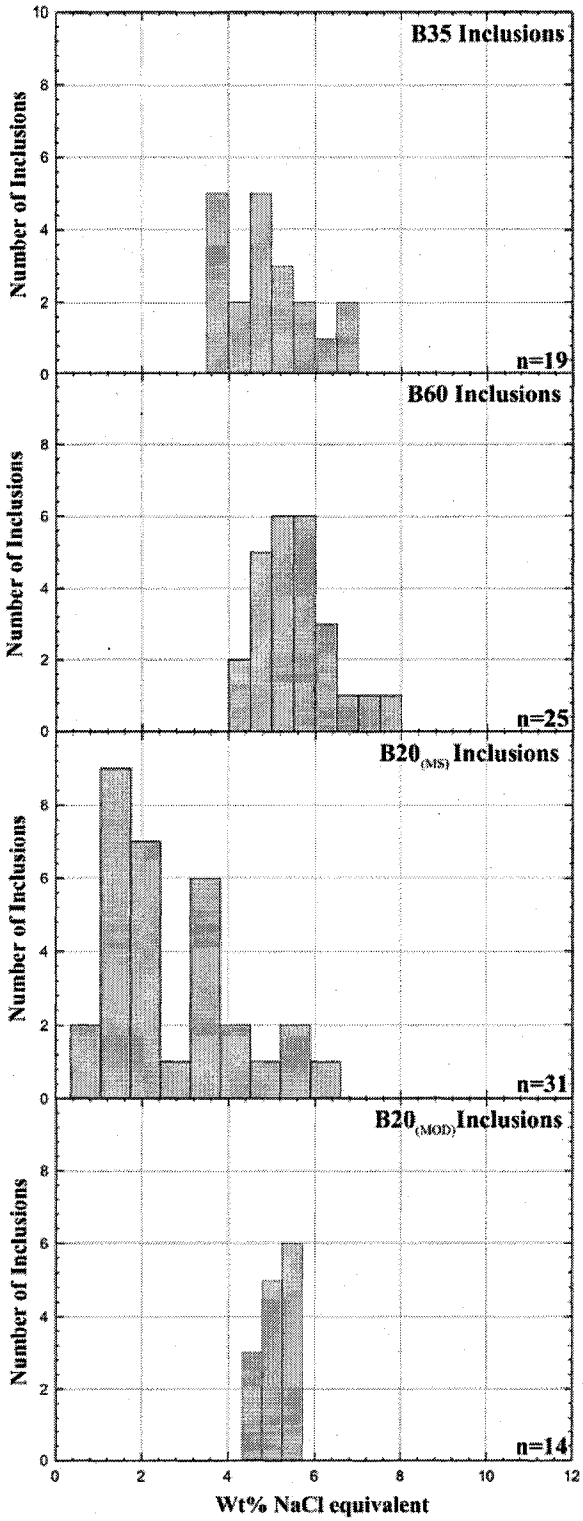

Figure 4-5: Salinities (wt.% NaCl equivalent) for B35, B60, $B20_{(MS)}$, and $B20_{(MOD)}$ inclusions from Butte.

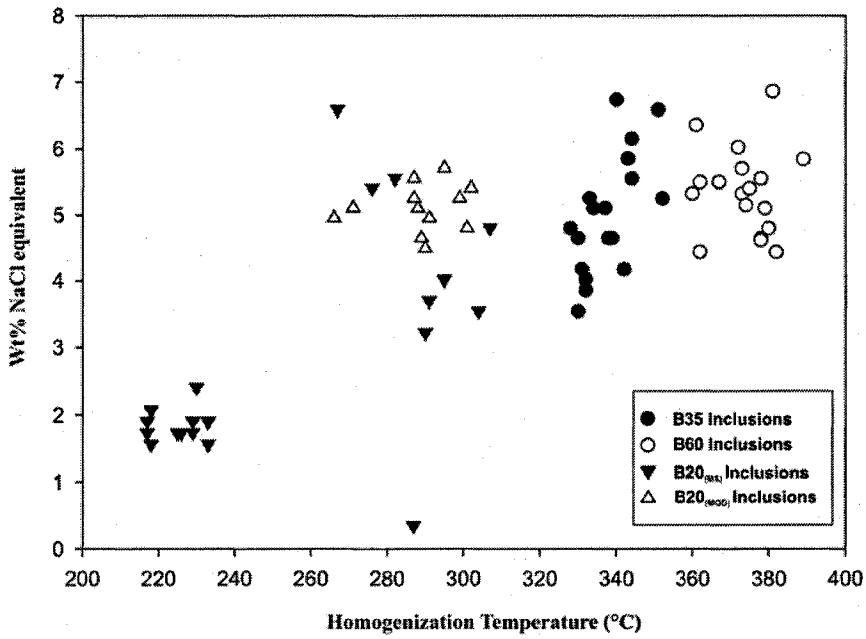

Figure 4-6: Homogenization temperatures vs. Wt.% NaCl equivalent for B35, B60, $B20_{(MS)}$, and $B20_{(MOD)}$ inclusions at Butte. In comparison to $B20_{(MS)}$ and $B20_{(MOD)}$ inclusions from the central region of Main Stage mineralization, $B20_{(MS)}$ inclusions from peripheral regions cluster towards lower salinities and homogenization temperatures and display a smaller range in values. B35 and B60 inclusions are quite similar, with B60 inclusions clustering at slightly higher homogenization temperatures.

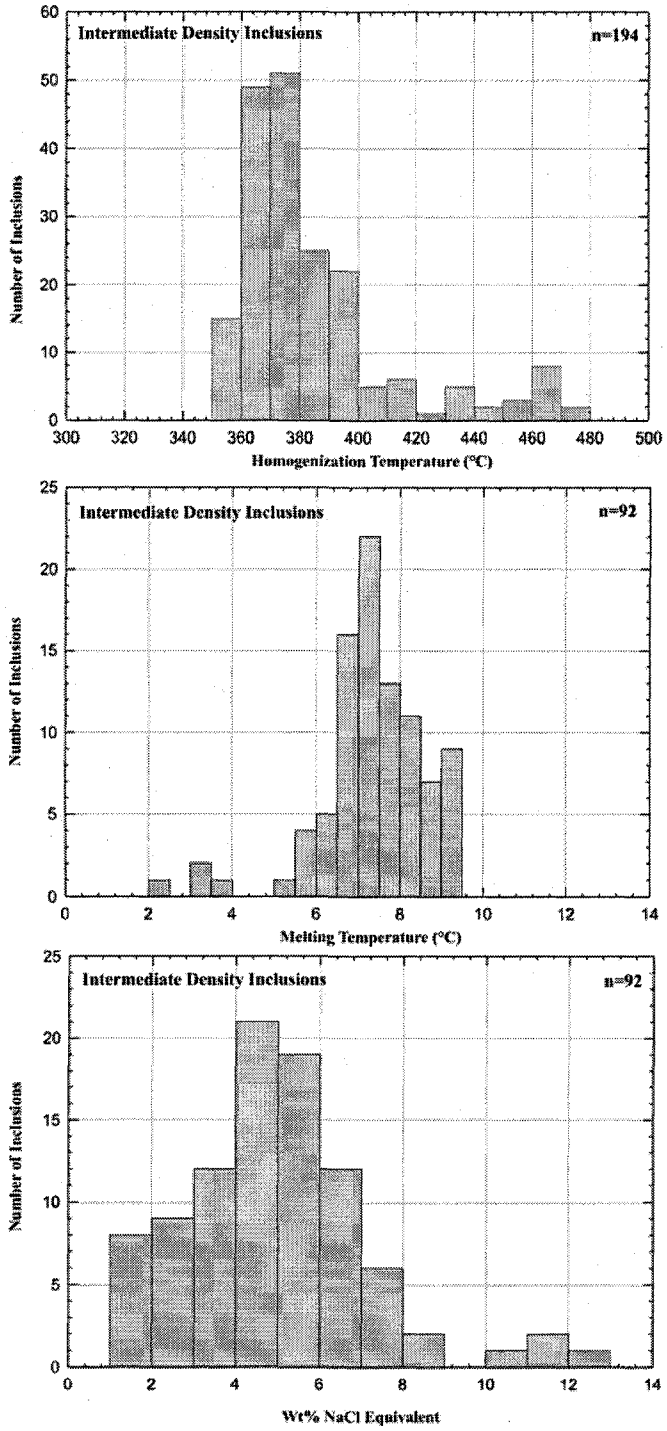

Figure 4-7: Homogenization temperatures, clathrate melting temperatures, and salinities (wt.% NaCl equivalent) for intermediate density inclusions at Bingham Canyon.

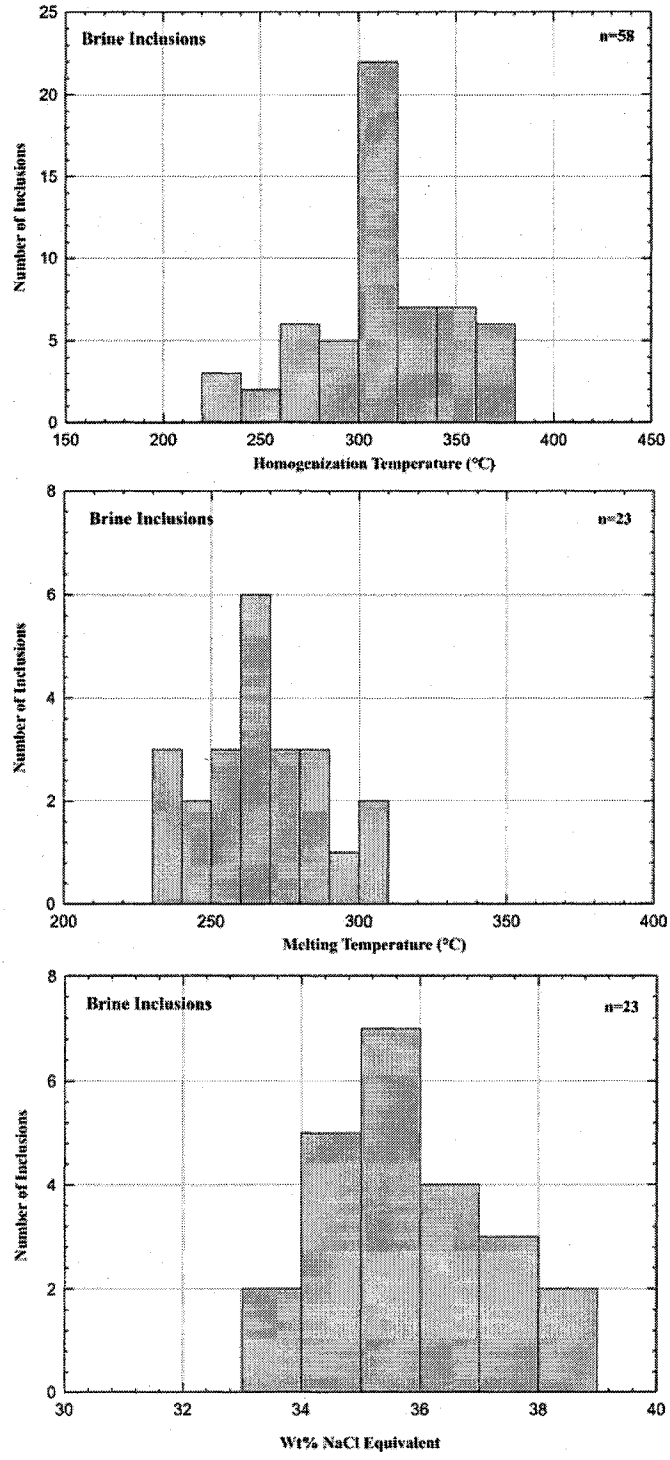

Figure 4-8: Homogenization temperatures, halite melting temperatures, and salinities (wt.% NaCl equivalent) for brine inclusions at Bingham Canyon.

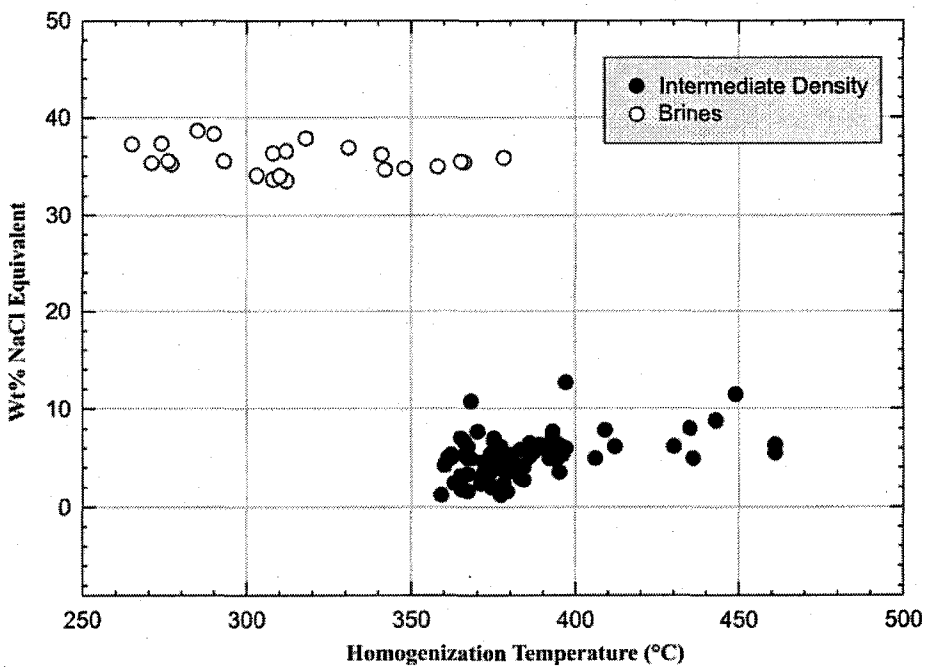

Figure 4-9: Homogenization temperatures vs. Wt.% NaCl equivalent for intermediate density and brine inclusions at Bingham Canyon. Salinities for brine inclusions are narrowly confined between 35 to 40 wt.% NaCl equivalent, with a range of homogenization temperatures between 260-375 °C. In contrast, intermediate density inclusions cluster at lower salinities between 1 to 8 wt.% NaCl equivalent, and homogenize at higher temperatures between 360-470 °C.

Table 4-1: Summary of quartz vein samples, fluid inclusion types, and geochemical data.

Deposit	Sample	Host Rock	Alteration Zone	Vein Type	Fluid Inclusion Frequency			Br/Cl (x 10^{-3} M)		Delta ^{37}Cl (‰)	
					LV	V	LVH	Range	Average	Range	Average
Butte **(Montana, USA)**	CZ1	BQM	mainstage	qtz+py+enr+cv	High	None	Rare	0.99-1.65	1.32	na	-1.3
	AL2	BQM	mainstage	qtz+sl+rdc+gn	High	None	Rare	na	1.88	na	-1.1
	X3564	BQM	mainstage	qtz+sl+rdc+gn	High	None	Rare	0.45-1.39	0.92	na	-2.0
	11172-1871	BQM	potassic	qtz+mo	High	Rare	Rare	-		na	-1.0
	11172-3740	BQM	potassic	qtz+mo	High	None	Rare	0.42-0.85	0.64	na	-1.3
	11052-6215	BQM	sericitic	qtz+py+ser	High	None	Rare	na	1.08	-1.0/ -1.6	-1.3
	11052-7025	BQM	sericitic	qtz+py+ser	High	None	Rare	na	0.81	na	-1.6
	11135-4967	BQM	potassic	qtz+minor sulfide	High	None	Rare	na	0.60	-0.6/ -1.0	-0.8
Bingham Canyon **(Utah, USA)**	D415.2936	EM	potassic	qtz+sulfide+kfs	Mod*	None	Rare	na	0.18	na	-0.9
	D415.2982.5	EM	potassic	qtz+sulfide	High*	Rare	Rare	na	0.22	-	
	D415.3025	EM	potassic	qtz+sulfide	High	Rare	Rare	na	0.88	na	-4.0
	D415.3050	EM	potassic	qtz+sulfide	High	Rare	Rare	0.32-0.58	0.45	-2.7/ -2.8	-2.8
	D420.4710	EM	potassic	qtz+mo	High	None	Rare	na	2.52	na	-3.1
	D420.5079.5	EM	potassic	qtz+sulfide+zeo	High	None	Rare	na	3.68	na	-2.6
	D430.3639	EM	potassic	qtz+mo+py	High	Rare	Rare	na	0.41	-	
	D430.3768	EM	potassic	qtz+mo	High	Rare	Rare	-		na	-3.4
	D162.2991	EM	potassic	qtz+mo	High	Rare	Rare	na	0.50	na	-3.2
	D162.3367	EM	potassic	qtz+mo	High	Rare	Rare	na	1.09	-	
	D152.2655	QMP	argillic	qtz	Mod	None	Mod	na	0.64	-2.6/ -5.5	-4.1

Abbreviations

BQM= Butte Quartz Monzonite; EM= Equigranular Monzonite; QMP= Quartz Monzonite Porphyry; Mod= Moderate

LV= liquid + vapor; V= vapor dominated; LVH; brine with halite daughter, (*)= secondary inclusions common

qtz= quartz, py = pyrite, cv= covellite, enr= enargite, mo= molybdenite; kfs= K-feldspar, ser= sericite, zeo= zeolite, sl=sphalerite, rdc= rhodochrosite, gn= galena

CHAPTER 5
HALOGEN AND STABLE CHLORINE ISOTOPE ANALYSIS OF QUARTZ - HOSTED FLUID INCLUSIONS FROM BUTTE AND BINGHAM CANYON

5.1 Abstract

A bulk geochemical study has been carried out on fluid inclusion leachates extracted from quartz veins from porphyry Cu deposits in Butte, Montana, U.S.A, and Bingham Canyon, Utah, U.S.A. Halogen ratios (Br/Cl) of fluid inclusion leachates were determined by ion chromatography, and $\delta^{37}Cl$ values of the leachates were measured by continuous-flow isotope-ratio mass spectrometry (CF-IRMS). Analyses were carried out on fluid inclusion leachates representing low-salinity parental magmatic fluid inclusions from Butte and Bingham that were trapped as single-phase aqueous fluids. Br/Cl ratios from early pre-Main Stage and later Main Stage veins at Butte range from 0.60-1.88 x 10^{-3} M. Ratios are similar between pre-Main Stage sericitically altered veins and Main Stage samples ranging from 0.81-1.08 x 10^{-3} M and 0.92-1.88 x 10^{-3} M respectively, clustering below seawater (1.54 x 10^{-3} M) and overlapping mantle values (~1-2 x 10^{-3} M). Two samples associated with early pre-Main Stage potassic alteration yield distinctly lower Br/Cl ratios of 0.60 and 0.64 x10^{-3} M. Butte $\delta^{37}Cl$ values range from –0.8 to -2.3 ‰ with no significant difference between pre-Main Stage and Main Stage samples. Br/Cl ratios for quartz veins from the potassically altered host monzonite at Bingham Canyon range from 0.18-3.68 x 10^{-3}M. A single quartz vein from the younger mineralizing quartz monzonite porphyry (QMP) returned a Br/Cl ratio of 0.64 x 10^{-3} M. Br/Cl ratios from Bingham are both higher and lower than previously reported for porphyry copper deposits. In contrast to Butte, $\delta^{37}Cl$ values for Bingham are lower, ranging from –0.9 to –4.1 ‰. Analyses of low-salinity inclusions trapped in the one-phase field, indicate a juvenile source of salinity in parental hydrothermal fluids related to porphyry deposit formation, and suggest that a significant partitioning of ^{35}Cl and ^{37}Cl occurs between Cl-bearing silicates and NaCl-dominated aqueous brines.

5.2 Introduction

The solubility and transport of metals in magmatic-hydrothermal systems is governed by complexation with inorganic and organic ligands such as Cl^-, SO_4^{2-}, S^{2-}, NH_3^-, CO_3, acetate, and propionate (Wood and Samson, 1998). Chloride, in particular, is an important anion to study because it is highly abundant, and is the dominant metal-complexing agent in many hydrothermal systems. The ultimate source of chloride in magmatic-hydrothermal systems is debatable, partially because processes such as phase separation, condensation, and/or mixing can mask the original magmatic signature of the fluids.

Halogen ratios (Br/Cl) have been used to differentiate between contrasting sources of salinity in fluid inclusions such as evaporated seawater, dissolution of halides, or magmatic fluids (e.g., Yardley et al., 2000; Yardley et al., 2003). The halogens are quite soluble in natural aqueous solutions,

and are considered to be geochemically conservative in many systems, as in the absence of halides, the halogens do not readily partition into mineral phases (e.g., Böhlke and Irwin, 1992). Thus, it has been suggested that halogen ratios can identify the origin of fluids from different reservoirs and help to determine fluid flow paths as a result (Böhlke and Irwin, 1992). The current database for elemental halogen ratios from hydrothermal minerals and fluid inclusions in magmatic hydrothermal systems is limited, although comparisons of global fumarole data with representative magmatic fluid inclusions from St. Austell granites have led previous authors to suggest that there is a range of Br/Cl ratios that correspond to juvenile magmatic fluids (Böhlke and Irwin, 1992; Banks et al., 2000a, b; Kendrick et al., 2001).

More recently, new techniques have been developed to measure stable chlorine isotopes in fluid inclusions (Eastoe, 1989; Eastoe and Guilbert, 1992; Banks et al., 2000a). It has previously been suggested that the chlorine in magmatic hydrothermal systems can be derived from the mantle, from the crust, or from a mixture of the two sources (e.g. Banks et al., 2000a). Chlorine, which is derived from a crustal reservoir (dominated by the oceans and evaporite minerals), has a $\delta^{37}Cl$ value of 0‰ and that derived from the mantle has a value of +4.7 ‰ (Magenheim et al., 1995). By using stable chlorine isotopes (^{35}Cl and ^{37}Cl) as a geochemical tracer, it may be possible to identify the source of chloride in the fluid inclusions and to calculate the relative contributions from two end-members in a mixed system. (Banks et al., 2000a, b). Fluid inclusion Cl-isotope studies from hydrothermal-magmatic systems are limited, especially for porphyry-Cu deposits (Eastoe et al., 1989 and Banks et al., 2000a, b), and no studies have addressed what the isotopic composition of a magmatic fluid may be.

In this study we analyzed the Br/Cl ratios and $\delta^{37}Cl$ compositions of fluid inclusion leachates from a series of microthermometrically well constrained vein quartz samples from the potassic and outer alteration zones of the deposits at Butte, Montana, U.S.A, and Bingham Canyon, Utah, U.S.A. The aim of the study was to characterize the halogen composition of the magmatic fluids in order to constrain (if possible) the origin of Cl in the system, and to identify any processes that may have resulted in the modification of the halogen signatures during the evolution of the mineralizing system.

5.3 Geological Setting

5.3.1 Butte, Montana

The Butte porphyry Cu-Mo deposit is hosted by the Butte quartz monzonite (BQM) at the southern end of the composite Boulder Batholith (Klepper, 1973; Miller, 1973; Smedes, 1973; Brimhall, 1977). The Butte porphyry is unusual because it formed at greater depths than most porphyry deposits, with depth estimates of original emplacement from 7 to 8 km based on hornblende barometry and fluid inclusion trapping pressures (Dilles et al., 1999; Rusk et al., 2004). There are two distinct ages of mineralization in the deposit termed pre-Main Stage and Main Stage (Meyer, 1965). Recent geochronological studies indicate emplacement of the BQM at approximately 75 Ma, pre-Main

Stage mineralization between 66 to 65 Ma, and Main Stage mineralization occurring between 65 and 62 Ma (Martin et al., 1999; Lund et al., 2002). Both pre-Main Stage and Main Stage veins were analyzed in this study (**Table 4-1**). Pre-Main Stage mineralization occurs in two concentrically zoned domal centers (Anaconda and Pittsmont Domes) with identical alteration types and vein-mineral assemblages (Rusk et al., 2004). Here, Cu-Mo mineralization is fracture controlled and is thought to have formed as exsolved magmatic aqueous fluids permeated through the BQM upon the emplacement of porphyry dikes. The interaction of these Cu-Mo bearing aqueous fluids with the BQM host generated stockwork veins and potassic wall rock alteration. Quartz-chalcopyrite-pyrite veins characterize early high temperature potassic alteration with biotite-K-feldspar-sericite alteration envelopes known as EDM (early dark micaceous) veins (Meyer, 1965; Brimhall, 1977). Potassic EDM alteration grades outward to a zone of pale green sericite (PGS) alteration with magnetite-pyrite-chalcopyrite-quartz veins displaying K-feldspar-chlorite-plagioclase-sericite alteration envelopes (Rusk, 2003). The mineralized Anaconda and Pittsmont domes are separated by a bulb-shaped monzonite rock body that is centered on a stockwork of pyrite-quartz veins with pervasive gray sericitic alteration that overprints pre-Main Stage mineralization west of the continental fault. Main Stage mineralization overlies and overprints the younger porphyry Cu-Mo pre-Main Stage mineralization with meter-scale fissure veins bearing high-grade Cu-Pb-Zn-Mn-As-Ag ores. These younger Main Stage veins are associated with an outward progression of sericitic and intermediate argillic alteration halos.

5.3.2 Bingham Canyon, Utah

The Bingham Canyon porphyry Cu-Au-Mo deposit is located in the central Oquirrh Mountains, 20 miles southwest of Salt Lake City, Utah (e.g., Lanier et al., 1978). The deposit is centered on a composite late Eocene (~38 Ma) porphyry stock that intruded into late Eocene equigranular monzonite and late Paleozoic sedimentary country rock (Lanier et al., 1978; Warnaars et al., 1978; Parry et al., 2001). Intrusion and mineralization at Bingham took place in a relatively short time span between 39.8 to 37.6 Ma (Warnaars et al., 1978; Keith et al., 1997), and from oldest to youngest the composite Bingham Intrusive Complex consists of: (1) equigranular monzonite, (2) quartz monzonite porphyry (QMP), (3) latite porphyry (4) mafic biotite porphyry, (5) quartz latite porphyry breccia and (6) quartz latite porphyry (Babcock et al., 1997; Deino and Keith, 1997; Landtwing et al., 2005). Quartz veins were studied from the equigranular monzonite and the QMP and only these two units will be discussed here. The pre-mineralization equigranular monzonite host is a fine-grained intrusive rock that was emplaced passively by stoping and assimilation (Lanier et al., 1978), with the highly altered Bingham Stock hosting a considerable portion of copper mineralization. The QMP is a thick dike-like body that intruded the Bingham Stock, and is associated with the highest ore grade, highest density of stockwork veining, and the most intense potassic alteration (Landtwing et al., 2005). Main-stage hydrothermal alteration is characterized by an inner zone of potassic alteration,

an outer propylitic zone flanked by unaltered rocks, and late argillic and sericitic zones that occur along the NW margins of the deposit that post-date potassic alteration (Babcock et al., 1997). Cu-Au mineralization coincides with potassic alteration, and is associated with multiple episodes of fracturing and mineral precipitation leading to the formation of stockwork quartz veins and sulfide disseminations. These stockwork veins contain chalcopyrite and bornite with hydrothermal K-spar and biotite found in the veins or as alteration selvages. Quartz-molybdenite veins formed at ~37 Ma (Chesley and Ruiz, 1997), and postdate both Cu-Fe-sulfide mineralization and the youngest intrusive magmatism. Based on crosscutting relationships, the latest veins are quartz-pyrite veins with overprinting sericite selvages. Samples in this study are from the potassically altered host monzonite and include late quartz-molybdenite and quartz-pyrite-sericite veins, with the exception of one vein from the QMP that was subject to pervasive argillic overprinting (**Table 4-1**).

5.4 Analytical Procedure

Initially, petrographic and microthermometric studies were carried out on double-polished fluid inclusion wafers for all sample veins and selected fluid inclusion assemblages as defined by Goldstein and Reynolds (1994). Microthermometric data were collected using a Linkam THMSG 600 heating and freezing stage, and thermocouples were calibrated at –56.6 °C, 0.0 °C, 374.1 °C, and 573.4 °C using synthetic fluid inclusion standards. Reported temperature measurements have an accuracy of ± 0.1 °C on cooling runs, and for heating runs within ± 1 °C.

Quartz veins were isolated from the host rock using a small rock saw, and were crushed and sieved to a grain size fraction of 1-2 mm. The samples were then picked under a binocular microscope to produce a clean mineral separate. Grains were placed in dilute nitric acid and heated on a hot plate just below boiling overnight to eliminate any surface contamination (e.g., Gleeson, 2003). 1-2 g of clean quartz was crushed to a powder of flour consistency using an agate mortar and pestle (Shepherd et al, 1985; Banks and Yardley, 1992; Gleeson, 2003). Fluid inclusion contents were re-dissolved by adding 2-5 ml de-ionized water and agitating the sample. Resultant leachates were purified using a 3 ml syringe fitted with a 13 mm disposable syringe filter of 0.2 μm pore size.

Leachate samples were analyzed for anions using a Dionex DX600 ion chromatograph fitted with an AS-14 analytical column. To conserve sample leachate for $\delta^{37}Cl$ analysis, a micro-sampling tray and 1.5 ml chromatography vials were used to limit the amount of leachate consumed during anion analysis. Several crushes produced low salinity leachates, resulting in Br concentrations below detection limits (< 0.003ppm and Cl concentrations below suitable levels for subsequent silver chloride precipitation. More saline leachates were obtained by re-crushing sample material and adjusting de-ionized water contents to 1 ml. Based on the complex nature and internal heterogeneity of some of the samples in this study, it was impossible to reproduce identical fluid inclusion leachates due to variations in the Br concentrations between crushes.. This is reflected by wide ranges in Br/Cl ratios produced during multiple crushes of discrete samples (e.g., Butte, Montana).

The same leachate analyzed for halogens by ion chromatography was used for Cl-isotope analysis. Chloride in the fluid inclusion leachate was isolated for CH_3I reaction by precipitating out silver chloride salt (AgCl) as described by Long et al., (1993) and Wassenaar and Koehler, (2004). The ionic strength of the solution was increased by adding 2ml of 1M KNO_3, and then acidified by adding 1ml of 5% (v/v) HNO_3. This solution was heated to 85°C on a hot plate, and then 1ml of 0.5M $AgNO_3$ was added to precipitate AgCl. Samples were vacuum filtered through pre-weighed 0.7μm glass fiber (GF) filters to isolate the AgCl precipitate. Filters were weighed to determine quantitative AgCl yield and placed inside amber or foil wrapped 10ml glass serum vials to prevent photo-dissociation (Long et al., 1993). The vials were sealed using butyl septum stoppers (ø = 20mm) and aluminum open seal caps.

Quantitative conversion of sample AgCl precipitate to CH_3Cl gas was carried out using the Iodomethane (CH_3I) reaction as described by Wassenaar and Koehler (2004), at the Stable Isotope Hydrology and Ecology Laboratory of Environment Canada in Saskatoon, Saskatchewan. Stopper sealed amber glass or foil wrapped serum vials containing sample AgCl on GF filters were evacuated using a rotary vacuum pump to <0.001 atm through a 21 G needle coupled to a high vacuum manifold. 150 μL of liquid CH_3I was directly injected through the stopper into the evacuated vials using a 21G needle and syringe. The sample vials were then placed in a convective oven to react for 48 hours at 85°C to ensure complete reaction of AgCl to CH_3Cl gas.

CH_3Cl analysis via CF-IRMS was carried out as described by Wassenaar and Koehler (2004). Between 150-700 μL of gas in the reaction vial containing both residual CH_3I and CH_3Cl was drawn into a 1000 μL gas-tight syringe and injected into a packed Porapak GC column through a sample injection port. The sample CH_3Cl peak was chromatographically separated from CH_3I and introduced via helium stream into the IRMS through an open split. The $\delta^{37}Cl$ values were obtained using a multicollector GV Instruments Isoprime™ IRMS. Data collection and normalization was carried out using Isoprime MassLynx instrument control software. The $\delta^{37}Cl$ value of sample Cl was calculated by measurement of CH_3Cl at m/z 52/50 compared to a reference injection of research grade CH_3Cl (99.99%). With routine IRMS source-tuning parameters, the target AgCl sample size for successful $\delta^{37}Cl$ determination was ~0.2mg. Multiple injections of 100% CH_3Cl yielded a repeatability (±SD) of ±0.06‰ for $\delta^{37}Cl$ analyses (n=10) (Wassenaar and Koehler, 2004). To correct the CH_3Cl $\delta^{37}Cl$ values relative to the Standard Mean Ocean Chloride (SMOC) reference (Kaufmann et al., 1989), standards were prepared using 200μL of Ocean Scientific Internal Stock Atlantic Seawater and G-10953 seawater (internal east coast seawater standard). There was no significant difference between the $\delta^{37}Cl$ values of both seawater samples. The Atlantic seawater used for this study was assumed to have a $\delta^{37}Cl$ of 0‰ with respect to SMOC. Multiple crushes of discrete samples produced notable ranges in $\delta^{37}Cl$, indicating internal heterogeneity for some samples (i.e. D152.2655) that most likely reflects the analysis of mixed fluid inclusion populations.

5.5 Sample and Fluid Inclusion Characteristics

In order to generate a viable interpretation of bulk geochemical data, it is essential to characterize the spatial and temporal variability of different fluid inclusion populations found within the sample material. Porphyry Cu deposits often have complex fluid histories with multiple and overprinting mineralization events and alteration types; on a microscopic level these distinct events can be represented by multiple generations of fluid inclusions with in a single host crystal. Furthermore, recent cathodoluminescence studies reveal complex growth histories for quartz veins and associated fluid inclusions from Bajo de la Alumbrera, Butte, and Bingham Canyon (Rusk and Reed, 2002; Harris et al., 2004; Redmond et al., 2004; Landtwing et al., 2005). In this case, the application of fluid inclusions requires careful petrographic and microthermometric studies to ascertain if a sample is appropriate for bulk fluid analysis (e.g., Bodnar, 1994). The current bulk geochemical study focused on pristine magmatic fluids; therefore by targeting drill core specimens from deep within the deposits (e.g., potassic zones of alteration) it has been possible on a first order basis to minimize the likelihood of supergene overprinting and to limit the analyses of multiple fluid inclusion generations. Current microthermometric measurements and petrographic observations of fluid inclusion assemblages were used to identify the dominant fluid inclusion populations within each sample vein, and in turn to define the salinity budget in produced leachates.

5.5.1 Butte, Montana

Butte pre-Main Stage and Main Stage fluid inclusions types are categorized as B35, B60, B85, B15H, B20, and $B20_{(MS)}$ following the classification scheme of Rusk (2003). Populations of B35, B60, and $B20_{(MS)}$ inclusion types dominate fluid inclusion leachates in this study (**Figure 4-1**). These inclusions are inferred to represent an aqueous, low-salinity, parental magmatic fluid that has not experienced fluid un-mixing. Results of current petrographic and microthermometric studies are similar to previous studies for Butte (Rusk, 2003; Rusk et al., 2004). Current homogenization temperatures and salinities are reported below, and summarized trapping temperatures, pressures, and CO_2-contents are from Rusk (2003). Sample numbers refer to drill hole and corresponding depth respectively.

B35 inclusions dominate the salinity budget (>90%) in two pre-Main Stage quartz-molybdenite veins (11172-1871 and 11172-3740) with K-feldspar alteration selvages. B35 inclusions are defined by 30-50 vol.% vapor at room temperature, and typically display negative euhedral to subhedral crystal shape. These inclusions are low-salinity (4-7 wt.% NaCl equivalent) with significant CO_2 contents (3-8 mol %), and homogenize to the liquid phase between 330-350 °C. Rusk (2003) estimates that fluid trapping occurred between temperatures of 575 and 650°C and pressures of 2 to 2.5 kbar (corresponding to 6-8 km under lithostatic pressures).

B60 inclusions are dominant in two quartz veins from the zone of pervasive sericitic alteration (PG-alteration; 11052-6215 and 11052-7025), and one barren quartz vein with a potassic alteration

envelope (11135-4967). B60 inclusions are defined by 50-70 vol% vapor at room temperature, and are negative crystal to equant in shape. Similar to B35 inclusions, fluids in B60 inclusions are low-salinity (4-8 wt.% NaCl equivalent) and CO_2-bearing (4-9 mol %). B60 inclusions homogenize to liquid, vapor, or critically at slightly higher temperatures between 360 to 390 °C, with estimated fluid trapping temperatures of 370 to 420°C and pressures of 400 to 800 bar (~4-8 km under lithostatic pressures; Rusk, 2003).

$B20_{(MS)}$ inclusions were studied in quartz veins from the central and peripheral zones of Main Stage mineralization (CZ-1, AL2, and X3564). Sample CZ-1 is from the central zone, and is dominated by enargite, covellite, pyrite, and quartz. AL2 and X3564 are from the Main Stage periphery, and are dominated by galena, sphalerite, rhodochrosite, and quartz. $B20_{(MS)}$ inclusions contain 10-30 vol% vapor at room temperature, and fluids are low-salinity (1-5 wt.% NaCl equivalent). In contrast to B35 and B60 inclusions, $B20_{(MS)}$ inclusions contain minimal CO_2 (0-2 mol%). These inclusions homogenize to liquid between 210-350 °C, and were likely trapped at temperatures below 350°C (Rusk, 2003).

5.5.2 Bingham Canyon, Utah

Late quartz-molybdenite and quartz-pyrite-sericite veins from Bingham are dominated by intermediate density fluid inclusions (**Figure 4-2**). Similar to Butte, these inclusions are inferred to represent an aqueous, low-salinity, CO_2-bearing, parental magmatic fluid that has not experienced un-mixing (Redmond et al., 2004; Landtwing et al., 2005). These inclusions are defined by 30 to 50% vapor at room temperature, are euhedral to rounded subhedral negative crystal in shape, and often contain either a small opaque (e.g. chalcopyrite) or a translucent daughter that is not halite. Previous studies of intermediate density inclusions are limited (Redmond et al., 2004; Landtwing et al., 2005), and these inclusions appear to be limited to the deep areas of the deposit. Redmond et al. (2004) suggest that there is a critical depth at 500m below the QMP ore body where intermediate density inclusions can be found, and that vapor-rich and brines inclusions are rare below this point. Samples in this study support these findings in that vapor-rich and brine inclusions are rare in sampled veins from deep within the potassic zone of alteration. Previous studies estimate that intermediate density inclusions were trapped at temperatures between 470 to 590 °C and pressures of 910 bar lithostatic pressure (assuming a 5 wt.% NaCl equivalent solution; Redmond et al., 2004).

Intermediate density inclusions are dominant (>95%) in late quartz-molybdenite and quartz-pyrite-sericite veins from the potassic zone of alteration. Quartz-molybdenite veins contain minor amounts of pyrite and chalcopyrite, and are associated with biotite-alkali-feldspar alteration envelopes often with minor sericite overprinting, whereas quartz-pyrite veins are associated with diffuse or intense sericite alteration selvages. Intermediate density inclusions dominate these samples (>95 %), along with rare brine and vapor-inclusions. These inclusions homogenize to vapor or by pseudocritical behavior (Bodnar, 1994) between 350 and 470 °C, and fluids are low to moderate salinity (1-13 wt.%

NaCl equivalent). Liquid CO_2 was not observed in any intermediate density inclusions, although cooling to –30 to –35 °C formed clathrate in almost all inclusions. For these inclusions, salinity estimates were calculated using the equations presented by Diamond (1992). Measured melting temperatures in six inclusions of –56.6 ± 0.1°C in which a solid phase formed upon cooling indicate CO_2 is the predominant gas.

5.6 Results

The Br/Cl ratios and $\delta^{37}Cl$ values for fluid inclusions leachates are presented in **Table 4-1**. Where multiple crushes were taken for samples, values are reported as averages.

5.6.1 Halogens Ratios

5.6.1.1 Butte, Montana

The Br/Cl ratios from pre-Main stage samples, which are dominated by B35 and B60 inclusions range from 0.60 to 1.08 $x10^{-3}$ M (**Figure 5-1**). Two samples associated with early pre-Main Stage pervasive sericitic alteration have Br/Cl ratios of 0.81 and 1.08 $x10^{-3}$ M, whereas samples from potassic alteration yield distinctly lower Br/Cl ratios of 0.60 and 0.64 $x10^{-3}$ M. These data are comparable with the Br/Cl ratios from the B20 inclusion-dominated Main Stage veins, which range in value from 0.92 to 1.88 $x10^{-3}$ M. All the data are comparable to the previous study of halogen ratios in Butte fluid inclusions by Irwin and Roedder (1995). The samples mostly have ratios less than seawater (1.54 $x10^{-3}$ M) and roughly overlap mantle values (~ 1-2 $x10^{-3}$ M) defined by diamond and mid-ocean ridge basalts (Deruelle et al., 1992; Jambon et al., 1995; Johnson et al., 2000).

5.6.1.2 Bingham Canyon, Utah

The Br/Cl values in bulk fluid inclusion leachates from Bingham are highly variable, and have values above and below previously published ratios (Irwin and Roedder, 1995; Kendrick et al., 2001). Br/Cl for late quartz-molybdenite and quartz-pyrite-sericite veins from the potassically altered host monzonite range from 0.18-3.68 x 10^{-3} M (**Figure 5-1**). Quartz-molybdenite veins and later quartz-pyrite-sericite veins have a similar spread in Br/Cl ranging from 0.41-1.09 x 10^{-3} M 0.18-0.88 x 10^{-3} M respectively. These ratios are well below seawater and roughly correspond to published Br/Cl data for global fumarole condensates (Böhlke and Irwin, 1992; and references therein), although there are no systematic variations in the halogen data with vein type or drill hole depth with the exception of two deep vein samples (D420.4710 and D420.5079.5) which have distinctly Br-enriched values of 2.52 and 3.68 x 10^{-3} M. A single barren quartz vein (D152.2655) from the younger mineralizing QMP with pervasive argillic overprinting has a Br/Cl of 0.64 x 10^{-3} M.

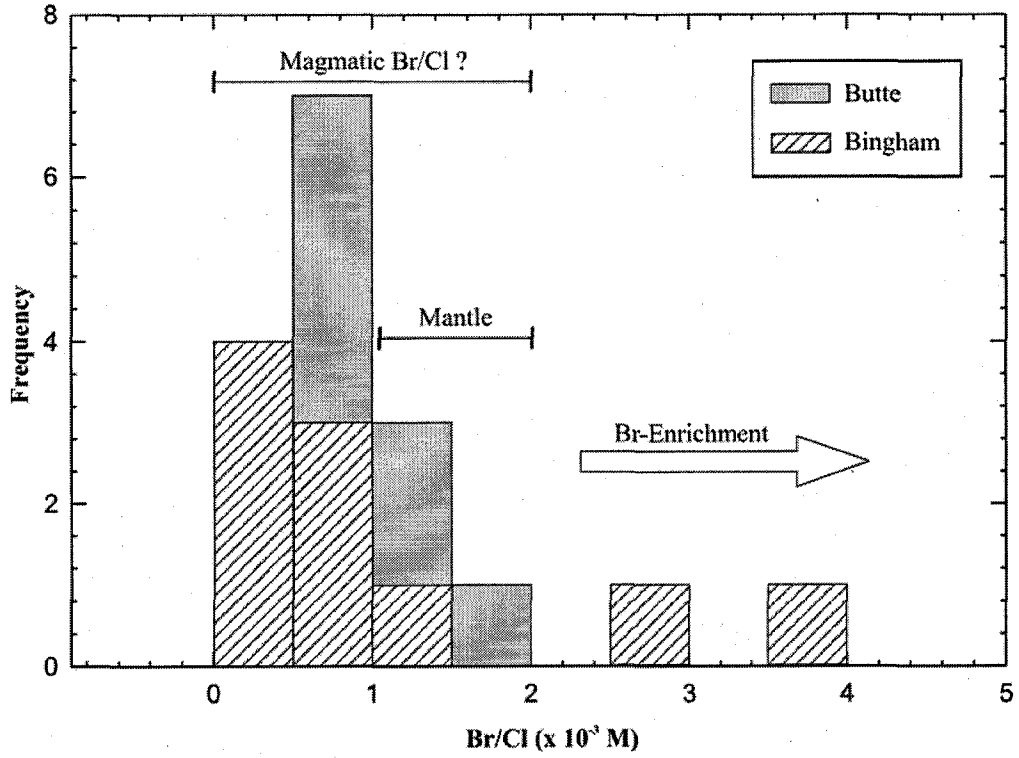

Figure 5-1: Elemental Br/Cl ratios for Butte and Bingham Canyon porphyry deposits. Br/Cl ratios for Butte fluid inclusion leachates are less than seawater (1.54 $x10^{-3}$ M), roughly overlap mantle values (~ 1-2 $x10^{-3}$ M) defined by diamond and mid-ocean ridge basalts (Deruelle et al., 1992; Jambon et al., 1995; Johnson et al., 2000), and are consistent with a juvenile magmatic component for both pre-Main Stage and Main Stage mineralization. Br/Cl ratios for Bingham Canyon fluid inclusion leachates are variable, extending both above and below the magmatic Br/Cl range. A comparison of Bingham Canyon Br/Cl ratios to a juvenile "magmatic signature" suggests that additional or alternative sources of salinity are present within the magmatic-hydrothermal system, or that either crystallization of Cl-bearing silicates or halite precipitation has modified the Br-concentration of juvenile fluids. Magmatic Br/Cl range is compiled from previous studies of magmatic-hydrothermal systems (Böhlke and Irwin, 1992; Banks et al., 2000a,b; Kendrick et al., 2001).

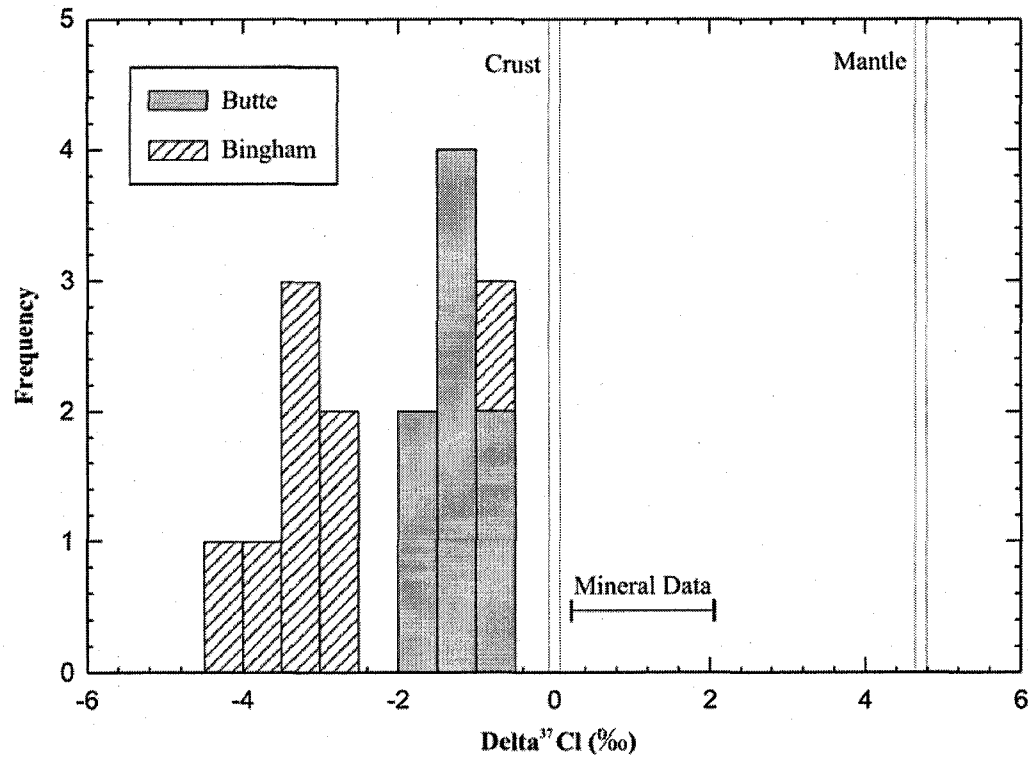

Figure 5-2: $\delta^{37}Cl$ values for Butte and Bingham Canyon porphyry deposits. $\delta^{37}Cl$ values between pre-Main Stage and Main Stage quartz veins at Butte are confined to a narrow range, indicating a common source of salinity for both ages of mineralization. Late quartz-molybdenite and quartz-pyrite-sericite veins from Bingham Canyon are also confined to a narrow range in $\delta^{37}Cl$ values, but cluster towards more negative Cl-isotopic compositions. Sample D415.2936 is an exception because it contains abundant low temperature secondary inclusions, and the higher $\delta^{37}Cl$ value (-0.9 ‰) may reflect either a different original source of salinity (e.g., crustal) or overprinting by a later fluid of different isotopic composition. The low $\delta^{37}Cl$ values for both deposits suggest that either a fractionation occurs between exsolved aqueous magmatic fluids and Cl-bearing silicates such as amphibole and mica, or the magmatic systems responsible for the formation of each deposit originally had a bulk $\delta^{37}Cl$ content that was negative. All reported $\delta^{37}Cl$ values are lower than either the proposed crustal and mantle Cl-isotopic compositions (0 ‰ and +4.7 ‰) defined by studies of seawater, evaporites, and mid-ocean ridge basalts (Magenheim et al., 1995). Mineral data are compiled from previous studies of magmatic biotite at Bingham Canyon (Eastoe and Guilbert, 1992).

5.6.2 Chlorine Isotopes

5.6.2.1 Butte, Montana

$\delta^{37}Cl$ values in fluid inclusion leachates from pre-Main Stage and Main Stage quartz veins range from –0.8 to -2.0 ‰, and are the first reported stable chlorine isotopic compositions for Butte fluids (**Figure 5-2**). The earliest veins, associated with potassic alteration (B35 dominated) have a narrow spread in $\delta^{37}Cl$ values between –0.8 to –1.3 ‰. Veins from the pervasive sericitic alteration zone (B60 dominated) have a similar range in values of –1.3 to –1.6 ‰. Central and peripheral Main Stage veins ($B20_{(MS)}$ dominated) have $\delta^{37}Cl$ values from –1.1 to –2.0 ‰ that overlap pre-Main Stage samples. All reported $\delta^{37}Cl$ values are lower than either the proposed crustal and mantle isotopic compositions (0 ‰ and +4.7 ‰) defined by studies of seawater, evaporites, and mid-ocean ridge basalts (Magenheim et al., 1995).

5.6.2.2 Bingham Canyon, Utah

In contrast to Butte, $\delta^{37}Cl$ values for quartz veins from the potassically altered monzonite host at Bingham (intermediate density dominated) are enriched in the lighter isotope, ranging from –0.9 to –4.1 ‰ (Figure 6). Quartz-molybdenite veins are narrowly confined between –3.1 to –3.4 ‰. In comparison, quartz-pyrite-sericite veins have similar $\delta^{37}Cl$ values ranging from –2.6 to –4.0 ‰, with the exception of one sample (D415.2936) that was subject to low temperature overprinting with a $\delta^{37}Cl$ value of –0.9 ‰. The single sample from the younger QMP (D152.2655), containing mixed intermediate density and brine inclusions, had the lightest value of –4.4 ‰, and is the lowest reported isotopic composition reported for magmatic-hydrothermal fluid inclusion studies, thus far. All reported $\delta^{37}Cl$ values are significantly lower than proposed crustal and mantle isotopic compositions (0 ‰ and +4.7 ‰), and previously reported values for minerals and fluids at Bingham (Eastoe et al., 1989; Eastoe and Guilbert, 1992).

5.7 Discussion

5.7.1 Halogens

Br/Cl ratios for fluid inclusions leachates extracted from pre-Main Stage and Main stage quartz veins at Butte range from 0.60 to 1.88 $x10^{-3}$ M, and all data is comparable to the previous study of halogen ratios in Butte fluid inclusions by Irwin and Roedder (1995). The samples have ratios less than seawater (1.54 $x10^{-3}$ M) and roughly overlap mantle values (~ 1-2 $x10^{-3}$ M) defined by diamond and mid-ocean ridge basalts (Deruelle et al., 1992; Jambon et al., 1995; Johnson et al., 2000). It has been previously suggested that magmatic fluids may be characterized by Br/Cl ratios less than that of seawater, specifically well defined between 0.5 to 1.0 $x10^{-3}$ M (Böhlke and Irwin, 1992; Banks et al., 2000a,b; Kendrick et al., 2001). As a whole, Br/Cl ratios for fluid inclusion leachates from Butte are

consistent with a "magmatic halogen signature", implying a juvenile magmatic component for both pre-Main Stage and Main Stage fluids.

Br/Cl ratios for fluid inclusion leachates extracted from quartz-molybdenite and quartz-pyrite-sericite veins from Bingham Canyon range between 0.18-3.68 × 10^{-3} M, and the single quartz vein (D152.2655) from the QMP has a Br/Cl ratio of 0.64 x 10^{-3} M. In contrast to Butte, Br/Cl ratios at Bingham Canyon are highly variable, extending both above and below previously reported ratios (Irwin and Roedder, 1995; Kendrick et al., 2001). Br-enriched values above seawater for samples D420.4710 and D420.5079.5 imply either the involvement of formation water derived from the sedimentary country rock (mixing or overprinting) or the crystallization of Cl-bearing phases (e.g. biotite, amphibole, or apatite) prior to volatile exsolution causing formation of a Br-enriched juvenile magmatic brine (Irwin and Roedder, 1995). The same effect could also be generated by the direct precipitation of halite from hydrothermal fluids, resulting in a "halite effect" where significant Cl is incorporated into the crystal lattice and Br is effectively excluded (Cloke and Kesler, 1979). As discussed below, the δ^{37}Cl values for samples D420.4710 and D420.5079.5 are similar to the rest of the Bingham Canyon leachates implying that Br-enrichment did not affect resultant Cl-isotopic compositions. In contrast, low Br/Cl ratios for samples D415.2936 and D415.2982.5 may be accounted for by crustal contamination or overprinting by Br-poor meteroic water. This is supported by the presence of abundant dilute low temperature secondary inclusions in these samples, and that the δ^{37}Cl value of –0.9 ‰ for sample D415.2936 is significantly closer to a crustal composition. As a whole, a comparison of Bingham Canyon Br/Cl ratios to a juvenile "magmatic signature" suggests that additional or alternative sources of salinity are present within the magmatic-hydrothermal system, or that either crystallization of Cl-bearing silicates or halite precipitation has modified the Br-concentration of juvenile fluids.

5.7.2 Chlorine Isotopes

This study reports the first stable chlorine isotopic compositions for Butte fluids (-0.8 to -2.0 ‰), and the lowest reported δ^{37}Cl values for Bingham Canyon (-0.9 to -4.4 ‰) and hydrothermal fluid inclusions in general, thus far. δ^{37}Cl values obtained for fluid inclusion leachates from Butte and Bingham quartz veins contrast with previously reported values for porphyry copper deposit samples that are confined to ± 1 ‰ of seawater (Eastoe et al., 1989; Eastoe and Guilbert, 1992). The preliminary results of these earlier studies suggest that chlorine isotopes might be fractionated between aqueous fluids and Cl-bearing silicates (e.g. amphibole), as well as between vapor and brine phases during fluid un-mixing. However, it was difficult to interpret the results of these studies in terms of chloride source because brine end-member inclusions dominated the salinity budget of leachates, and analytical techniques resulted in the analysis of multiple fluid inclusion populations (e.g., ~250-500g quartz required for crushing). The current δ^{37}Cl analyses of parental magmatic fluid inclusions from

Butte and Bingham better reflect the origin of salinity for the ore-forming fluid in these deposits because the possible isotopic effects related to fluid un-mixing are avoided.

$\delta^{37}Cl$ values between pre-Main Stage and Main Stage quartz veins at Butte are confined to a narrow range (-0.8 to -2.0 ‰), indicating a common source of salinity for both ages of mineralization. Because there is no deviation of $\delta^{37}Cl$ values towards crustal values, results do not support the involvement of external fluids during mineralization unless these fluids were dilute meteoric waters that did not significantly affect the bulk chlorine-isotope budget. Based on the Br/Cl ratios for Butte that fall within the previously suggested magmatic range, it is likely that the low $\delta^{37}Cl$ values at Butte also reflect a juvenile magmatic origin as a source of salinity for B35, B60, and $B20_{(MS)}$ inclusions.

Similar to Butte, late quartz-molybdenite and quartz-pyrite-sericite veins from Bingham Canyon are confined to a narrow range in $\delta^{37}Cl$ values from (-2.6 to –4.1 ‰), with the exception of sample D415.2936 (-0.9 ‰). The Br/Cl ratios for most leachates from Bingham Canyon also fall within the previously suggested magmatic range, so it is likely that the low $\delta^{37}Cl$ values also reflect a juvenile magmatic origin as a source of salinity for intermediate density fluid inclusions. Sample D415.2936 is an exception because it contains abundant low temperature secondary inclusions. Thus, the higher $\delta^{37}Cl$ value may reflect either a different original source of salinity (e.g., crustal), or from overprinting by a later fluid of different isotopic composition.

5.7.3 Chlorine Source in Porphyry Deposits

The low $\delta^{37}Cl$ values for both deposits suggest that either fractionation occurs between exsolved aqueous magmatic fluids and Cl-bearing silicates such as amphibole and mica, or the magmatic systems responsible for the formation of each deposit originally had a bulk $\delta^{37}Cl$ content that was negative. The first scenario is supported by recent theoretical modeling of Cl-isotope partitioning between brines and silicates (Schauble et al., 2003). Schauble et al. (2003) show that by using $MnCl_2$ and $FeCl_2$ as analogues for structurally bound Cl^- in amphiboles and micas, silicates can have $\delta^{37}Cl$ values up to ~2 to 3 ‰ higher than co-existing NaCl-dominated brines at room temperature. On a qualitative basis, this theoretical fractionation agrees with observed systematics for hydrothermally altered crust where Cl-rich amphiboles and smectite minerals have characteristically higher $\delta^{37}Cl$ values than seawater (Magenheim et al., 1994; Magenheim et al., 1995). Ransome et al. (1995) showed that subduction-zone pore waters have strongly negative $\delta^{37}Cl$ values (up to ~ -8 ‰) as compared to seawater, and these findings are also consistent with the partitioning of ^{37}Cl into silicate minerals.

At this point, this theory is partially ambiguous because it is unknown what an appropriate Cl-isotope behavior would be for an exsolved supercritical phase. If this phase were to behave similar to NaCl-saturated liquid water, it would have a low $^{37}Cl/^{35}Cl$ ratio, and this is supported by current findings. However, if it were to behave more like HCl vapor, the fractionation would be reversed resulting in a higher $\delta^{37}Cl$ value (Schauble et al., 2003). In addition, it is not known whether or not

these inferred fractionations are applicable to the high temperatures of the porphyry environment, but limited $\delta^{37}Cl$ values for magmatic biotite at Bingham Canyon range up to + 1.7 ‰ supporting the partitioning of chloride between aqueous fluids and silicate phases (**Figure 5-2**; Eastoe and Guilbert, 1992). Large equilibrium fractionations of >1 ‰ seem unlikely at these temperatures, unless there is extensive fractional removal of chlorine from the fluid. This may be viable for the Bingham system, in that unaltered monzonite is anomalously rich in chlorine (Parry, 1972), and that magmatic biotite contains several times more chlorine than that of hydrothermal biotite (Eastoe and Guilbert, 1992).

In terms of original source of chlorine in these magmatic systems, $\delta^{37}Cl$ values for both Butte and Bingham Canyon fall below previously determined isotopic compositions for the crustal (0 ‰) and the mantle (+4.7 ‰) reservoirs (Magenheim et al., 1995). Based on these isotopic compositions, a mantle reservoir for chloride is unlikely because the fractionation required to reach these $\delta^{37}Cl$ values is unrealistically large. Alternatively, because this mantle isotopic composition was calculated from studies of MORB, this value may not reflect the mantle composition in a subduction zone tectonic regime. Recently, a significantly different mantle value of -0.08 ‰ has been proposed based on studies of primitive MORB, carbonaceous chondrites, halite nodules in kimberlite, and fresh carbonatites (Sharp et al., 2005). This mismatch between determined mantle values might suggest that the mantle may have heterogeneous Cl-isotopic compositions similar to $\delta^{18}O$, therefore further studies targeting the Cl-isotopic composition of melt inclusions or eclogite may provide a more suitable end-member composition for porphyry systems. Based on halogen data, if either a crustal or a –0.08 ‰ mantle value is assumed as an original source for chloride, then it may be possible to account for the observed $\delta^{37}Cl$ values as discussed above. However, if such a large fractionation is not possible at magmatic temperatures, then this implies an alternative source of salinity. Such a source (~ -2 to -6 ‰) is currently unknown, although highly negative subduction zone pore waters or serpentinites (e.g., Sharp and Barnes, 2004) may provide such a reservoir if they are effectively recycled to depth (e.g., not expelled at the fore-arc), and the negative Cl-isotopic signature is preserved to the porphyry environment.

Cl-isotope geochemistry is still in its infancy, and further studies of temperature-controlled water-rock fractionation are required to confirm the isotopic effects of various processes within a magmatic-hydrothermal system. By constructing a crude chlorine budget between fluids and silicate minerals in a hydrothermal system, it may be possible to back calculate an empirical Rayleigh-type fractionation factor to address whether high temperature fractionation can account for the observed negative $\delta^{37}Cl$ values at Butte and Bingham Canyon. A more in depth study is required to address the Cl-isotopic composition of melt inclusions and both magmatic and hydrothermal hydrous minerals to further characterize the fluid history in these systems. In addition, vapor and brine end-member dominated leachates need to be studied to determine the quantitative isotopic effects of phase separation.

5.9 Conclusions

In this study, we have minimized the likelihood of late-stage meteoric overprinting to limit the analyses of multiple fluid inclusion generations, and analyzed the halogen and stable chlorine isotope composition of parental magmatic fluid inclusions. Elemental Br/Cl ratios for fluid inclusion leachates were determined by ion chromatography, and $\delta^{37}Cl$ values were obtained on the same leachates using CF-IRMS. We analyzed low-salinity fluid inclusions from Butte and Bingham that were trapped as a single-phase, supercritical, CO_2-bearing, aqueous fluid. Resultant data suggest a juvenile source of salinity in parental hydrothermal fluids related to porphyry deposit formation.

CHAPTER 6
CONCLUSIONS

A bulk fluid inclusion geochemical study has been carried out on a suite of quartz veins from two separate porphyry copper deposits: Butte, Montana, U.S.A, and Bingham Canyon, Utah, U.S.A. Halogen ratios (Br/Cl) of fluid inclusion leachates were determined by ion chromatography, and $\delta^{37}Cl$ values of the leachates were measured by continuous-flow isotope-ratio mass spectrometry (CF-IRMS). This study presents a scientifically viable analytical technique for the determination of $\delta^{37}Cl$ values in dilute natural samples (< 0.2 mg AgCl), and therefore provides an alternative to using TIMS for $\delta^{37}Cl$ determinations in fluid inclusions. Analyzed samples were dominated by low-salinity parental magmatic fluid inclusions that were trapped as a single-phase aqueous fluid in the one-phase field of the $NaCl-H_2O$ system. Resultant data provide insight into the source of salinity in parental magmatic-hydrothermal fluids related to porphyry deposit formation. In addition, the data also suggest that a significant partitioning of ^{35}Cl and ^{37}Cl occurs between Cl-bearing silicates and NaCl-dominated aqueous brines. Ultimately, this study shows the potential of Cl-isotopes to deduce the source of chloride and fluid history in these systems, as well as providing insight into the global geochemical cycle of chlorine. The main findings of this work are summarized as follows:

1. Current geochemical studies have produced one of the largest halogen datasets for fluid inclusions, and further extends the range in Br/Cl ratios for magmatic-hydrothermal systems. Elemental Br/Cl ratios have a relatively narrow range of values at each porphyry deposit, with the exception of four samples from Bingham Canyon (0.18 - 3.68 x 10^{-3}M) that extend both above and below the previously suggested halogen signature for magmatic-hydrothermal systems; these ratios overlap with the range determined in mantle fluids indicating salinity was derived primarily from a juvenile source.

2. Stable chlorine isotopic determinations via CF-IRMS have produced one of the largest datasets for magmatic-hydrothermal fluids, as well as the lowest $\delta^{37}Cl$ values reported for fluid inclusions. Fluid inclusion leachates were dominated by low-salinity parental magmatic fluid inclusions, and $\delta^{37}Cl$ values (-1 to –4 ‰) are lower than the proposed values for both the crust (0 ‰) and the mantle (4.7 ‰). The low $\delta^{37}Cl$ values for both deposits suggest that either a fractionation occurs between exsolved aqueous magmatic fluids and Cl-bearing silicates such as amphibole and mica, or the magmatic systems responsible for the formation of each deposit originally had a bulk $\delta^{37}Cl$ content that was negative. Alternative sources of bulk salinity may include subduction zone pore waters or ocean floor serpentinites if they are effectively recycled to depth, and the negative Cl-isotopic signature is preserved to the porphyry environment.

BIBLIOGRAPHY

Babcock, R.C., Jr, Ballantyne, G.H., and Phillips, C.H. (1997): Summary of the geology of the Bingham district, Utah (reprint) In: John, D.A. and G.H. Ballantyne (Ed.), Geology and Ore Deposits of the Oquirrh and Wasatch Mountains, Utah, Guidebook Series of the Economic Geologists vol.29, pp.133-145.

Bakker, R.J. (1997): Clathrates: computer programs to calculate fluid inclusion V-X properties using clathrate melting temperatures. Comput. Geoscience 23 (1), 1-18.

Banks, D.A. and Yardley, B.W.D. (1992): Crush-leach analysis of fluid inclusions in small natural and synthetic samples. Geochimica et Cosmochimica Acta 56, 245-248.

Banks, D.A., Green R., Cliff A., and Yardley B.W.D., (2000a): Chlorine isotopes in fluid inclusions: Determination of the origins of salinity in magmatic fluids. Geochimica et Cosmochimica Acta, 1785-1789.

Banks, D.A., Gleeson S.A., and Green R. (2000b): Determination of the origin of salinity in granite-related fluids: evidence from chlorine isotopes in fluid inclusions. Journal of Geochemical Exploration 69-70, 309-312.

Beane, R.E. and Titley, S.R. (1981): Porphyry copper deposits part II. Hydrothermal alteration and mineralization. Economic Geology 75th Anniversary volume, 235-269.

Belkin, H.E. (1994): Microthermometric investigations: Th and Tm. Practical and theoretical aspects. In: De Vivo, B. and Frezzotti, M.L. (Ed.), Fluid Inclusions in Minerals, pp.7-23.

Bodnar, R.J. (1994): Philosophy of fluid inclusion analysis. In: De Vivo, B. and Frezzotti, M.L. (Ed.), Fluid Inclusions in Minerals, pp.1-6.

Bodnar, R.J. and Vityk, M.O. (1994): Interpretation of microthermometric data for H_2O-NaCl fluid inclusions. In: De Vivo, B. and Frezzotti, M.L. (Ed.), Fluid Inclusions in Minerals, pp.117-130.

Böhlke, J.K. and Irwin, J.J. (1992): Laser microprobe analyses of Cl, Br, I, and K in fluid inclusions: Implications for sources of salinity in some ancient hydrothermal fluids. Geochimica et Cosmochimica Acta 56, 203-225.

Bowman, J.R., Parry, W.T., Kropp, W.P., and Kruer, S.A. (1987): Chemical and isotopic evolution of hydrothermal solutions at Bingham, Utah. Economic Geology 82, 395-428.

Brimhall, G. (1977): Early fracture disseminated mineralization at Butte, Montana. Economic Geology 72, 37-59.

Brimhall, G. (1980): Deep hypogene oxidation of porphyry copper potassic silicate protore at Butte, Montana: a theoretical evaluation of the copper remobilization hypothesis. Economic Geology 75, 384-409.

Burnham, C.W. (1979): Magmas and hydrothermal fluids. In: Barnes, H.L., (Ed.), Geochemistry of Hydrothermal Ore Deposits, Third Ed. Wiley, New York, pp. 71-136.

Chesley, J.T. and Ruiz, J. (1997): Preliminary Re-Os dating on molybdenite mineralization from the Bingham Canyon porphyry copper deposit, Utah. In: John, D.A. and G.H. Ballantyne (Ed.), Geology and Ore Deposits of the Oquirrh and Wasatch Mountains, Utah, Guidebook Series of the Economic Geologists vol.29, pp.133-145.

Cline, J.S. and Bodnar, R.J. (1991): Can economic porphyry copper mineralization be generated by a typical calc-alkaline melt? Journal of Geophysical Research 96, 8113-8125.

Cloke, P.L. and Kesler, S. (1979): The halite trend in hydrothermal solutions. Economic Geology 74, 1823-1831.

Deino, A. and Keith, J.D. (1997): Ages of volcanic and intrusive rocks in the Bingham district, Utah. In: John, D.A. and G.H. Ballantyne (Ed.), Geology and Ore Deposits of the Oquirrh and Wasatch Mountains, Utah, Guidebook Series of the Economic Geologists vol.29, pp.133-145.

Deruelle, B., Dreibus, G., and Jambon, A. (1992): Iodine abundances in oceanic basalts: implications for Earth dynamics. Earth and Planetary Science Letters 108, 217-227.

Diamond, L.W. (1992): Stability of CO_2 clathrate hydrate + CO_2 liquid + CO_2 vapor + aqueous KCL-NaCl solutions: experimental determination and application to salinity estimates of fluid inclusions. Geochimica et Cosmochimica Acta 56, 273-280.

Dilles, J.H., Reed., M., Roberts, S., Zhang, L., and Houston, R. (1999): Early magmatic-hydrothermal features related to the porphyry copper mineralization at Butte, Montana. Geological Society of America Bulletin 31, 382.

Eastoe, J.C., Guilbert, J.M., and Kaufman, R.S. (1989): Preliminary evidence for fractionation of stable chlorine isotopes in ore-forming hydrothermal systems. *Geology* 17, 285-288.

Eastoe, J.C. and Guilbert, J.M. (1992): Stable chlorine isotopes in hydrothermal processes. Geochimica et Cosmochimica Acta 56, 4247-4255.

Eggenkamp, H.G.M., Kreulen R., and Koster van Groos, A.F. (1995): Chlorine stable isotope fractionation in evaporites. Geochimica et Cosmochimica Acta 59, 5169-5175.

Gleeson, S.A. (2003): Bulk analysis of electrolytes in fluid inclusions. Fluid Inclusions: Analysis and Interpretation, Short Course Series 32, pp. 233-246.

Godon, A., Jendrzejewski, N., Eggenkamp, H.G.M., Banks, D.A., Ader, M., Coleman, M.L, and Pineau, F. (2004): A cross-calibration of chlorine isotopic measurements and suitability of seawater as the international reference material. Chemical Geology 207 (1-2), 1-12.

Goldstein, R.H. and Reynolds, T.J. (1994): Systematics of Fluid Inclusions in Diagenetic Minerals, Society for Sedimentary Geology, 199 pp.

Gustafson, L.B. and Hunt, J.P. (1975): The porphyry deposits at El Salvador, Chile. Economic Geology 70, 857-912.

Harris, A.C., Kamenetsky, V.S., White, N.C., and Steele D.A. (2004): Volatile phase separation in silicic magmas at Bajo de la Alumbrera porphyry Cu-Au deposit, NW Argentina. Resource Geology 54, 341-356.

Hedenquist, J.W. and Richards, J.P. (1998): Influence of geochemical techniques on porphyry copper genesis. In: Richards, J.P. and Larson, P.B. (Ed.), Techniques in Hydrothermal Ore Deposits Geology, Reviews in Economic Geology 10, pp.195-234.

Hedenquist, J.W., Arribas, A., and Reynolds, J. (1998): Evolution of an intrusion-centered hydrothermal system: Far Southeast-Lepanto porphyry and epithermal Cu-Au deposits, Philippines. Economic Geology 93, 373-404.

Heinrich, C.A., Driesner, T., Stefansson, A., and Seward, T.M. (2004): Magmatic vapor contraction and the transport of gold from the porphyry environment to epithermal ore deposits. Geology 32,

761-764.

Honda, F. (1970): A possible process for the fluctuation of halogen abundances in fumarolic gases. Geochemical Journal 3, 187-200.

Irwin, J.J. and Roedder, E. (1995): Diverse origins of fluid in magmatic inclusions at Bingham (Utah, USA), Butte (Montana, USA), St.Austell (Cornwall, UK), and Ascension Island (mid-Atlantic, UK), indicated by laser microprobe analysis of Cl, K, Br, I, BA + Te, U, Ar, Kr, and Xe. Geochimica et Cosmochimica Acta 59, 295-312.

Jambon, A., Deruelle, B., Dreibus, G., and Pineau, F. (1995): Chlorine and bromine abundance in MORB; the contrasting behavior of the Mid-Atlantic Ridge and the East Pacific Rise and implications for chlorine geodynamic cycle. Chemical Geology 126, 101-117.

Johnson, L.H., Burgess, R., Turner, G., Milledge, J.H., and Harris, J.W. (2000): Noble gas and halogen geochemistry of mantle fluids: comparison of African and Canadian diamonds. Geochimica et Cosmochimica Acta 64, 717-732.

Kaufmann, R.S., Long A., Bentley, H. and Davis, S. (1984): Natural chlorine isotope variations. Nature 309, 338-340.

Keith, J.D., Whitney, J.A., Hattori, K.H., Ballantyne, G.H., Christiansen, E.H., Barr, D.L., Cannon, T.M., and Hook, C.J. (1997): The role of magmatic sulfides and mafic alkaline magmas in the Bingham and Tintic mining districts, Utah. Journal of Petrology 38, 1679-1690.

Kendrick, M.A., Burgess, R.A., Pattrick, D. and Turner, G. (2001): Fluid inclusion noble gas and halogen evidence on the origin of Cu-porphyry mineralizing fluids. Geochimica et Cosmochimica Acta 65, 2651-2668.

Klepper, M.R. (1973): Geology of the southern part of the Boulder Batholith. Economic Geology 68, 907.

Landtwing, M.R., Pettke, T., Halter, W.E., Heinrich, C.A., Redmond, P.B., Einaudi, M.T., and Kunze, K. (2005): Copper deposition during quartz dissolution by cooling magmatic-hydrothermal fluids: The Bingham Porphyry. Earth and Planetary Science Letters 235, 229-243.

Lanier, G., John, E.C., Swensen, A.J., Reid, J., Bard, C.E., Caddey, S.W., and Wilson J.C. (1978): General geology of the Bingham mine, Bingham Canyon, Utah. Economic Geology 73, 1228-1241.

Long, A., Eastoe, C.J., Kaufmann, R.S., Martin, J.G., Wirt, L. and Finely, J.B. (1993): High-precision measurement of chlorine stable isotope ratios. Geochimica et Cosmochimica Acta 57, 2907-2912.

Lowell, J.D. and Guilbert, J.M. (1970): Lateral and vertical alteration-mineralization zoning in porphyry ore deposits. Economic Geology 65, 373-408.

Lund, K., Aleinikoff, J.N., Kunk, M.J., Unruh, D.M., and Zeihen, G.D. (2002): SHRIMP U-Pb and Ar-40/Ar-39 age constraints for relating plutonism and mineralization in the Boulder Batholith region, Montana. Economic Geology 97, 241-267.

Magenheim, A.J., Spivack, A.J., Michael, P.J. and Gieskes, J.M. (1995): Chlorine stable isotope composition of the oceanic crust: Implications for the Earth's distribution of chlorine. Earth and Planetary Science Letters 131, 417-432.

Magenheim, A.J., Spivack, A.J., Volpe, C., and Ransome, B. (1994): Precise determination of stable chlorine isotopic-ratios in low-concentration natural samples. Geochimica et Cosmochimica Acta 58, 3117-3121.

Martin M.W., Dilles, J.H., and Proffet, J.M. (1999): U-Pb geochronologic constraints for the Butte porphyry system. GSA abstracts with programs vol.31 (A-380).

Miller, R.N. (1973): Production history of the Butte district and geological function, past and present. Economic Geology 68, 908.

Meyer, C. (1965): An early potassic type of alteration at Butte, Montana. American Mineralogist 50, 1717-1722.

Meyer, C., Shea, E., and Goddard, C.C. (1968): Ore deposits at Butte, Montana. In: Ore deposits of the United States 1933-1967: New York, Am. Inst. Min. Metal. Petrol. Eng., vol.2, pp. 1373-1416.

Moore, W.J. (1978): Chemical characteristics of hydrothermal alteration at Bingham, Utah. Economic Geology 73, 1260-1269.

Moore, W.J. and Nash, J.T. (1974): Alteration and fluid inclusion studies of the porphyry copper ore body at Bingham, Utah. Economic Geology 69, 631-645.

Musashi, M., Markl, G., and Kreulen, R. (1998): Stable chlorine-isotope analysis of rock samples: New aspects of chlorine extraction. Analytica Chimica Acta 362, 261-269.

Parry, W.T. (1972): Chlorine in biotite from basin and range plutons. Economic Geology 67, 972-975.

Parry, W.T., Wilson, P.N., Moser, D., and Heizler, M.T. (2001): U-Pb dating of zircon and 40Ar/39Ar dating of biotite at Bingham Canyon, Utah. Economic Geology 96, 1671-1683.

Ransome, B., Spivack, A.J., Kastner, M. (1995): Stable Cl isotopes in subduction-zone pore waters: implications for fluid-rock reactions and the cycling of chlorine. Geology 23, 715-718.

Redmond, P., Einaudi, M.T., Inan, E.E., Landtwing, M.R., and Heinrich, C.A. (2004): Copper deposition by fluid cooling in intrusion-centered systems: new insights from the Bingham porphyry ore deposit, Utah. Geology 32, 217-220.

Roedder, E. (1984). Fluid Inclusions. Rev. Miner. 12 (646 pp.).

Rusk, B. and Reed, M. (2002): Scanning electron microscope-cathodoluminescence analysis of quartz reveals complex growth histories in veins from the Butte porphyry deposit, Montana. Geology 30, 727-730.

Rusk, B.G. (2003): Cathodoluminescent quartz textures and fluid inclusions in veins of the porphyry copper-molybdenum deposit in Butte, Montana: Constraints on the physical and chemical evolution of the hydrothermal system. Unpubl. PhD dissert., Univ. of Oregon. 235 pp.

Rusk B.G., Reed, M., Dilles, J.H., Klemm, L.M., and Heinrich, C.A. (2004): Composition of magmatic hydrothermal fluids determined by LA-ICP-MS of fluid inclusions from the porphyry copper-molybdenum deposit at Butte, MT. Chemical Geology 210, 173-199.

Schauble, E.A., Rossman, G.R., and Taylor, H.P. (2003): Theoretical estimates of equilibrium chlorine-isotope fractionations. Geochimica et Cosmochimica Acta 67, 3267-3281.

Sharp, Z.D. and Barnes J.D. (2004): Water-soluble chlorides in massive seafloor serpentinites: a source of chloride in subduction zones. Earth and Planetary Science Letters 226 (1-2): 243-254.

Sharp, Z.D., Barnes, J.D., Brearley, A.J., Chaussidon, M., and Van Zuilen, M. (2005): The global chlorine cycle over the last 3.7Ga; Chlorine Isotope Constraints. GSA abstracts with programs vol.37 (7).

Shepherd, T.J., Rankin, A.H., and Alderton, D.H.M. (1985): A practical guide to fluid inclusion studies. Blackie, London, 239.

Sillitoe, R.H. (1973): The tops and bottoms of porphyry-copper deposits. Economic Geology 67, 184-197.

Smedes, H.W. (1973): Regional geologic setting of the Boulder Batholith, Montana. Geology 68, 907.

Warnaars, F.W., Smith, W.H., Bray, R.E., Lanier, G., and Shafiqullah, M. (1978): Geochronology of igneous intrusions and porphyry copper mineralization at Bingham, Utah. Economic Geology 73, 1242-1249.

Wassenaar, L.I. and Koehler, G. (2004): An on-line technique for the determination of the $\delta^{37}Cl$ of inorganic and total organic Cl in environmental samples. Analytical Chemistry 76, 6384-6388.

Webster, J.D. (2004): The exsolution of magmatic hydrosaline chloride fluids. Chemical Geology 210 (1-4), 33-48.

Wood, S.A. and Samson, I.M. (1998): Solubility of ore minerals and complexation of ore metals in hydrothermal solutions. In: Richards, J.P. and Larson, P.B. (Ed.), Techniques in Hydrothermal Ore Deposits Geology, Reviews in Economic Geology 10, pp.33-80.

Xiao, Y.K. and Zhang, G.C. (1992): High-precision isotopic measurement of chlorine by thermal ionization mass spectrometry of the Cs_2Cl^+ ion. International Journal of Mass Spectrometry and Ion Processes 116, 183-192.

Xiao, Y.K., Zhou, Y.M., and Liu, W.G. (1995): Precise measurement of chlorine isotopes based on Cs_2Cl^+ by thermal ionization mass spectrometry. Analytical Letters 28, 1295-1304.

Yardley, B.W.D., S. Gleeson, S.Bruce and Banks, D.A. (2000): Origin of retrograde fluids in metamorphic rocks. Journal of Geochemical Exploration, 69-70, 281-285, 2000.

Yardley, B.W.D., Bennett, A., and Banks, D.A (2003): Controls on the Chemical Composition of Crustal Brines. Journal of Geochemical Exploration (78-79), 133-135.

APPENDIX A
SAMPLE PETROGRAPHY

This section contains hand sample and petrographic descriptions for studied host rock and quartz vein samples for Butte, Montana, U.S.A (**A1**) and Bingham Canyon, Utah, U.S.A (**A2**). Corresponding plates for hand samples and thin sections are found in **Appendix B.**

A1: Butte, Montana

Hand sample and drill core fragments from Butte included quartz veins from both the pre-Main Stage and Main Stage ages of mineralization. Pre-Main Stage samples included quartz-molybdenite veins with potassic alteration selvages, and quartz - pyrite - sericite veins from the zone of pervasive sericitic alteration. Main Stage veins included central (quartz - enargite - covellite - pyrite) and peripheral (galena - sphalerite - rhodochrosite - quartz) samples. These samples have been previously studied in detail and came with well constrained petrographic descriptions (e.g. Rusk, 2000; Rusk, 2004). No thin sections were prepared, and only hand sample descriptions are provided below.

11172-3740

This sample is a fragment of a quartz - molybdenite vein from the potassic alteration zone of the pre-Main Stage of mineralization (**Plate 1.A**). The vein is dominated by clear white quartz (>95 %), and displays a potassic alteration envelope along with anhydrite. The vein also contains biotite, molybdenite wisps, chalcopyrite specks, and calcite. Pyrite is predominately located along a thin line at the margin of the vein that follows an area of re-brake (sericite is locally associated). Dimensions are 38 mm X 18 mm X 27 mm.

11172-1871

This sample is a quartz - molybdenite vein from the potassic alteration zone of the pre-Main Stage of mineralization (**Plate 1.B**). The vein is dominated by clear white quartz (>95 %), and displays a potassic alteration envelope along with anhydrite. The vein also contains biotite, molybdenite, minor pyrite, and minor chalcopyrite. Upper veinlet in this sample contains a soft whitish mineral that does not effervesce that may be a later gypsum veinlet. Dimensions are 34 mm X 16 mm X 14 mm.

11135-4967

This sample is 3 fragments of a barren quartz vein from the potassic alteration zone of the pre-Main Stage of mineralization (**Plate 1.C**). The vein is dominated by coarse-grained white-grey quartz (>95 %) with minor specks of chalcopyrite, and displays a K-feldspar alteration envelope (biotite - K-

feldspar - sericite). Trace calcite and pyrite is also present in the sample. Dimensions of the fragments are 28 mm X 19 mm, 24 mm X 30 mm, and 7 mm X 20 mm.

11052-7025

This sample is a fragment of a meter-scale barren quartz vein from the pervasive sericitic alteration zone of the pre-Main Stage of mineralization (**Plate 1.D**). The only minerals found in the vein are quartz and pyrite. Quartz is medium to coarse grained and cloudy grey-white in color, along with minor specks of pyrite. Dimensions are 45 mm X 23 mm X 16 mm.

11052-6215

This sample is 3 fragments of a barren quartz vein from the pervasive sericitic alteration zone of the pre-Main Stage of mineralization (**Plate 1.E**). The only minerals found in the vein are medium to coarse-grained cloudy white quartz and minor specks of pyrite. Sample also contains four dusty vugs lined with sulfide along with small clear crystals of quartz (not sampled). Dimensions are 41 mm X 26 mm X 20 mm.

CZ1

This sample is from the central zone of the Main Stage of mineralization, and is dominated by quartz, enargite, pyrite, and covellite (**Plate 1.F**). Quartz in the central vein is grey-white in color with coarse subhedral to euhedral crystals. Small white-grey euhedral quartz crystals are intergrown with enargite (not sampled). Sulfides include coarse-grained enargite and pyrite with minor specks of covellite. Trace amounts of kaolinite and siderite are also present. Dimensions are 45 mm X 38 mm X 25 mm.

AL2

This sample is from the peripheral zone of the Main Stage of mineralization, and is dominated by galena, sphalerite, rhodochrosite, and quartz (**Plate 1.G**). Sample contains a large isolated vein dominated by white, anhedral, fine-grained quartz along with galena, sphalerite, and thin crosscutting veinlets of rhodochrosite. Dark regions are primarily composed of galena and quartz. Dimensions are 44 mm X 6 mm X 7 mm.

X3564

This sample is a vein fragment from the peripheral zone of the Main Stage of mineralization, and is dominated by galena, sphalerite, rhodochrosite, and quartz (**Plate 1.H**). Vein quartz is clear white in color, medium-grained, and associated with trace specks of sulfide. One side of the sample displays white-brown clay alteration. Dimensions are 26 mm X 16 mm X 27 mm.

Modoc-10649

This sample is a quartz vein from the late porphyritic Modoc intrusion and associated breccia. The central vein is dominated by quartz, pyrite, chalcopyrite, and molybdenite (**Plate 1.I**). Sericite and altered alkali-feldspar also present. The host breccia is comprised of a green-grey matrix, disseminated sulfides, and both unaltered and altered phenocrysts of alkali-feldspar. Dimensions are 88 mm X 48 mm X 34 mm.

A2: Bingham Canyon, Utah

Drill core slabs from Bingham Canyon included late quartz-molybdenite and quartz-pyrite-sericite veins from the host monzonite and main-mineralizing quartz monzonite porphyry (QMP). The mineralogy and alteration of the host monzonite has been previously described in detail and will only be briefly discussed below (Lanier et al., 1978; Moore, 1978; Babcock et al., 1997; Phillips et al., 1997). Petrography focused on vein mineralogy, textures, and associated alteration selvages. For all samples, the host rock was pervasively potassically-altered monzonite, with the exception of one sample from the QMP that was subject to argillic overprinting.

Host Monzonite

The sampled host monzonite at Bingham Canyon is fine-grained, sub-equigranular, and has been pervasively potassically-altered. Remnant magmatic augite is pale green to colorless, and is present as subhedral to euhedral crystals (up to 0.6 mm) that are rimmed to varying degrees by deuteric amphibole. Two types of amphibole are present: (1) late magmatic deuteric amphibole that is yellow-green with light green pleochroism and forms euhedral to anhedral pseudomorphs after augite (up to 0.4 mm) and (2) hydrothermal actinolite that is pale green, fibrous, frayed, or as rectangular laths (0.5 mm) that partially or totally replace augite. Hydrothermal actinolite is sometimes associated with minor calcite and epidote, and can be altered to clay minerals. Biotite is present as both magmatic relict phlogopite and as shreddy hydrothermal biotite. Magmatic relict phlogopite occurs as subhedral to euhedral grains (up to 1 mm across) with pale brown-red pleochroism and often hosts needle-like, intersecting crystals of sagenetic rutile. Saganetic rutile is inferred to have precipitated within the crystal structure during early hydrothermal alteration of Ti-bearing phlogopite (Moore, 1973). Hydrothermal biotite replaces actinolite, and occurs as small frayed yellow-brown to green pleochroic grains with a shreddy interlocking texture that generally form aggregates with fine-grained quartz and sulfides. In addition, some hydrothermal biotite can be chloritized to varying degrees. Magmatic alkali-feldspar occurs as interstitial anhedral grains, as well as larger phenocrysts with remnant perthitic texture. Hydrothermal alkali-feldspar occurs as rims around albite, as patch perthites with alkali-feldspar enveloping albite, and as a minor constituent of quartz - biotite replacement of albite. The perthitic texture formed by replacement of albite is distinctive for hydrothermal alkali-feldspar.

Relict magmatic albite occurs as subhedral to euhedral laths with remnant polysynthetic twinning and/or oscillatory zoning, and grain boundaries are commonly sutured with alkali-feldspar.

D415.2829.5

***Hand Sample*:** The host monzonite is fine-grained, sub-equigranular, and has been subject to pervasive potassic alteration. Pyrite is found as disseminations in the host, in thin pyrite-only veinlets, and within larger quartz-sulfide veins as subhedral to euhedral cubes. Two large veins (~10 mm wide) are found in this section: (1) a sub-planar white-grey quartz dominated vein with a weak pyrite centerline and (2) a more irregular vein containing clear-grey quartz, alkali-feldspar, and pyrite. These larger veins display potassic-alteration envelopes, and both contain trace amounts of calcite. Other veinlets (0.2 to 0.4 mm in width) present in this section contain quartz - pyrite or quartz - K-feldspar assemblages, and are irregular in orientation. Dimensions are 185 mm X 63 mm X 31 mm (**Plate 2.A**).

***Host Rock Thin Section*:** The host monzonite is pervasively altered to secondary hydrothermal alkali-feldspar with a dusty appearance in plane-polarized light. The host groundmass has abundant anhedral patches of alkali-feldspar with perthitic texture (patch perthites). Euhedral to anhedral albite laths (up to 0.8 mm in length) display obscured polysynthetic twinning, as well as sutured grain boundaries with secondary alkali-feldspar that are poorly defined and appear to blend together. Relict magmatic biotite grains (between 0.4 to 3.2 mm in length) are euhedral to subhedral in shape, and display pale red-brown pleochroism with sagenetic rutile visible as needle-like, intersecting crystals (**Plates 4.A** and **4.B**). Secondary hydrothermal biotite is pale yellow-brown in color, and is found as interlocking shreddy aggregates (**Plate 4.C**). Apatite is abundant, displaying euhedral cross-sections and acicular prismatic crystals found poikilitically enclosed in hydrothermal alkali-feldspar and magmatic phlogopite. Disseminated pyrite is abundant (commonly associated with hydrothermal biotite), along with minor chalcopyrite, and remnant magnetite. Other minerals include quartz, sericite, rutile, chlorite, epidote, and clay. Several quartz - calcite veinlets with biotite - alkali-feldspar alteration selvages are present, as well as a single wispy biotite-only veinlet.

***Vein Thin Section*:** This section contains the analyzed quartz vein for this sample. The central quartz vein (~10 mm wide) is associated with a diffuse sericite alteration selvage, and displays a complex centerline of medium to coarse-grained angular pyrite, along with minor amounts of calcite, radial dickite, and alkali-feldspar. Towards the margins of the vein, quartz grades into a microcrystalline mosaic texture with rounded and sutured grain boundaries (**Plate 4.D**). A thin offshoot of the central vein follows sub-parallel in orientation. Other veinlets include: (1) a quartz-only veinlet (0.2 mm wide) that is cut by (2) a quartz - calcite - pyrite veinlet (0.4 mm wide).

D415.2936

Hand Sample: The host monzonite is fine-grained, sub-equigranular, and has been subject to pervasive potassic alteration (abundant hydrothermal biotite and alkali-feldspar). A significant amount of clay minerals are observed (**Plate 4.G**). Some hydrothermal biotite is slightly altered to chlorite. Pyrite is found as disseminations in the host, in thin pyrite-only veinlets, and within larger quartz-sulfide veins. Diffuse sericite overprinting to the host rock is visible at the margins of quartz-sulfide veinlets. The central vein (6 mm wide) in this sample is composed of white-grey medium-grained subhedral to anhedral quartz, along with pyrite, and is cut by smaller pyrite-only and quartz - pyrite veinlets. Minor calcite is inferred by slight effervescence. Dimensions are 103 mm X 64 mm X 34 mm (**Plate 2.B**).

Vein Thin Section: This section contains the analyzed quartz vein for this sample. The central quartz vein (6 mm wide) is associated with a diffuse sericite envelope with minor anhydrite, and displays a discontinuous centerline of massive or angular pyrite. The central vein channel appears to have been re-used by a later vein (total of 8.8 mm width). This area of the vein was isolated and not sampled for analysis. Vein quartz displays a remnant comb texture, but has been highly recrystallized to microcrystalline mosaic quartz (**Plates 4.H** and **4.I**). Three smaller quartz - pyrite - sericite veins (~0.4 mm wide) are present that cut across the central vein.

D415.2982.5

Hand Sample: The host monzonite is fine-grained, sub-equigranular, and has been subject to pervasive potassic alteration (abundant hydrothermal biotite and alkali-feldspar). The central vein (10 to 15 mm wide) in this sample is vuggy and has dusty grey appearance. Vein quartz is diffuse, anhedral, and grey-white in color. Pyrite in the central vein is medium-grained and subhedral to anhedral in shape. Host rock adjacent to the central vein is light in color, and is altered to sericite and clay. Sample also contains several pyrite-only veinlets. Dimensions are 156 mm X 63 mm X 29 mm (**Plate 2.C**).

Vein Thin Section: This section contains the analyzed quartz vein for this sample. The large central vein (10 to 15 mm width) is diffuse, irregular, and is associated with an intense sericite and clay alteration envelope. Vein quartz is fine to coarse-grained, anhedral in shape, and has a dirty and dusty appearance; remnant euhedral growth zones are visible in areas (**Plate 5.D**). Quartz grains are either highly fractured with fresh sharp contacts, or have been recrystallized to a microcrystalline mosaic texture with sutured grain boundaries (**Plates 5.A**, **5.B**, and **5.C**). Pyrite is highly fractured and appears to be altered. Other veinlets include: (1) a quartz only (0.8mm wide) veinlets and (2) two thin quartz - pyrite - sericite offshoots from the central vein.

D415.3025

***Hand Sample*:** The host monzonite is fine-grained, sub-equigranular, and has been subject to pervasive potassic alteration (abundant hydrothermal biotite and alkali-feldspar). The central quartz vein in this sample contains a high concentration of coarse anhedral pyrite, calcite, and minor alkali-feldspar that is altered to sericite. Pyrite and chalcopyrite are found as disseminations in the host. Sample also contains multiple carbonate - pyrite veinlets that cut across the central vein. Dimensions are 96 mm X 64 mm X 31 mm (**Plate 2.D**).

***Host Rock Thin Section*:** The host monzonite is pervasively altered to secondary hydrothermal alkali-feldspar with a dusty appearance in plane-polarized light. The host groundmass has abundant anhedral patches of alkali-feldspar with perthitic texture (patch perthites). Euhedral to anhedral albite laths (up to 0.8 mm in length) display obscured polysynthetic and Carlsbad twinning (**Plate 6.C**), as well as sutured grain boundaries with secondary alkali-feldspar that are poorly defined and appear to blend together. Relict magmatic biotite grains (between 0.4 to 3.2 mm in length) are euhedral to subhedral in shape, and display pale red-brown pleochroism with sagenetic rutile visible as needle-like, intersecting crystals. Secondary hydrothermal biotite is pale yellow-brown in color, and is found as interlocking shreddy aggregates; some hydrothermal biotite is altered to chlorite. Hydrothermal actinolite that is altered to clay minerals forms pseudomorphs after augite (**Plate 6.B**). Apatite is abundant, displaying euhedral cross-sections and acicular prismatic crystals found poikilitically enclosed in hydrothermal alkali-feldspar and magmatic phlogopite. Disseminated pyrite is abundant (commonly associated with hydrothermal biotite), along with minor chalcopyrite, and remnant magnetite. Other minerals include quartz, sericite, rutile, chlorite, epidote, anhydrite (**Plate 6.A**), and clay. Veinlets include: (1) a thin irregular biotite-only veinlet that is cut by (2) a calcite - quartz - pyrite veinlet (0.5mm wide).

***Vein Thin Section*:** This section contains the analyzed quartz vein for this sample. The central quartz vein is associated with an intense sericite - quartz alteration selvage (**Plate 6.D**), and contains pyrite, calcite, and apatite. Vein quartz is coarse to fine-grained and euhedral to anhedral in shape (**Plate 6.E**). High undulatory extinction is observed in coarser grains indicating strain, and some grain boundaries are sutured or display triple-junctions. These grains are often closely associated with clusters of fine-grained recrystallized quartz (**Plate 6.E**). This section contains several veinlets and veins including: (1) thin irregular biotite-only veinlets, (2) quartz - calcite - pyrite veinlets (up to ~2.5 mm wide), (3) a calcite-only veinlet and (4) a quartz - pyrite - sericite veinlet (2 mm wide).

D415.3050

***Hand Sample*:** The host monzonite is fine-grained, sub-equigranular, and has been subject to pervasive potassic alteration (abundant hydrothermal biotite and alkali-feldspar). This sample contains a large central composite vein channel that has been re-used by 2 separate veins (13 mm wide), and is associated with a diffuse sericite alteration selvage. Pyrite is concentrated along a centerline towards

one margin of the vein channel. Abundant calcite is also present in the vein. Sample also contains small pyrite-only veinlets with biotite alteration selvages. Dimensions are 120 mm X 63 mm X 36 mm (**Plate 2.E**).

***Vein Thin Section*:** This section contains the analyzed quartz vein for this sample. The central vein is a composite of two vein forming events, and is associated with an intense sericite, quartz, and clay overprint along with disseminated pyrite (**Plate 7.A**). The original quartz - calcite vein displays both remnant comb and microcrystalline mosaic textures (**Plates 7.B and 7.C**). Larger grains in this region have sutured grain boundaries, and calcite shows visible euhedral growth zones. A later quartz - pyrite vein follows sub-parallel, and has re-used the original vein channel (**Plate 7.D**). Quartz grains are fine to coarse-grained and anhedral in shape with sutured boundaries, although some areas are highly fractured and fresh.

D420.4710

***Hand sample*:** The host monzonite is fine-grained, sub-equigranular, and has been subject to pervasive potassic alteration (abundant hydrothermal biotite and alkali-feldspar). The large central quartz vein contains molybdenite in a strong centerline and as wisps near the margins, minor calcite, and is associated with a diffuse sericite - quartz -clay alteration selvage. The sample also contains thin quartz - pyrite veinlets. Dimensions are 120 mm X 42 mm X 25 mm (**Plate 2.G**).

Vein Thin Section: This section contains the analyzed quartz vein for this sample. The large central vein (24 mm wide) contains quartz, molybdenite, calcite, and anhydrite, and is associated with a diffuse sericite alteration selvage. Vein quartz displays a crustiform pattern alternating from a microcrystalline mosaic texture at the margins, to comb texture, then back to fine-grained mosaic texture at the molybdenite centerline contact (**Plates 8.A and 8.B**). Molybdenite is concentrated in a strong centerline (0.4 to 0.6 mm wide), as faint wisps near the margins, and as randomly dispersed flakes. Calcite is located in fractures and as coarser isolated grains. Other veinlets include: (1) a quartz - calcite - anhydrite - chalcopyrite - pyrite - molybdenite veinlet with a sericite alteration envelope that runs sub-parallel to the central vein channel, and (2) thin veinlets containing pyrite, chalcopyrite, and minor quartz.

D420.5079.5

***Hand sample*:** The host monzonite is fine-grained, sub-equigranular, and has been subject to pervasive potassic alteration (abundant hydrothermal biotite and alkali-feldspar). Deuteric amphibole forms pseudomorphs after magmatic augite, and some albite laths are altered to sericite and calcite. The central vein contains clear grey to white quartz that grades from fine-grained subhedral to coarse subhedral from the margins towards the pyrite centerline. The pyrite centerline is slightly vuggy in

areas, and is associated with orange zeolite. Vein quartz displays comb texture with prismatic grains that are perpendicular to the vein walls. Other veinlets include: (1) thin wispy zeolite veinlets, (2) magnetite ± chalcopyrite and quartz veinlets, (3) carbonate-only veinlets, (4) biotite-only veinlets, (5) quartz - molybdenite veinlets, and (6) quartz - pyrite veinlets. Dimensions are 134 mm X 41 mm X 22 mm (**Plate 2.F**).

Host Thin Section: The host monzonite is pervasively altered to secondary hydrothermal alkali-feldspar with a dusty appearance in plane-polarized light (**Plate 8.E**). Euhedral to anhedral albite laths (up to 0.8 mm in length) display obscured polysynthetic and Carlsbad twinning, as well as sutured grain boundaries with secondary alkali-feldspar that are poorly defined and appear to blend together. Some albite is slightly altered to calcite. Relict magmatic biotite grains (between 0.4 to 3.2 mm in length) are euhedral to subhedral in shape, and display pale red-brown pleochroism with sagenetic rutile visible as needle-like, intersecting crystals. Secondary hydrothermal biotite is pale yellow-brown in color, and is found as interlocking shreddy aggregates; some hydrothermal biotite is altered to chlorite. Hydrothermal actinolite forms pseudomorphs after magmatic augite. Chalcopyrite, magnetite, molybdenite, bornite, and pyrite are found as disseminations in the host rock. Other minerals include rutile, epidote, thorite, zircon, monazite, illemnite, and apatite. This section also contains a strange veinlet that appears to be brecciated, and is composed of pyrite, flaky zeolite, and minor bornite (**Plate 8.F**).

Vein Thin Section: This section contains the analyzed quartz vein for this sample. The central vein (10 mm wide) contains quartz, pyrite, calcite, and aggregates of flaky zeolite, and is associated with a diffuse sericite alteration selvage. Vein quartz displays a crustiform pattern alternating from a microcrystalline mosaic texture at the margins, to comb texture, then back to fine-grained mosaic texture at the pyrite centerline contact (**Plate 8.G**). Angular pyrite that forms the centerline is rimmed by zeolite, amphibole, and sericite (**Plate 8.H**). Other veinlets include: (1) magnetite ± chalcopyrite veinlets that are thin and irregular with minor quartz infill, (2) a thin zeolite veinlet (0.2 mm wide) cut by another zeolite veinlet (0.4 mm wide), (3) a thin molybdenite - quartz veinlet, (4) and irregular carbonate-only veinlet (0.2 mm wide), and (5) a thin wispy biotite-only veinlet.

D430.3639

Hand sample: The host monzonite is fine-grained, sub-equigranular, and has been subject to pervasive potassic alteration (abundant hydrothermal biotite and alkali-feldspar). The central vein contains white-grey to clear grey quartz that ranges from subhedral to anhedral granular to subhedral to anhedral medium-grained (crustiform layering texture), along with chalcopyrite, molybdenite, pyrite, calcite, and anhydrite. Branching of the vein at the edge of the sample encloses a small portion of the host rock. Dimensions are 103 mm X 42 mm X 24 mm (**Plate 3.A**).

Vein Thin Section: This section contains the analyzed quartz vein for this sample. The central vein (11 mm wide) contains quartz, molybdenite, chalcopyrite, pyrite, calcite, and anhydrite, and is associated with a minor sericite and clay alteration selvage. Vein quartz displays a complex crustiform pattern, alternating between 3 sets of microcrystalline mosaic to comb texture layers (**Plates 9.A** and **9.B**). Individual quartz grains display undulatory extinction, and form sutured grain boundaries with surrounding crystals. Calcite is abundant near the central region of the vein as coarser isolated grains. The sample also contains thin and irregular calcite - anhydrite veinlets. Other minerals found in the host rock include rutile, monazite, epidote, apatite, zircon, and thorite.

D430.3768

Hand Sample: The host monzonite is fine-grained, sub-equigranular, and has been subject to pervasive potassic alteration (abundant hydrothermal biotite and alkali-feldspar). The host is highly fractured, and some hydrothermal biotite appears to be foliated. The large central vein contains quartz, molybdenite, chalcopyrite, calcite, and biotite. Vein quartz displays a crustiform pattern with alternating layers of microcrystalline mosaic to comb textures. Molybdenite is found along three linear wisps. Dimensions are 59 mm X 47 mm X 21 mm (**Plate 3.B**).

Vein Thin Section: This section contains the analyzed quartz vein for this sample. The central vein (24 mm wide) contains quartz, molybdenite, chalcopyrite, pyrite, calcite, and anhydrite, and is associated with a biotite - alkali-feldspar alteration selvage. Vein quartz displays a complex crustiform pattern, alternating between 2 sets of microcrystalline mosaic to comb texture layers (**Plate 9.C**). Quartz found in the microcrystalline bands is fine-grained and milky white in color, whereas comb quartz is coarser-grained and clear. Individual quartz grains display undulatory extinction, and form sutured grain boundaries with surrounding crystals. Molybdenite is located along wisps that follow the bands of microcrystalline quartz. Calcite fills thin fractures that cut across the vein channel. The sample also contains thin and irregular calcite - anhydrite veinlets. Other minerals found in the host rock include rutile, monazite, epidote, apatite, zircon, and thorite.

D152.2655

Vein Thin Section: This section contains the analyzed quartz vein for this sample. The QMP host rock has been subject to intermediate argillic alteration. Magmatic phlogopite is altered to clay minerals, appears to be sheared, and is associated with rutile (**Plate 10.A**). Hydrothermal biotite is also altered to sericite and clay (**Plate 10.B**). There are frequent voids in the thin section that represent the subsequent loss of sericite or clay that originally formed pseudomorphs after albite phenocrysts. The host rock also contains minor calcite and epidote. The central vein contains quartz, a thin line of pyrite, and minor chalcopyrite, magnetite, molybdenite, sericite, and calcite (**Plate 10.C**). Vein quartz

is clear grey and massive, appears to have been overprinted by a linear flow of fluid that is visible as multiple sub-parallel trails of secondary fluid inclusions that cut across grain boundaries (**Plate 10.D**). One side of the section contains a band of coarse scalenohedral calcite crystals with sharp terminations. Dimensions of the sampled quartz vein fragment are 48 mm X 43 mm X 28 mm (**Plate 3.C**).

D162.2991

Hand Sample: The host monzonite is fine-grained, sub-equigranular, and has been subject to pervasive potassic alteration (abundant hydrothermal biotite and alkali-feldspar). The sample contains a large central quartz - molybdenite vein (17 mm wide), and a vein offshoot (6 mm) that branches off enclosing a portion of the host rock. Some areas of the vein are vuggy, and quartz is white-grey medium-grained subhedral to fine-grained anhedral. Molybdenite is associated with a thin line of rebrake near the channel margin, and calcite is abundant (some vugs contains calcite rosettes). Based on the asymmetrical appearance of the vein channel, its appears that this vein may represent two separate vein-forming events. Other minerals include azurite and clay. Dimensions are 41 mm X 63 mm X 46 mm (**Plate 3.D**).

Vein Thin Section: This section contains the analyzed quartz vein for this sample. The large central vein (17 mm wide) contains quartz, molybdenite, chalcopyrite, pyrite, calcite, flaky zeolite, and anhydrite, and is associated with a biotite - alkali-feldspar - alteration selvage. Vein quartz is white-grey and coarse-grained with sutured grain boundaries; larger prismatic crystals display strong undulatory extinction, and others are highly fractured (**Plates 11.A and 11.B**). There are also some smaller fine-grained aggregates of recrystallized quartz. Molybdenite is present as thin wisps near the channel margins, and as randomly dispersed flakes. Other veinlets include: (1) a calcite-only veinlet that cuts across the large central vein, (2) a quartz - calcite veinlet that is cut by the central vein, and (3) a quartz-only veinlet.

D162.3367

Hand Sample: The host monzonite is fine-grained, sub-equigranular, and has been subject to pervasive potassic alteration (abundant hydrothermal biotite and alkali-feldspar). The central vein (10 mm wide) contains quartz, molybdenite, and calcite, and is associated with a biotite - alkali-feldspar alteration selvage. Vein quartz is white and fine-grained with a granular sacchroidal texture, and molybdenite is concentrated along a weak centerline. Other veinlets include: (1) a quartz-only veinlet cut by the central vein and (2) a complex veinlet containing chalcopyrite, molybdenite, bornite, quartz, zeolite, and calcite. Dimensions are 63 mm X 46 mm X 28 mm (**Plate 3.E**).

Host Thin Section: The host monzonite is fine-grained, sub-equigranular, and has been subject to pervasive potassic alteration (abundant hydrothermal biotite and alkali-feldspar). The host groundmass

has abundant anhedral patches of alkali-feldspar with perthitic texture (patch perthites). Secondary hydrothermal biotite is pale yellow-brown in color, and is found as interlocking shreddy aggregates **(Plates 11.C and 11.D)**. Deuteric amphibole is pale green-brown and pleochroic, and forms pseudomorphs after augite **(Plates 11.E** and **11.F)**. Fresher euhedral phenocrysts of augite are also present, and are rimmed to varying degrees by hydrothermal actinolite that is blue-green in color. Hydrothermal actinolite is also present as rectangular grains that are often associated with calcite. Disseminated pyrite is abundant (commonly associated with hydrothermal biotite), along with minor chalcopyrite, bornite and remnant magnetite. Other minerals include quartz, chlorite, rutile, titanite, zeolite, and apatite. Sample contains two irregular quartz - zeolite veinlets (1.5 mm wide) with biotite - alkali-feldspar selvages **(Plate 11.G)**.

Vein Thin Section: This section contains the analyzed quartz vein for this sample. The central vein (10 mm wide) contains quartz, molybdenite, calcite, and zeolite, and is associated with a biotite - alkali-feldspar alteration selvage. Vein quartz is white-grey subhedral to anhedral with a range in grain size from medium near the centerline to fine-grained with granular sacchroidal texture at the margins **(Plate 11.H)**. Coarser grains display either sutured grain boundaries or polygonal with triple junctions **(Plate 11.H)**. Molybdenite is concentrated in a weak centerline, and also as dispersed flakes throughout the vein. The section also contains a chevron shaped vein (1.6 to 2 mm wide) that is dominated by chalcopyrite rimmed by bornite, with minor amounts of quartz, calcite, zeolite, and molybdenite.

APPENDIX B
PLATES

Plate 1: Butte hand samples for pre-Main Stage, Main Stage, and Modoc quartz veins.

Plate 2: Bingham hand samples for DDH415 and DDH420 quartz veins.

Plate 3: Bingham hand samples for DDH430, DDH162, and DDH152 quartz veins.

Plate 4: Representative photographs for thin sections D415.2829.5 and D415.2936.

Plate 5: Representative photographs for thin section D415.2982.5.

Plate 6: Representative photographs for thin section D415.3025.

Plate 7: Representative photographs for thin section D415.3050.

Plate 8: Representative photographs for thin section D420.4710 and D420.5079.5.

Plate 9: Representative photographs for thin sections D430.3639 and D430.3768.

Plate 10: Representative photographs for thin section D152.2655.

Plate 11: Representative photographs for thin sections D162.2991 and D162.3367.

PLATE 1

1.A: This sample is a fragment of a quartz - molybdenite vein from the potassic alteration zone of the pre-Main Stage of mineralization (11172-3740).

1.B: This sample is a quartz - molybdenite vein from the potassic alteration zone of the pre-Main Stage of mineralization (11172-1871).

1.C: This sample is 3 fragments of a barren quartz vein from the potassic alteration zone of the pre-Main Stage of mineralization (11135-4967).

1.D: This sample is a fragment of a meter-scale barren quartz vein from the pervasive sericitic alteration zone of the pre-Main Stage of mineralization (11052-7025).

1.E: This sample is 3 fragments of a barren quartz vein from the pervasive sericitic alteration zone of the pre-Main Stage of mineralization (11052-6215).

1.F: This sample is from the central zone of the Main Stage of mineralization, and is dominated by quartz, enargite, pyrite, and covellite (CZ1).

1.G: This sample is from the peripheral zone of the Main Stage of mineralization, and is dominated by galena, sphalerite, rhodochrosite, and quartz (AL2).

1.H: This sample is from the peripheral zone of the Main Stage of mineralization, and is dominated by galena, sphalerite, rhodochrosite, and quartz (X3564).

1.I: This sample is a quartz vein from the late porphyritic Modoc intrusion and associated breccia (Modoc-10649).

PLATE 1

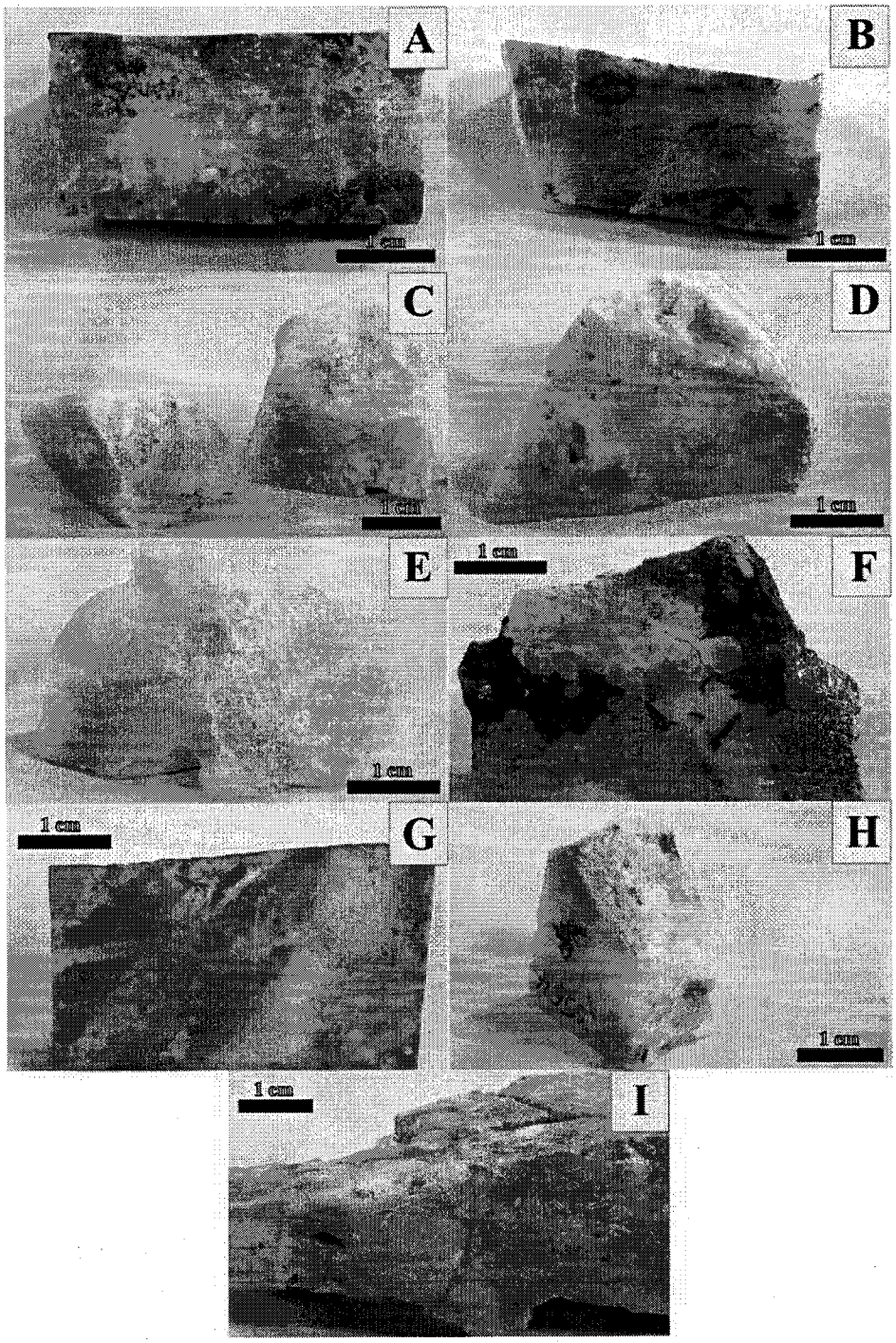

PLATE 2

2.A: This sample is a quartz - sulfide - faint alkali-feldspar vein from the potassic alteration zone with monzonite host (D415.2829.5).

2.B: This sample is a quartz - sulfide - alkali-feldspar vein from the potassic alteration zone with monzonite host (D415.2936).

2.C: This sample is a quartz - sulfide vein from the potassic alteration zone with monzonite host (D415.2982.5).

2.D: This sample is a quartz - sulfide vein from the potassic alteration zone with monzonite host (D415.3025).

2.E: This sample is a quartz - sulfide vein from the potassic alteration zone with monzonite host (D415.3050).

2.F: This sample is a quartz - sulfide - zeolite vein from the potassic alteration zone with monzonite host (D420.5079.5).

2.G: This sample is a quartz - molybdenite vein from the potassic alteration zone with monzonite host (D420.4710).

PLATE 2

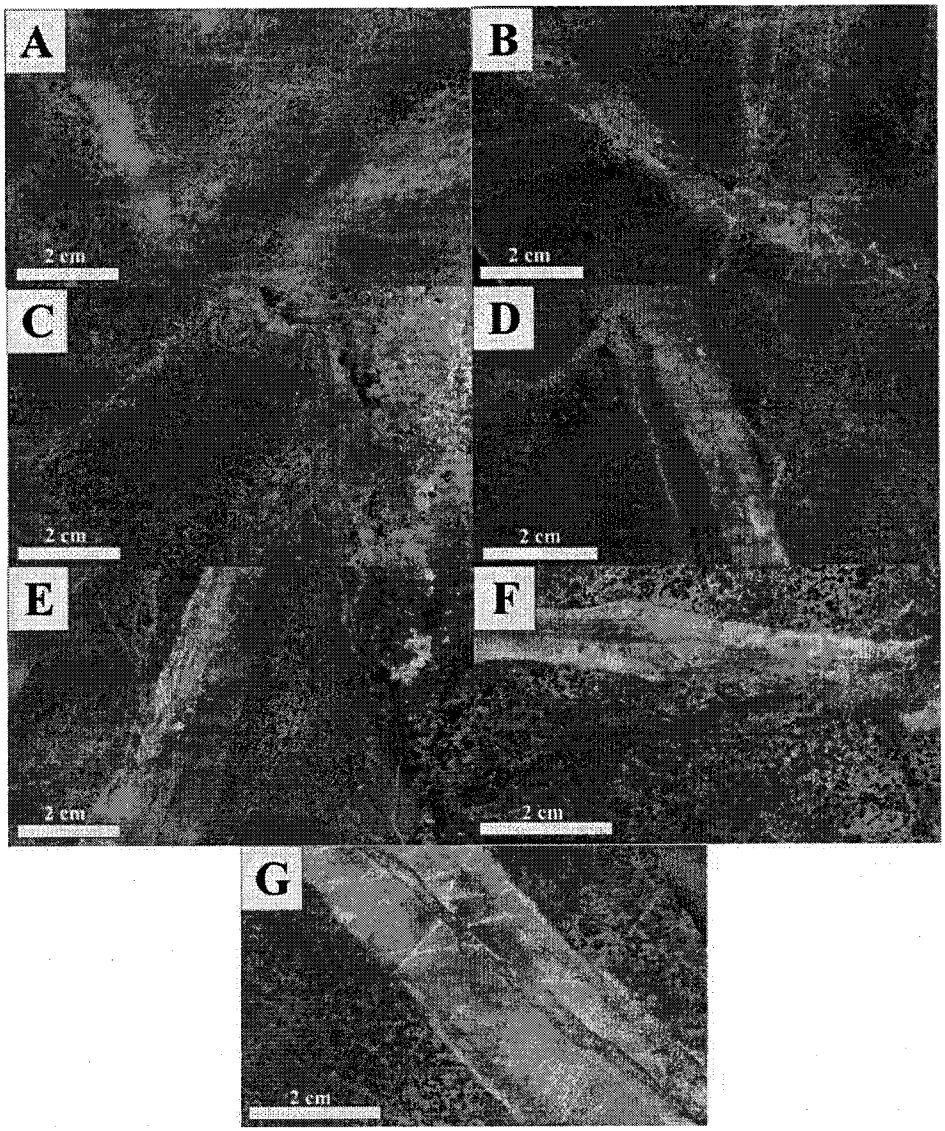

PLATE 3

3.A: This sample is a quartz - molybdenite - sulfide vein from the potassic alteration zone with monzonite host (D430.3639).

3.B: This sample is a quartz - molybdenite vein from the potassic alteration zone with monzonite host (D430.3768).

3.C: This sample is a quartz vein fragment from the QMP subject to intermediate argillic overprinting (D152.2655).

3.D: This sample is a quartz - molybdenite vein from the potassic alteration zone with monzonite host (D162.2991).

3.E: This sample is a quartz - molybdenite vein from the potassic alteration zone with monzonite host (D162.3367).

PLATE 3

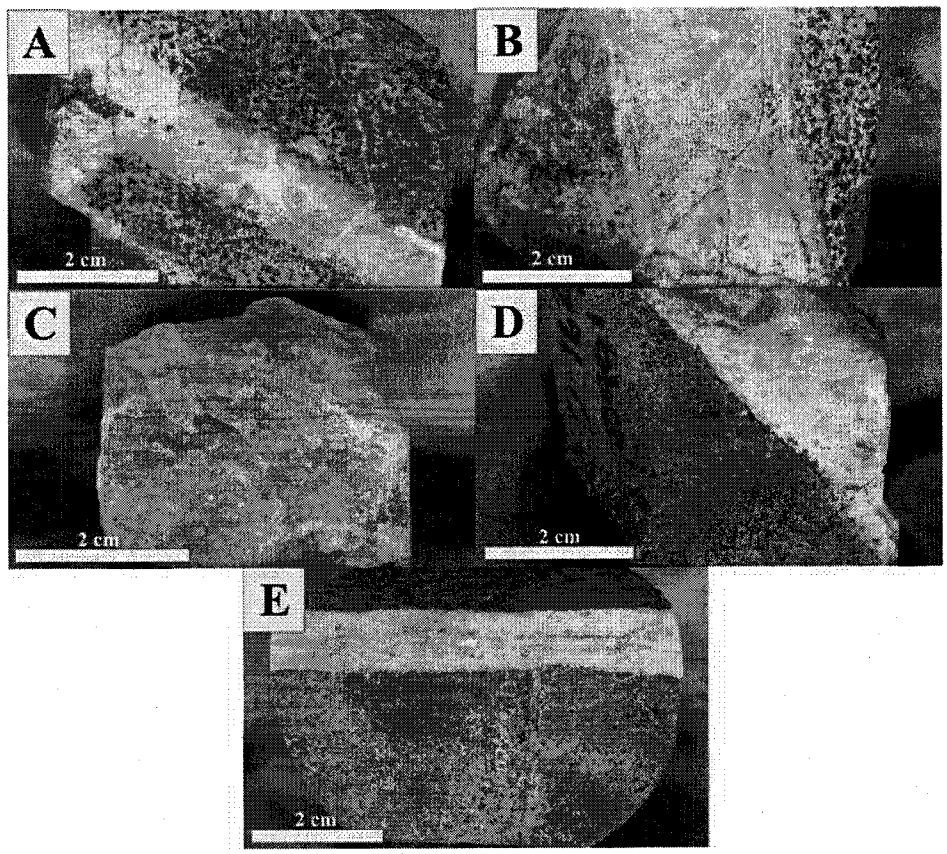

PLATE 4

4.A: Relict magmatic biotite grains (between 0.4 to 3.2 mm in length) are euhedral to subhedral in shape, and display pale red-brown pleochroism with sagenetic rutile visible as needle-like, intersecting crystals (crossed-polarized light; D415.2829.5).

4.B: Relict magmatic biotite grains (between 0.4 to 3.2 mm in length) are euhedral to subhedral in shape, and display pale red-brown pleochroism with sagenetic rutile visible as needle-like, intersecting crystals (plane-polarized light; D415.2829.5).

4.C: Secondary hydrothermal biotite is pale yellow-brown in color, and is found as interlocking shreddy aggregates (plane-polarized light; D415.2829.5).

4.D: Quartz displaying microcrystalline mosaic texture with rounded and sutured grain boundaries (crossed-polarized light; D415.2829.5).

4.E: Intracrystalline brine and intermediate density fluid inclusions (plane-polarized light; D415.2829.5).

4.F: Diffuse intracrystalline cluster of brine and intermediate density fluid inclusions (plane-polarized light; D415.2829.5).

4.G: Overprinting of the host monzonite by clay minerals (plane-polarized light; D415.2936).

4.H: Vein quartz displays a remnant comb texture, but has been highly recrystallized to microcrystalline mosaic quartz (crossed-polarized light; D415.2936).

4.I: Vein quartz displays a remnant comb texture, but has been highly recrystallized to microcrystalline mosaic quartz (crossed-polarized; light D415.2936).

4.J: Diffuse intracrystalline cluster of brine and intermediate density fluid inclusions (crossed-polarized light; D415.2936).

PLATE 4

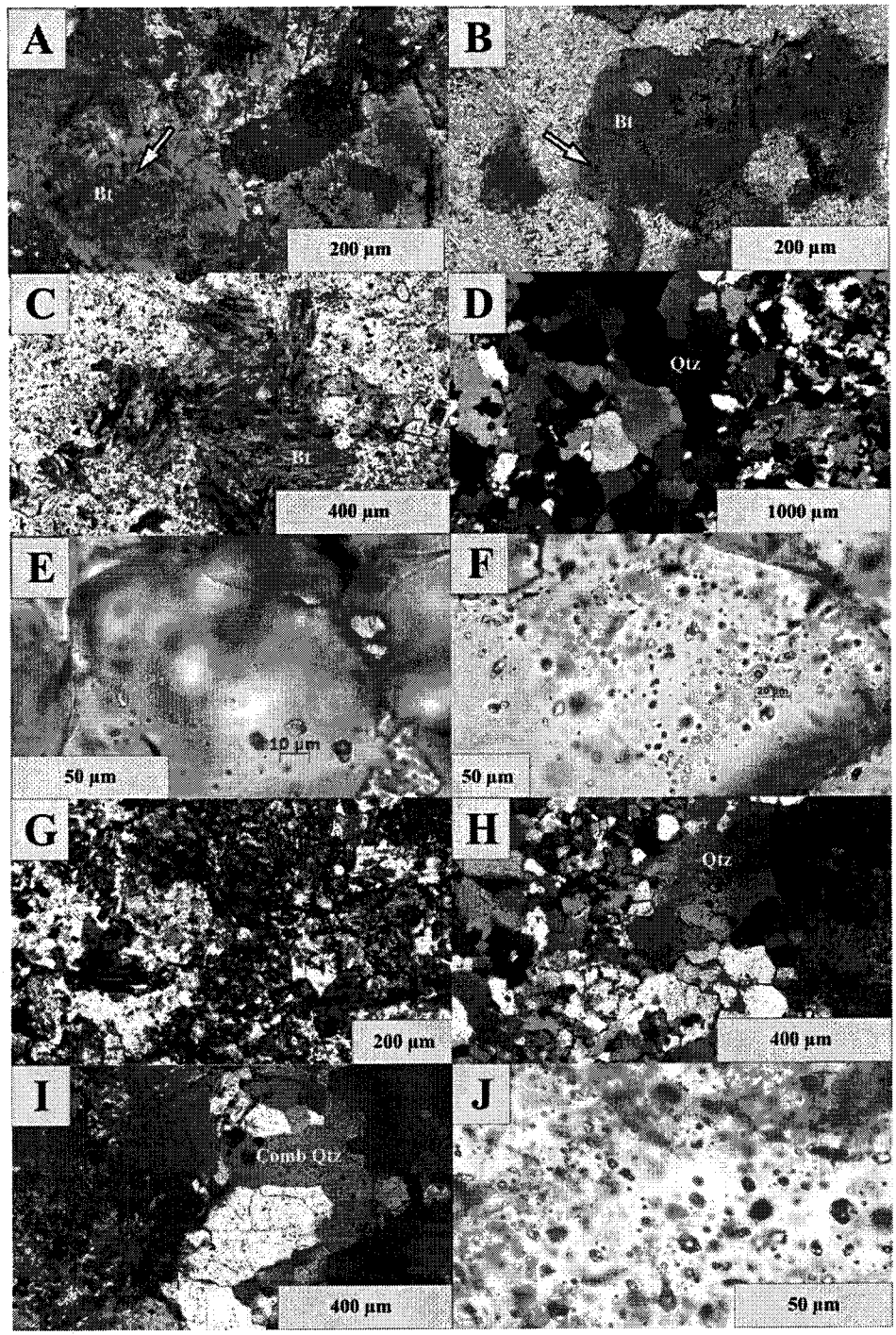

PLATE 5

5.A: Quartz grains displaying sutured grain boundaries (crossed-polarized light; D415.2982.5).

5.B: Quartz grains have been recrystallized to a microcrystalline mosaic texture with sutured grain boundaries (crossed-polarized light; D415.2982.5).

5.C: Quartz grains are highly fractured with fresh sharp contacts (crossed-polarized light; D415.2982.5).

5.D: Primary fluid inclusions located along growth zones (crossed-polarized light; D415.2982.5).

5.E: Primary fluid inclusions located along growth zones with intracrystalline intermediate density inclusions (plane-polarized light; D415.2982.5).

5.F: Primary fluid inclusions located along growth zones with intracrystalline intermediate density inclusions (plane-polarized light; D415.2982.5).

PLATE 5

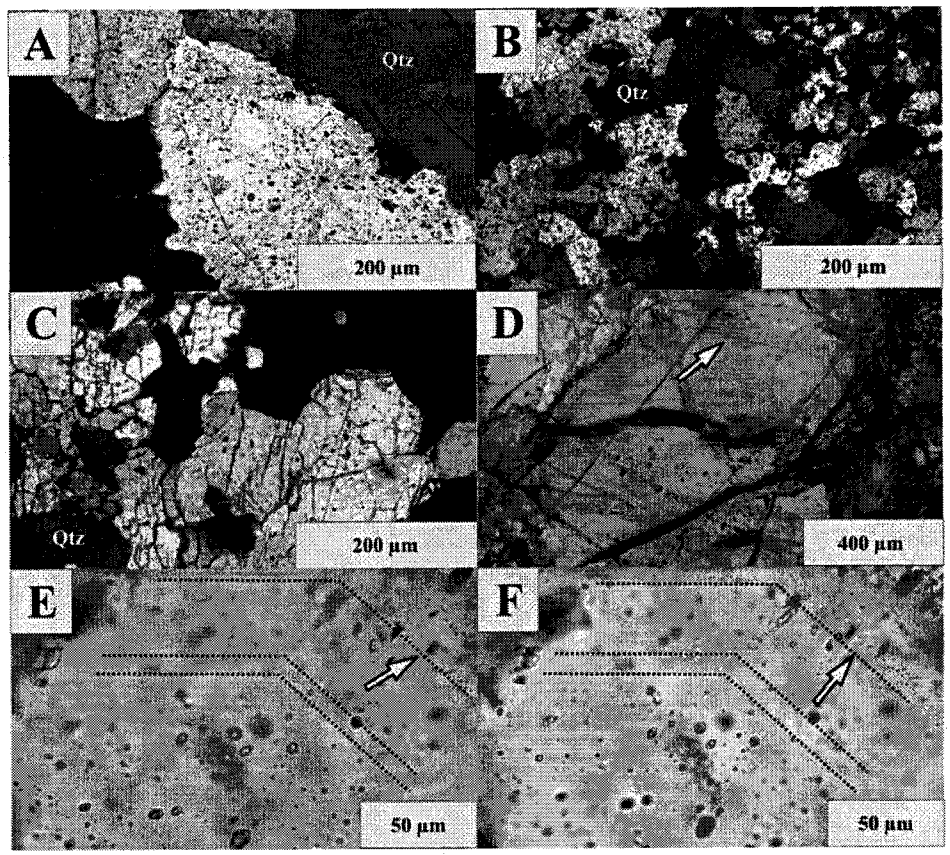

PLATE 6

6.A: Anhydrite grain within the host monzonite (crossed-polarized light; D415.3025).

6.B: Hydrothermal actinolite that is altered to clay minerals forms pseudomorphs after augite (plane-polarized light; D415.3025).

6.C: Euhedral to anhedral albite laths (up to 0.8 mm in length) display obscured polysynthetic and Carlsbad twinning (crossed-polarized light; D415.3025).

6.D: The central quartz vein is associated with an intense sericite - quartz alteration selvage (crossed-polarized light; D415.3025).

6.E: High undulatory extinction is observed in coarser grains of quartz indicating strain, and some grain boundaries are sutured or display triple-junctions. These grains are often closely associated with clusters of fine-grained recrystallized quartz (crossed-polarized light; D415.3025).

6.F: Intermediate density and brine inclusions with euhedral to rounded subhedral negative crystal shape (plane-polarized light; D415.3025).

6.G: Brine inclusions with euhedral to rounded subhedral negative crystal shape (plane-polarized light; D415.3025).

PLATE 6

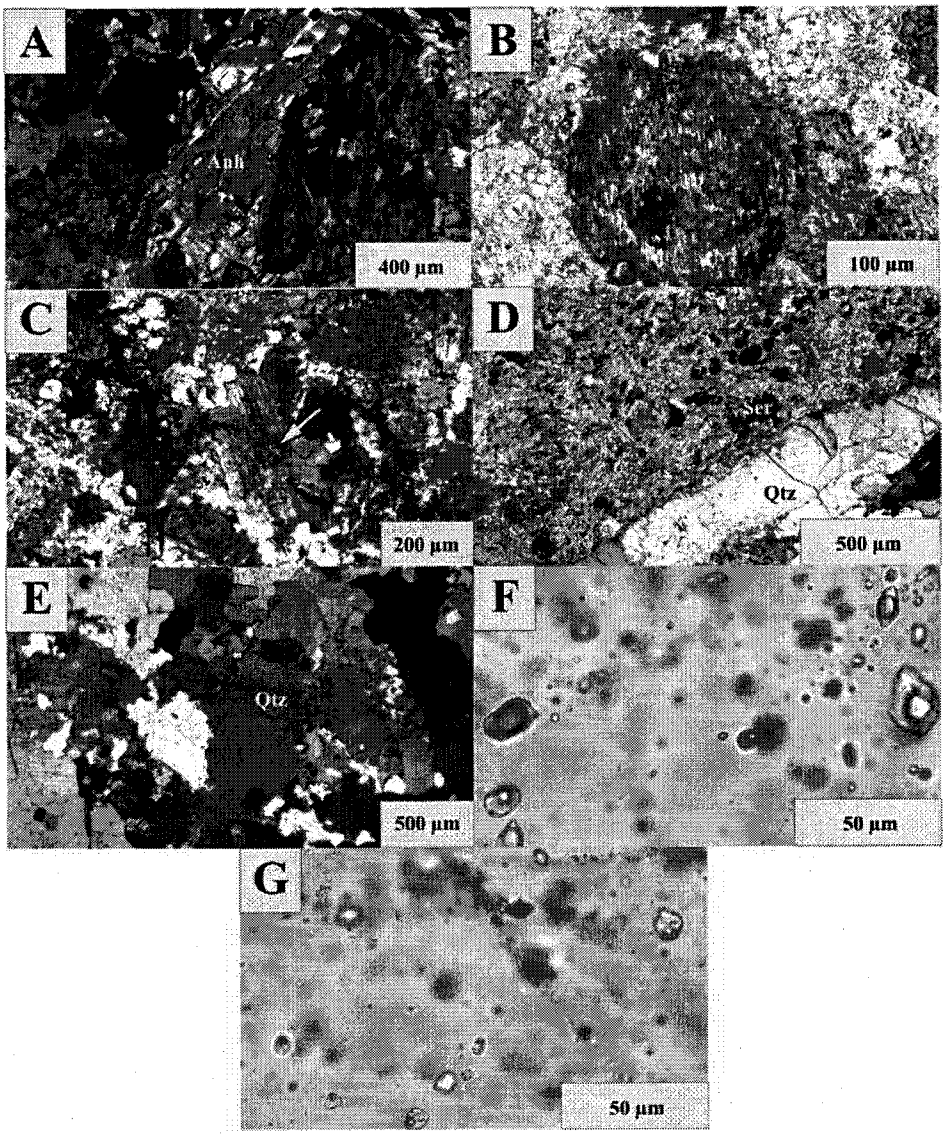

PLATE 7

7.A: Intense sericite, quartz, and clay overprint of the host monzonite along with disseminated pyrite (plane-polarized light; D415.3050).

7.B: Vein quartz displays both remnant comb and microcrystalline mosaic textures (crossed-polarized light; D415.3050).

7.C: Vein quartz displays both remnant comb texture (crossed-polarized light; D415.3050).

7.D: Quartz - pyrite vein has re-used the original vein channel (crossed-polarized light; D415.3050).

7.E: Intracrystalline intermediate density inclusions with rounded subhedral negative crystal shape (plane-polarized light; D415.3050).

7.F: Intracrystalline intermediate density inclusions with rounded subhedral negative crystal shape. Some inclusion trails follow healed fractures (plane-polarized light; D415.3050).

PLATE 7

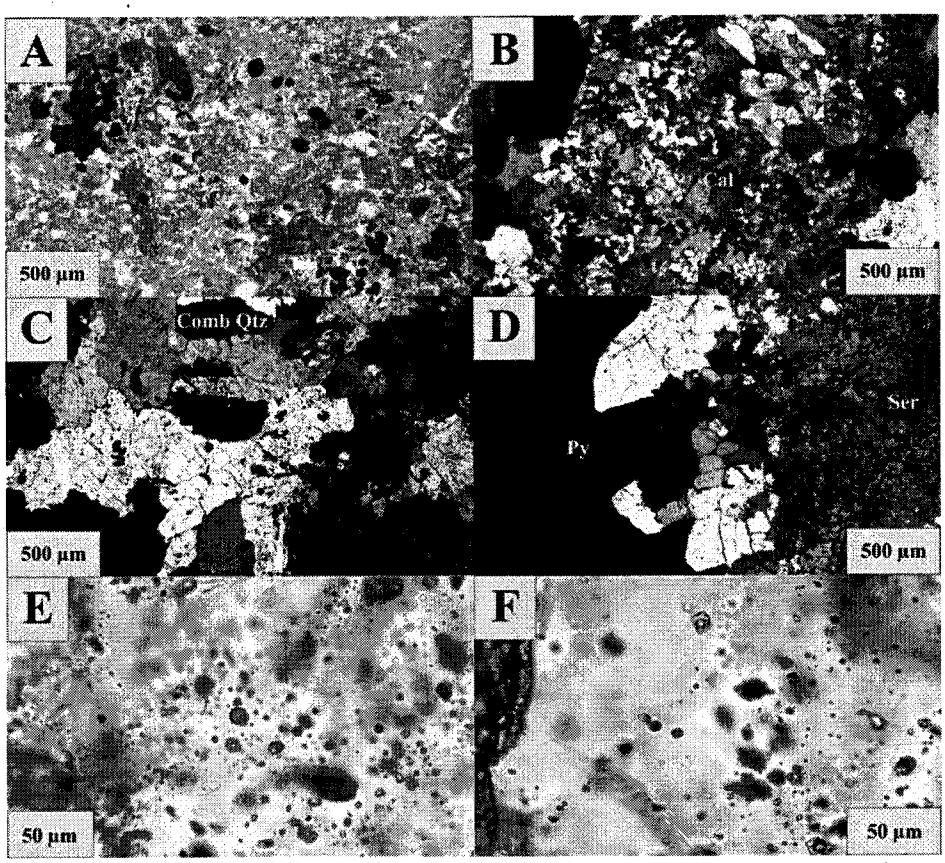

PLATE 8

8.A: Vein quartz displays a crustiform pattern alternating from microcrystalline mosaic texture to comb quartz with sutured grain boundaries (crossed-polarized light; D420.4710).

8.B: Vein quartz displays microcrystalline mosaic texture (crossed-polarized light; D420.4710).

8.C: Intracrystalline intermediate density inclusions with subhedral negative crystal shape. Some inclusions have the shape of a lemon due to necking (plane-polarized light; D420.4710).

8.D: Intracrystalline intermediate density inclusions with subhedral negative crystal shape. Some inclusions have the shape of a lemon due to necking. Secondary inclusion trails are also visible (plane-polarized light; D420.4710).

8.E: The host monzonite is pervasively altered to secondary hydrothermal alkali-feldspar occurring as anhedral patch perthites (crossed-polarized light; D420.5079.5).

8.F: Flaky zeolite veinlet with minor bornite (plane-polarized light; D420.5079.5).

8.G: Vein quartz displays a crustiform pattern alternating from a microcrystalline mosaic texture at the margins, to comb texture, then back to fine-grained mosaic texture at the pyrite centerline contact (crossed-polarized light; D420.5079.5).

8.H: Angular pyrite centerline that is rimmed by zeolite, amphibole, and sericite (plane-polarized light; D420.5079.5).

8.I: Intracrystalline intermediate density inclusions with euhedral to subhedral negative crystal shape. Some inclusions have the shape of a lemon due to necking (plane-polarized light; D420.5079.5).

PLATE 8

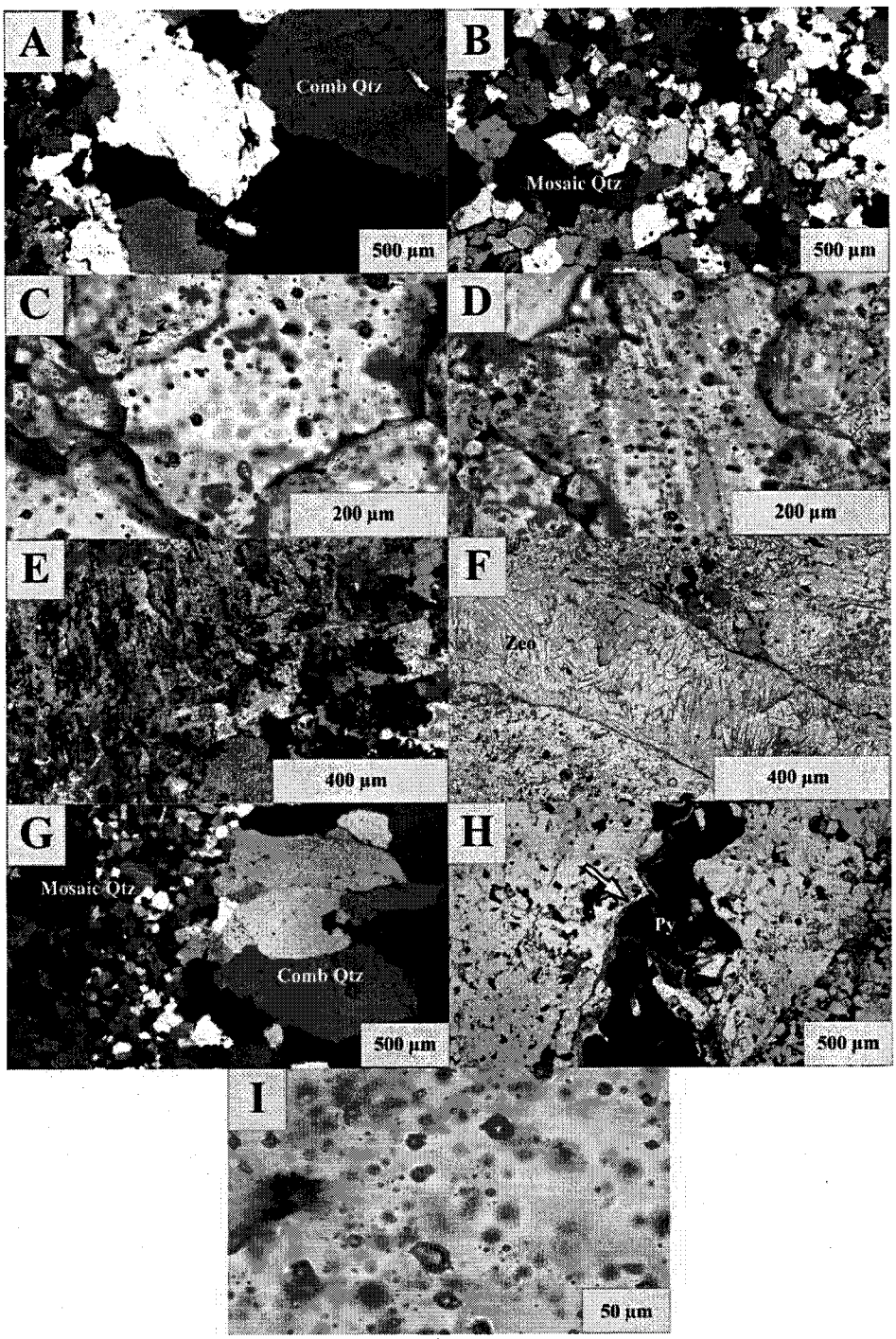

PLATE 9

9.A: Vein quartz displays a complex crustiform pattern, alternating between sets of microcrystalline and comb texture layers (crossed-polarized light; D430.3639).

9.B: Vein quartz displays a complex crustiform pattern, alternating between sets of microcrystalline and comb texture layers. Calcite and anhydrite grains also present (crossed-polarized light; D430.3639).

9.C: Vein quartz displays a complex crustiform pattern, alternating between sets of microcrystalline and comb texture layers (crossed-polarized light; D430.3768).

9.D: Intracrystalline intermediate density inclusions with euhedral to rounded subhedral negative crystal shape (plane-polarized light; D430.3768).

9.E: Intracrystalline intermediate density inclusions and irregular brines inclusions. Intermediate density inclusions display euhedral to rounded subhedral negative crystal shape (plane-polarized light; D430.3768).

PLATE 9

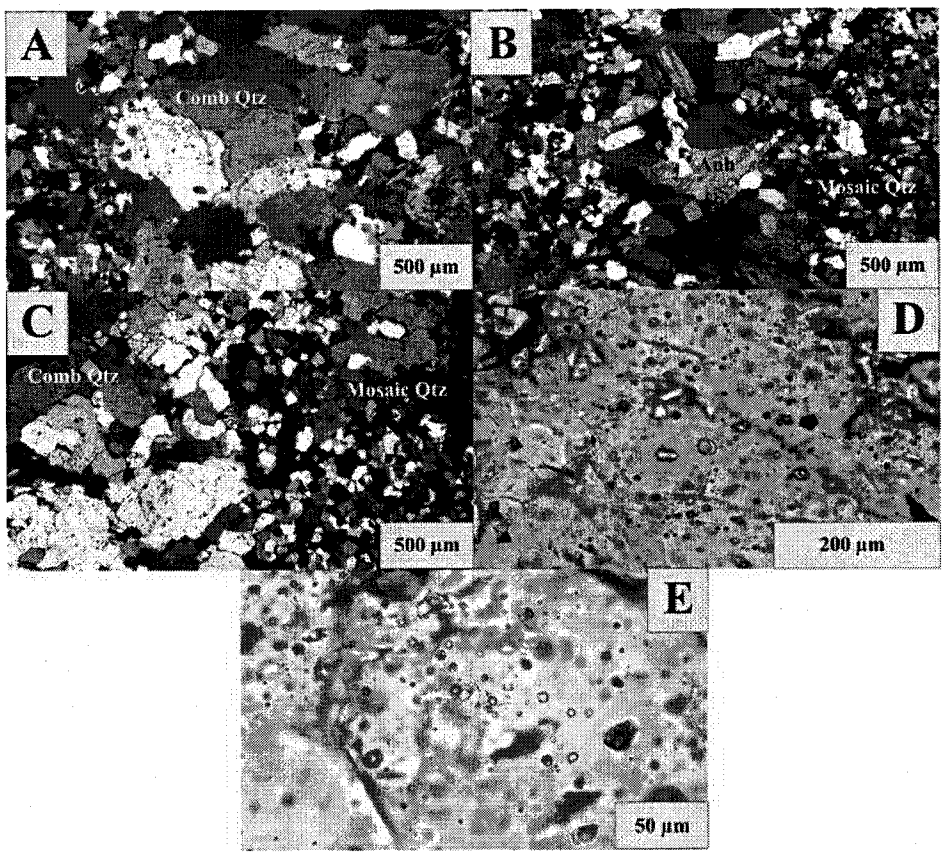

PLATE 10

10.A: Magmatic phlogopite is altered to clay minerals, appears to be sheared, and is associated with rutile (plane-polarized light; D152.2655).

10.B: Hydrothermal biotite is altered to sericite and clay minerals (plane-polarized light; D152.2655).

10.C: Vein quartz displays a mosaic texture with sutured grain boundaries (crossed-polarized light; D152.2655).

10.D: Vein quartz appears to have been overprinted by a linear flow of fluid that is visible as multiple sub-parallel trails of secondary fluid inclusions that cut across grain boundaries (crossed-polarized light; D152.2655).

10.E: Intracrystalline brine and polyphase brine inclusions displaying both subhedral negative crystal and irregular shapes (plane-polarized light; D152.2655).

10.F: Intracrystalline intermediate inclusions displaying euhedral to rounded subhedral negative crystal shape (plane-polarized light; D152.2655).

10.G: Multiple secondary fluid inclusion trails that cut across grain boundaries of vein quartz (plane-polarized light; D152.2655).

PLATE 10

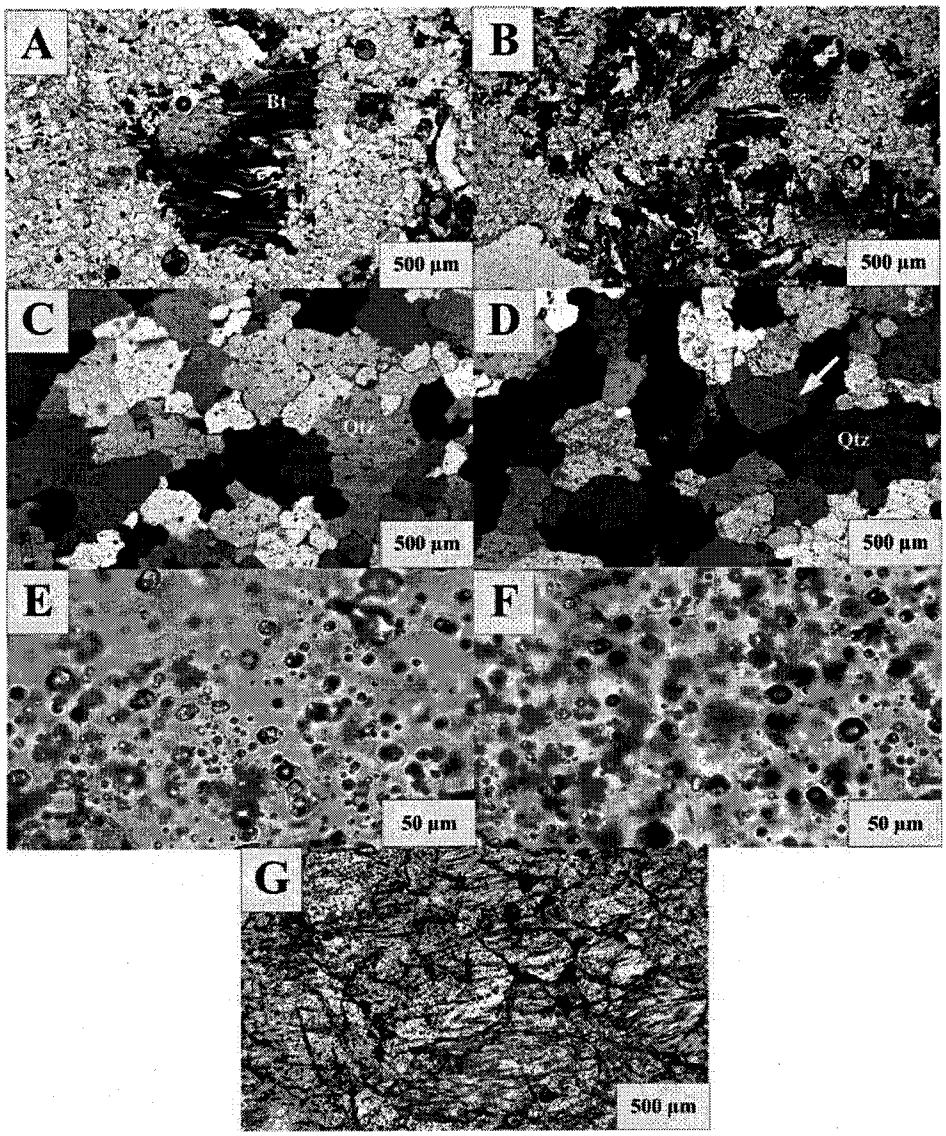

PLATE 11

11.A: Vein quartz displays comb texture with sutured grain boundaries. Larger prismatic crystals display strong undulatory extinction (crossed-polarized light; D162.2991).

11.B: Vein quartz displays comb texture with sutured grain boundaries. Larger prismatic crystals display strong undulatory extinction (crossed-polarized light; D162.2991).

11.C: Secondary hydrothermal biotite is pale yellow-brown in color, and is found as interlocking shreddy aggregates (plane-polarized light; D162.3367).

11.D: Secondary hydrothermal biotite is pale yellow-brown in color, and is found as interlocking shreddy aggregates (crossed-polarized light; D162.3367).

11.E: Deuteric amphibole is pale green-brown and pleochroic, and forms pseudomorphs after augite (plane-polarized light; D162.3367).

11.F: Deuteric amphibole is pale green-brown and pleochroic, and forms pseudomorphs after augite (crossed-polarized light; D162.3367).

11.G: Quartz - zeolite veinlet with biotite - alkali-feldspar selvage (plane-polarized light; D162.3367).

11.H: Vein quartz displays a mosaic texture with sutured grain boundaries (crossed-polarized light; D162.3367).

11.I: Intracrystalline intermediate inclusions displaying euhedral negative crystal shape (plane-polarized light; D162.3367).

11.J: Intracrystalline intermediate inclusions displaying euhedral to subhedral negative crystal shape (plane-polarized light; D162.3367).

PLATE 11

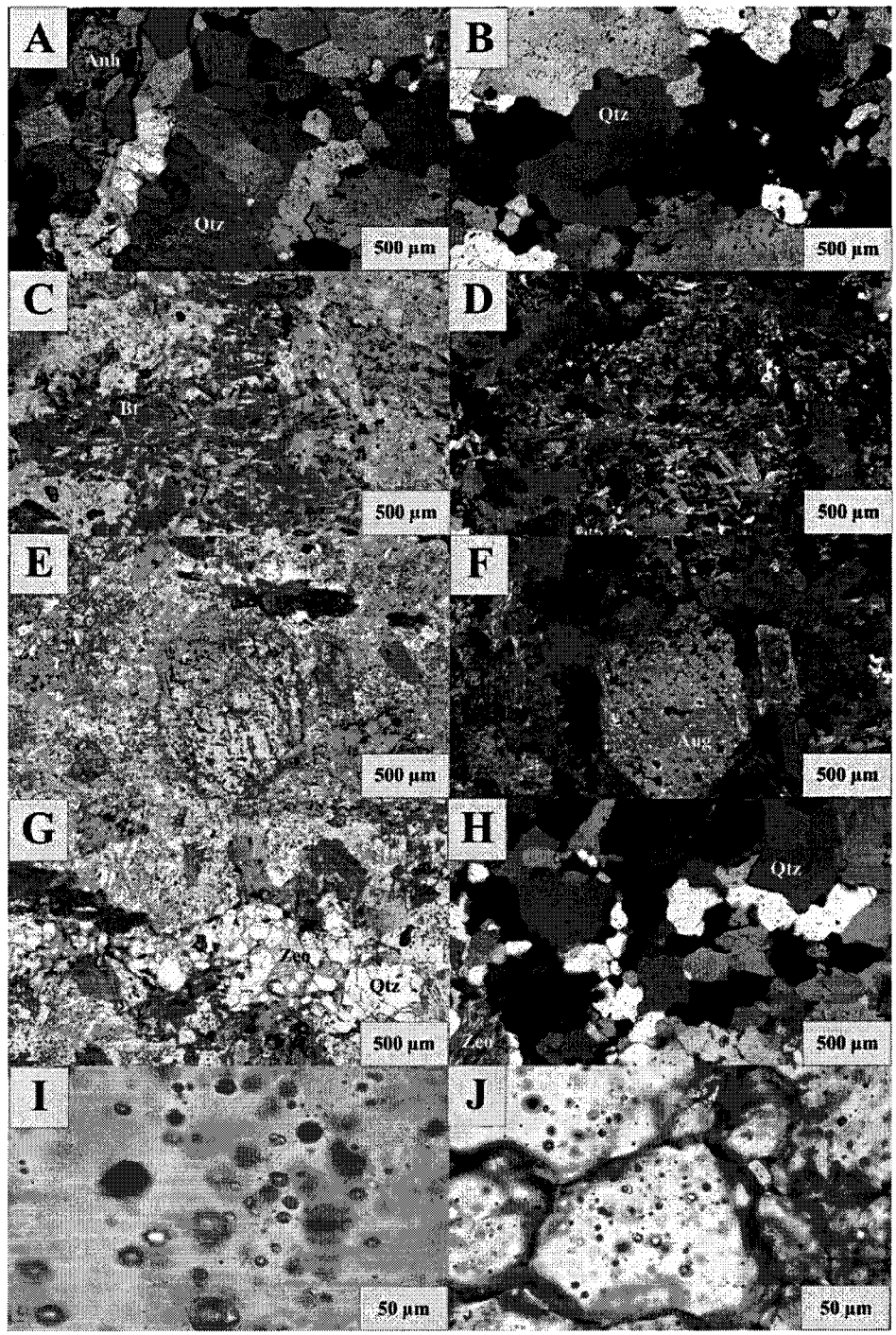

APPENDIX C
MICROTHERMOMETRY

This section contains the complete microthermometric data set for fluid inclusion assemblages from Butte, Montana, U.S.A and Bingham Canyon, Utah, U.S.A.

Table C-1: Microthermometric data for Butte, Montana, U.S.A and Bingham Canyon, Utah, U.S.A fluid inclusion assemblages.

Sample	Chip	Cluster	Inclusion	Type	Tm_{NaCl}	Tm_{ice}	Tm_{clath}	$Th_{l\text{-}v(l)}$	Th_{crit}	$Th_{l\text{-}v(v)}$	wt.% NaCl
11172-3740	1	A	1	B35	-	-2.3	-	332	-	-	3.87
			2	B35	-	-2.1	-	330	-	-	3.55
			3	B35	-	-2.9	-	328	-	-	4.80
			4	B35	-	-2.8	-	338	-	-	4.65
			5	B35	-	-2.3	-	332	-	-	3.87
			6	B35	-	-2.4	-	-	-	-	4.03
			7	B35	-	-3.1	-	337	-	-	5.11
			8	B35	-	-	-	331	-	-	-
			9	B35	-	-2.4	-	332	-	-	4.03
			10	B35	-	-2.7	-	-	-	-	4.49
			11	B35	-	-2.5	-	331	-	-	4.18
			12	B35	-	-2.5	-	342	-	-	4.18
			13	B35	-	-3.3	-	-	-	-	5.41
			14	B35	-	-3.2	-	333	-	-	5.26
			15	B35	-	-	-	333	-	-	-
			16	B35	-	-	-	330	-	-	-
			17	B35	-	-	-	333	-	-	-
			18	B35	-	-2.8	-	330	-	-	4.65
11172-1871	1	A	1	B35	-	-3.8	-	344	-	-	6.16
			2	B35	-	-3.6	-	343	-	-	5.86
			3	B35	-	-	-	343	-	-	-
			4	B35	-	-3.4	-	344	-	-	5.56
			5	B35	-	-	-	345	-	-	-
			6	B35	-	-4.2	-	340	-	-	6.74
			7	B35	-	-4.1	-	351	-	-	6.59
			8	B35	-	-2.8	-	339	-	-	4.65
			9	B35	-	-	-	346	-	-	-
			10	B35	-	-	-	344	-	-	-
			11	B35	-	-3.1	-	334	-	-	5.11
			12	B35	-	-3.2	-	352	-	-	5.26
			13	B35	-	-	-	348	-	-	-
			14	B35	-	-	-	350	-	-	-
			15	B35	-	-	-	352	-	-	-
			16	B35	-	-	-	348	-	-	-
			17	B35	-	-	-	341	-	-	-
			18	B35	-	-	-	340	-	-	-

Table C-1: Microthermometric data for Butte, Montana, U.S.A and Bingham Canyon, Utah, US.A fluid inclusion assemblages (continued).

Sample	Chip	Cluster	Inclusion	Type	Tm_{NaCl}	Tm_{ice}	Tm_{clath}	$Th_{l\text{-}v(l)}$	Th_{crit}	$Th_{l\text{-}v(v)}$	wt.% NaCl
11135-4967	1	A	1	B60	-	-	7.1	367	-	-	5.51
			2	B60	-	-	6.3	-	381	-	6.87
			3	B60	-	-	6.9	-	389	-	5.85
			4	B60	-	-	7.7	-	382	-	4.44
			5	B60	-	-	7.2	-	-	-	5.33
			6	B60	-	-	7.2	373	-	-	5.33
			7	B60	-	-	-	378	-	-	-
			8	B60	-	-	-	372	-	-	-
			9	B60	-	-	7.4	-	-	-	4.98
			10	B60	-	-	-	361	-	-	-
			11	B60	-	-	-	358	-	-	-
			12	B60	-	-	-	362	-	-	-
			13	B60	-	-	-	365	-	-	-
			14	B60	-	-	7.1	362	-	-	5.51
			15	B60	-	-	6.9	-	-	-	5.85
			16	B60	-	-	6.8	372	-	-	6.02
			17	B60	-	-	-	364	-	-	-
			18	B60	-	-	-	-	375	-	-
11052-7025	1	A	1	B60	-	-	-	-	390	-	-
			2	B60	-	-	-	-	385	-	-
			3	B60	-	-	-	-	376	-	-
			4	B60	-	-	-	-	381	-	-
			5	B60	-	-	-	-	383	-	-
			6	B60	-	-	-	-	374	-	-
			7	B60	-	-	-	-	388	-	-
	1	B	1	B60	-	-2.9	-	-	380	-	4.80
			2	B60	-	-	-	-	379	-	-
			3	B60	-	-2.8	-	-	378	-	4.65
			4	B60	-	-3.5	-	-	373	-	5.71
			5	B60	-	-3.1	-	-	379	-	5.11
			6	B60	-	-	-	-	374	-	-
			7	B60	-	-	-	-	377	-	-
			8	B60	-	-3.4	-	-	378	-	5.56
			9	B60	-	-	-	-	374	-	-
			10	B60	-	-3.3	-	-	375	-	5.41
11052-6215	1	A	1	B60	-	-	6.8	-	-	-	6.02
			2	B60	-	-	6.6	-	361	-	6.37
			3	B60	-	-	7.2	-	360	-	5.33
			4	B60	-	-	-	-	361	-	-
			5	B60	-	-	-	-	368	-	-
			6	B60	-	-	7.7	-	362	-	4.44
			7	B60	-	-	-	-	364	-	-
			8	B60	-	-	-	-	372	-	-
			9	B60	-	-	-	-	366	-	-
			10	B60	-	-	6.2	-	-	-	7.04
			11	B60	-	-	-	-	363	-	-
			12	B60	-	-	7.3	-	374	-	5.16
			13	B60	-	-	7.6	-	378	-	4.62
			14	B60	-	-	5.8	-	-	-	7.69
			15	B60	-	-	7.4	-	-	-	4.98

Table C-1: Microthermometric data for Butte, Montana, U.S.A and Bingham Canyon, Utah, U.S.A fluid inclusion assemblages (continued).

Sample	Chip	Cluster	Inclusion	Type	Tm_{NaCl}	Tm_{ice}	Tm_{clath}	$Th_{l\text{-}v(l)}$	Th_{crit}	$Th_{l\text{-}v(v)}$	wt.% NaCl
CZ1	1	A	1	$B20_{(MS)}$	-	-	-	308	-	-	-
			2	$B20_{(MS)}$	-	-	-	308	-	-	-
			3	$B20_{(MS)}$	-	-	-	278	-	-	-
			4	$B20_{(MS)}$	-	-2.4	-	295	-	-	4.03
			5	$B20_{(MS)}$	-	-4.1	-	267	-	-	6.59
			6	$B20_{(MS)}$	-	-1.9	-	290	-	-	3.23
			7	$B20_{(MS)}$	-	-2.2	-	291	-	-	3.71
			8	$B20_{(MS)}$	-	-	-	339	-	-	-
			9	$B20_{(MS)}$	-	-2.7	-	286	-	-	4.49
			10	$B20_{(MS)}$	-	-	-	346	-	-	-
			11	$B20_{(MS)}$	-	-	-	344	-	-	-
			12	$B20_{(MS)}$	-	-	-	311	-	-	-
			13	$B20_{(MS)}$	-	-	-	345	-	-	-
	1	B	1	$B20_{(MS)}$	-	-3.4	-	282	-	-	5.56
			2	$B20_{(MS)}$	-	-3.3	-	276	-	-	5.41
			3	$B20_{(MS)}$	-	-2.1	-	304	-	-	3.55
			4	$B20_{(MS)}$	-	-2.9	-	307	-	-	4.80
			5	$B20_{(MS)}$	-	-	-	348	-	-	-
			7	$B20_{(MS)}$	-	-	-	319	-	-	-
			8	$B20_{(MS)}$	-	-0.2	-	287	-	-	0.35
AL2	1	A	1	$B20_{(MS)}$	-	-	-	265	-	-	-
			2	$B20_{(MS)}$	-	-	-	246	-	-	-
			3	$B20_{(MS)}$	-	-	-	268	-	-	-
			4	$B20_{(MS)}$	-	-	-	256	-	-	-
			5	$B20_{(MS)}$	-	-	-	247	-	-	-
			6	$B20_{(MS)}$	-	-	-	246	-	-	-
			7	$B20_{(MS)}$	-	-	-	247	-	-	-
			8	$B20_{(MS)}$	-	-	-	225	-	-	-
			9	$B20_{(MS)}$	-	-	-	250	-	-	-
			10	$B20_{(MS)}$	-	-	-	251	-	-	-
			11	$B20_{(MS)}$	-	-	-	227	-	-	-
			12	$B20_{(MS)}$	-	-	-	249	-	-	-
			13	$B20_{(MS)}$	-	-	-	245	-	-	-
			14	$B20_{(MS)}$	-	-	-	288	-	-	-
	2	A	1	$B20_{(MS)}$	-	-0.8	-	-	-	-	1.40
			2	$B20_{(MS)}$	-	-1.2	-	-	-	-	2.07
			3	$B20_{(MS)}$	-	-2.2	-	-	-	-	3.71
			4	$B20_{(MS)}$	-	-1.9	-	-	-	-	3.23
			5	$B20_{(MS)}$	-	-1.9	-	-	-	-	3.23
			6	$B20_{(MS)}$	-	-1.4	-	-	-	-	2.41
			7	$B20_{(MS)}$	-	-1.7	-	-	-	-	2.90
			8	$B20_{(MS)}$	-	-0.8	-	-	-	-	1.40
			9	$B20_{(MS)}$	-	-0.3	-	-	-	-	0.53
			10	$B20_{(MS)}$	-	-0.9	-	-	-	-	1.57

Table C-1: Microthermometric data for Butte, Montana, U.S.A and Bingham Canyon, Utah, U.S.A fluid inclusion assemblages (continued).

Sample	Chip	Cluster	Inclusion	Type	Tm_{NaCl}	Tm_{ice}	Tm_{clath}	$Th_{l-v(l)}$	Th_{crit}	$Th_{l-v(v)}$	wt.% NaCl
X3564	1	A	1	$B20_{(MS)}$	-	-	-	208	-	-	-
			2	$B20_{(MS)}$	-	-	-	227	-	-	-
			3	$B20_{(MS)}$	-	-	-	222	-	-	-
			4	$B20_{(MS)}$	-	-	-	244	-	-	-
			5	$B20_{(MS)}$	-	-	-	204	-	-	-
			6	$B20_{(MS)}$	-	-	-	227	-	-	-
			7	$B20_{(MS)}$	-	-	-	196	-	-	-
			8	$B20_{(MS)}$	-	-	-	212	-	-	-
			9	$B20_{(MS)}$	-	-	-	222	-	-	-
			10	$B20_{(MS)}$	-	-	-	214	-	-	-
			11	$B20_{(MS)}$	-	-	-	230	-	-	-
	2	A	1	$B20_{(MS)}$	-	-	-	216	-	-	-
			2	$B20_{(MS)}$	-	-	-	219	-	-	-
			3	$B20_{(MS)}$	-	-	-	217	-	-	-
			4	$B20_{(MS)}$	-	-	-	221	-	-	-
			5	$B20_{(MS)}$	-	-1.0	-	217	-	-	1.74
			6	$B20_{(MS)}$	-	-1.0	-	226	-	-	1.74
			7	$B20_{(MS)}$	-	-0.9	-	218	-	-	1.57
			8	$B20_{(MS)}$	-	-1.1	-	229	-	-	1.91
			9	$B20_{(MS)}$	-	-1.4	-	230	-	-	2.41
			10	$B20_{(MS)}$	-	-1.0	-	225	-	-	1.74
			11	$B20_{(MS)}$	-	-	-	229	-	-	-
			12	$B20_{(MS)}$	-	-0.9	-	233	-	-	1.57
			13	$B20_{(MS)}$	-	-1.1	-	217	-	-	1.91
			14	$B20_{(MS)}$	-	-1.2	-	218	-	-	2.07
			15	$B20_{(MS)}$	-	-	-	227	-	-	-
			16	$B20_{(MS)}$	-	-1.0	-	229	-	-	1.74
			17	$B20_{(MS)}$	-	-1.1	-	233	-	-	1.91
Modoc-10649	1	A	1	B20	-	-	-	298	-	-	-
			2	B20	-	-	-	296	-	-	-
			3	B20	-	-3.2	-	299	-	-	5.26
			4	B20	-	-2.9	-	301	-	-	4.80
			5	B20	-	-2.8	-	289	-	-	4.65
			6	B20	-	-3.0	-	266	-	-	4.96
			7	B20	-	-	-	302	-	-	-
			8	B20	-	-3.1	-	288	-	-	5.11
			9	B20	-	-3.4	-	287	-	-	5.56
			10	B20	-	-3.5	-	295	-	-	5.71
			11	B20	-	-	-	293	-	-	-
			12	B20	-	-	-	286	-	-	-

Table C-1: Microthermometric data for Butte, Montana, U.S.A and Bingham Canyon, Utah, U.S.A fluid inclusion assemblages (continued).

Sample	Chip	Cluster	Inclusion	Type	Tm_{NaCl}	Tm_{ice}	Tm_{clath}	$Th_{l\text{-}v(l)}$	Th_{crit}	$Th_{l\text{-}v(v)}$	wt.% NaCl
Modoc-10649	1	A	13	B20	-	-	-	304	-	-	-
			14	B20	-	-	-	303	-	-	-
			15	B20	-	-	-	305	-	-	-
			16	B20	-	-	-	284	-	-	-
			17	B20	-	-	-	276	-	-	-
			18	B20	-	-	-	274	-	-	-
			19	B20	-	-	-	276	-	-	-
			20	B20	-	-	-	316	-	-	-
			21	B20	-	-3.0	-	291	-	-	4.96
			22	B20	-	-3.2	-	287	-	-	5.26
			23	B20	-	-3.1	-	271	-	-	5.11
			24	B60	-	-	8.5	366	-	-	2.97
			25	B60	-	-	8.8	376	-	-	2.39
			26	B20	-	-3.3	-	302	-	-	5.41
			27	B20	-	-2.7	-	290	-	-	4.49
			28	B20	-	-	-	291	-	-	-
			29	B60	-	-	-	342	-	-	-
			30	B20	-	-3.2	-	-	-	-	5.26
			31	B20	-	-2.6	-	-	-	-	4.34
D415.2936	1	A	1	ID	-	-	6.7	-	412	-	6.20
			2	ID	-	-	5.7	-	409	-	7.85
			3	ID	-	-	6.7	-	430	-	6.20
			4	ID	-	-	-	-	-	466	-
			7	ID	-	-	8.3	-	367	-	3.34
			8	ID	-	-	6.5	-	-	-	-
			9	ID	-	-	9.1	-	365	-	1.81
			10	ID	-	-	-	-	378	-	-
			11	ID	-	-	-	-	461	-	-
	1	B	1	B	-	-	-	350	-	-	-
			2	B	-	-	-	345	-	-	-
			3	B	-	-	-	332	-	-	-
			4	B	-	-	-	368	-	-	-
			5	B	-	-	-	317	-	-	-
			6	B	-	-	-	301	-	-	-
			7	B	-	-	-	317	-	-	-
			8	B	-	-	-	336	-	-	-
	2	A	1	ID	-	-	-	-	411	-	-
			2	ID	-	-	-	-	412	-	-
			3	ID	-	-	-	-	414	-	-
			4	ID	-	-	-	-	371	-	-
			5	ID	-	-	-	-	362	-	-
			6	ID	-	-	-	-	359	-	-
			7	ID	-	-	-	-	354	-	-
			8	ID	-	-	-	-	364	-	-
			9	ID	-	-	-	-	363	-	-

Table C-1: Microthermometric data for Butte, Montana, U.S.A and Bingham Canyon, Utah, U.S.A fluid inclusion assemblages (continued).

Sample	Chip	Cluster	Inclusion	Type	Tm_{NaCl}	Tm_{ice}	Tm_{clath}	$Th_{l\text{-}v(l)}$	Th_{crit}	$Th_{l\text{-}v(v)}$	wt.% NaCl
D415.2982.5	1	A	1	B	258	-	-	277	-	-	35.2
			2	B	260	-	-	271	-	-	35.3
			3	B	275	-	-	308	-	-	36.3
			4	B	-	-	-	292	-	-	-
			5	B	-	-	-	271	-	-	-
			6	B	-	-	-	325	-	-	-
			7	B	-	-	-	290	-	-	-
			8	B	-	-	-	224	-	-	-
			9	B	-	-	-	243	-	-	-
			10	B	-	-	-	224	-	-	-
			11	B	-	-	-	235	-	-	-
			12	B	-	-	-	243	-	-	-
			13	B	263	-	-	276	-	-	35.5
	1	B	1	B	-	-	-	311	-	-	-
			2	B	-	-	-	319	-	-	-
			3	B	-	-	-	318	-	-	-
			4	B	-	-	-	301	-	-	-
			5	B	-	-	-	307	-	-	-
			6	B	-	-	-	325	-	-	-
			7	B	-	-	-	319	-	-	-
			8	B	-	-	-	307	-	-	-
			9	B	-	-	-	318	-	-	-
			10	B	-	-	-	313	-	-	-
			11	B	-	-	-	325	-	-	-
			12	B	-	-	-	313	-	-	-
			13	B	-	-	-	319	-	-	-
			14	B	-	-	-	312	-	-	-
			15	B	-	-	-	329	-	-	-
	1	C	1	ID	-	-	-	-	377	-	-
			2	ID	-	-	-	-	377	-	-
			3	ID	-	-	-	-	381	-	-
			4	ID	-	-	-	-	383	-	-
			5	ID	-	-	-	-	379	-	-
			6	ID	-	-	-	-	393	-	-
			7	ID	-	-	-	-	389	-	-
			8	ID	-	-	-	-	391	-	-
			9	ID	-	-	-	-	375	-	-
			10	ID	-	-	-	-	377	-	-

Table C-1: Microthermometric data for Butte, Montana, U.S.A and Bingham Canyon, Utah, U.S.A fluid inclusion assemblages (continued).

Sample	Chip	Cluster	Inclusion	Type	Tm_{NaCl}	Tm_{ice}	Tm_{clath}	$Th_{l\text{-}v(l)}$	Th_{crit}	$Th_{l\text{-}v(v)}$	wt.% NaCl
D415.3025	1	A	1	ID	-	-	7.3	-	379		5.16
			2	ID	-	-	7.4	-	-	374	4.98
			3	ID	-	-	7.8	-	378		4.26
			4	ID	-	-	7.2		380		5.33
			5	ID	-	-	-	-	378		-
			6	ID	-	-	7.1	-	374		5.51
			7	ID	-	-	7.8	-	379		4.26
			8	ID	-	-	7.8	-	384		4.26
			9	ID	-	-	8.2	-	-	379	3.53
			10	ID	-	-	7.4	-	-	392	4.98
			11	ID	-	-	7.3	-	-	-	5.16
			12	ID	-	-	7.9	-	-	384	4.08
			13	ID	-	-	-	-	375	-	-
			14	ID	-	-	-	-	-	392	-
D415.3050	1	A	1	ID	-	-	7.4	-	367	-	4.98
			2	ID	-	-	-	-	-	368	-
			3	ID	-	-	-	-	367	-	-
			4	ID	-	-	6.4	-	366	-	6.70
			5	ID	-	-	6.2	-	365	-	7.04
			6	ID	-	-	6.7	-	367	-	6.20
			7	ID	-	-	7.4	-	368	-	4.98
			8	ID	-	-	-	-	-	389	-
			9	ID	-	-	-	-	-	359	-
			10	ID	-	-	7.5	-	-	394	4.80
			11	ID	-	-	7.3	-	-	393	5.16
			12	ID	-	-	5.8	-	363	-	7.69
			13	ID	-	-	-	-	-	359	-
D420.4710	1	A	1	ID	-	-	-	-	361	-	-
			2	ID	-	-	-	-	359	-	-
			3	ID	-	-	-	-	366	-	-
			4	ID	-	-	-	-	366	-	-
			5	ID	-	-	-	-	368	-	-
			6	ID	-	-	-	-	370	-	-
			7	ID	-	-	-	-	360	-	-
			8	ID	-	-	-	-	371	-	-
	1	B	1	ID	-	-	-	-	369	-	-
			2	ID	-	-	-	-	358	-	-
			3	ID	-	-	-	-	361	-	-
			4	ID	-	-	-	-	360	-	-

Table C-1: Microthermometric data for Butte, Montana, U.S.A and Bingham Canyon, Utah, U.S.A fluid inclusion assemblages (continued).

Sample	Chip	Cluster	Inclusion	Type	Tm_{NaCl}	Tm_{ice}	Tm_{clath}	$Th_{l\text{-}v(l)}$	Th_{crit}	$Th_{l\text{-}v(v)}$	wt.% NaCl
D420.4710	1	C	1	ID	-	-	-	-	391	-	-
			2	ID	-	-	-	-	371	-	-
			3	ID	-	-	-	-	381	-	-
			4	ID	-	-	-	-	368	-	-
			5	ID	-	-	-	-	370	-	-
			6	ID	-	-	-	-	366	-	-
			7	ID	-	-	-	-	367	-	-
			8	ID	-	-	-	-	367	-	-
			9	ID	-	-	-	-	363	-	-
	2	A	1	ID	-	-	7.9	-	-	-	4.08
			2	ID	-	-	8.1	-	-	-	3.71
			3	ID	-	-	8.3	-	-	-	3.34
			4	ID	-	-	7.8	-	-	-	4.26
			5	ID	-	-	8.4	-	365	-	3.15
			6	ID	-	-	8.8	-	371	-	2.39
			7	ID	-	-	-	-	368	-	-
			8	ID	-	-	-	-	365	-	-
			9	ID	-	-	8.9	-	374	-	2.20
			10	ID	-	-	9.0	-	374	-	2.01
			11	ID	-	-	-	-	366	-	-
			12	ID	-	-	-	-	366	-	-
			13	ID	-	-	-	-	370	-	-
			14	ID	-	-	8.2	-	374	-	3.53
			15	ID	-	-	-	-	365	-	-
			16	ID	-	-	-	-	366	-	-
			17	ID	-	-	8.1	-	-	-	3.71
			18	ID	-	-	8.2	-	-	-	3.53
D420.5079.5	1	A	1	ID	-	-	-	-	374	-	-
			2	ID	-	-	-	-	373	-	-
			3	ID	-	-	-	-	380	-	-
			4	ID	-	-	-	-	376	-	-
			5	ID	-	-	-	-	359	-	-
			6	ID	-	-	-	-	405	-	-
			7	ID	-	-	-	-	384	-	-
			8	ID	-	-	-	-	407	-	-
	1	B	1	ID	-	-	-	-	362	-	-
			2	ID	-	-	-	-	363	-	-
			3	ID	-	-	-	-	363	-	-
			4	ID	-	-	-	-	371	-	-

Table C-1: Microthermometric data for Butte, Montana, U.S.A and Bingham Canyon, Utah, U.S.A fluid inclusion assemblages (continued).

Sample	Chip	Cluster	Inclusion	Type	Tm_{NaCl}	Tm_{ice}	Tm_{clath}	$Th_{l\text{-}v(l)}$	Th_{crit}	$Th_{l\text{-}v(v)}$	wt.% NaCl
D420.5079.5	1	C	1	ID	-	-	-	-	354	-	-
			2	ID	-	-	-	-	356	-	-
			3	ID	-	-	-	-	368	-	-
			4	ID	-	-	-	-	351	-	-
			5	ID	-	-	-	-	354	-	-
	2	A	1	ID	-	-	8.5	-	371	-	2.97
			2	ID	-	-	9.4	-	359	-	1.22
			3	ID	-	-	7.8	-	360	-	4.26
			4	ID	-	-	7.2	-	362	-	5.33
			5	ID	-	-	7.4	-	361	-	4.98
			6	ID	-	-	7.2	-	366	-	5.33
			7	ID	-	-	-	-	367	-	-
			8	ID	-	-	7.4	-	362	-	4.98
			9	ID	-	-	8.6	-	365	-	2.78
			10	ID	-	-	-	-	353	-	-
			11	ID	-	-	-	-	362	-	-
			12	ID	-	-	-	-	358	-	-
			13	ID	-	-	9.2	-	367	-	1.62
			14	ID	-	-	-	-	357	-	-
			15	ID	-	-	-	-	361	-	-
D430.3639	1	A	1	ID	-	-	9.2	-		379	1.62
			2	ID	-	-	8.8	-		378	2.39
			3	ID	-	-	9.4	-		377	1.22
			4	ID	-	-	-	-		378	-
			5	ID	-	-	7.8	-		382	4.26
			6	ID	-	-	9.3	-		377	1.42
			7	ID	-	-	9.4	-		377	1.22
			8	ID	-	-	8.6	-		384	2.78
			9	ID	-	-	7.8	-		-	4.26
			10	ID	-	-	9.1	-		-	1.81
			11	ID	-	-	-	-	380	-	-
			12	ID	-	-	7.6	-	372	-	4.62
			13	ID	-	-	8.1	-	378	-	3.71
			14	ID	-	-	7.9	-	374	-	4.08
			15	ID	-	-	-	-	-	382	-
			16	ID	-	-	-	-	-	373	-
			17	ID	-	-	-	-	372	-	-
			18	ID	-	-	-	-	380	-	-
			19	ID	-	-	-	-	372	-	-
			20	ID	-	-	-	-	377	-	-
			21	ID	-	-	-	-	376	-	-

Table C-1: Microthermometric data for Butte, Montana, U.S.A and Bingham Canyon, Utah, U.S.A fluid inclusion assemblages (continued).

Sample	Chip	Cluster	Inclusion	Type	Tm_{NaCl}	Tm_{ice}	Tm_{clath}	$Th_{l\text{-}v(l)}$	Th_{crit}	$Th_{l\text{-}v(v)}$	wt.% NaCl
D430.3768	1	A	1	ID	-	-	6.5	-		386	6.53
			2	ID	-	-	6.9	-		393	5.85
			3	ID	-	-	-	-	422	-	-
			4	ID	-	-	7.4	-	436	-	4.98
			5	ID	-	-	7.1	-	387	-	5.51
			6	ID	-	-	6.9	-	-	383	5.85
			7	ID	-	-	6.9	-	-	392	5.85
			8	ID	-	-	7.3	-	-	386	5.16
			9	ID	-	-	6.8	-	-	397	6.02
			10	ID	-	-	7.2	-		377	5.33
			11	ID	-	-	6.6	-		389	6.37
			12	ID	-	-	6.9	-		-	5.85
			13	ID	-	-	7.0	-		-	5.68
	1	B	1	ID	-	-	6.4	-	375	-	6.70
			2	ID	-	-	-	-	378	-	-
			3	ID	-	-	-	-	-	-	-
			4	ID	-	-	5.8	-	-	-	7.69
			5	ID	-	-	-	-	-	398	-
			6	ID	-	-	5.6	-	-	435	8.01
			7	ID	-	-	-	-	459	-	-
			8	ID	-	-	-	-	-	-	-
			9	ID	-	-	-	-	-	-	-
			10	ID	-	-	-	-	-	-	-
			11	ID	-	-	7.1	-	-	-	5.51
D162.2991	1	A	1	ID	-	-	8.5	-	-	383	2.97
			2	ID	-	-1.4	-	-	363	-	2.41
			3	ID	-	-	6.2	-	393	-	7.04
			4	ID	-	-2.1	-	-	395	-	3.55
			5	ID	-	-	7.8	-	-	378	4.26
			6	ID	-	-	-	-	-	394	-
			7	ID	-	-	-	-	414	-	-
			8	ID	-	-	-	-	-	393	-
			9	ID	-	-	-	-	-	387	-
	1	B	1	ID	-	-	3.3	-	-	449	11.4
			2	ID	-	-	-	-	475	-	-
			3	ID	-	-	2.4	-	-	397	12.7
			4	ID	-	-	-	-	417	-	-
			5	ID	-	-	-	-	-	465	-
			6	ID	-	-	-	-	-	-	-
			7	ID	-	-	-	-	474	-	-
			8	ID	-	-	-	-	407	-	-
			9	ID	-	-	5.1	-	-	443	8.80
			10	ID	-	-	3.1	-	-	-	11.7

Table C-1: Microthermometric data for Butte, Montana, U.S.A and Bingham Canyon, Utah, U.S.A fluid inclusion assemblages (continued).

Sample	Chip	Cluster	Inclusion	Type	Tm_{NaCl}	Tm_{ice}	Tm_{clath}	$Th_{l\text{-}v(l)}$	Th_{crit}	$Th_{l\text{-}v(v)}$	wt.% NaCl
D162.2991	1	B	11	ID	-	-	8.3	-	-	373	3.34
			12	ID	-	-	6.6	-	395	-	6.37
			13	ID	-	-	6.7	-	-	377	6.20
			14	ID	-	-	-	-	-	380	-
			15	ID	-	-	6.2	-	375	-	7.04
			16	ID	-	-	3.8	-	368	-	10.7
			17	ID	-	-	8.2	-	-	372	3.53
D162.3367	1	A	1	B	261	-	-	366	-	-	35.4
			2	B	249	-	-	342	-	-	34.6
			3	ID	-	-	-	-	455	-	-
			4	ID	-	-	-	-	438	-	-
			5	B	-	-	-	359	-	-	-
			6	ID	-	-	-	-	-	463	-
			7	ID	-	-	-	-	438	-	-
			8	B	-	-	-	362	-	-	-
			9	B	-	-	-	368	-	-	-
			10	B	251	-	-	348	-	-	34.7
			11	B	254	-	-	358	-	-	34.9
			12	B	262	-	-	365	-	-	35.5
	2	A	1	ID	-	-	6.8	-	-	389	6.02
			2	ID	-	-	7.2	-	-	396	5.33
			3	ID	-	-	6.9	-	-	383	5.85
			4	ID	-	-	6.6	-	-	461	6.37
			5	ID	-	-	-	-	-	460	-
			6	ID	-	-	-	-	-	394	-
			7	ID	-	-	-	-	-	395	-
			8	ID	-	-	-	-	-	396	-
			9	ID	-	-	-	-	-	463	-
			10	ID	-	-	-	-	-	456	-
			11	ID	-	-	7.1	-	-	461	5.51
			12	ID	-	-	7.4	-	-	406	4.98
			13	ID	-	-	-	-	-	398	-
D152.2655	1	A	1	B	233	-	-	308	-	-	33.7
			2	B	289	-	-	274	-	-	37.3
			3	B	231	-	-	312	-	-	33.5
			4	B	239	-	-	310	-	-	34.0
			5	B	302	-	-	290	-	-	38.3
			6	B	288	-	-	265	-	-	37.3
			7	B	306	-	-	285	-	-	38.6
			8	B	263	-	-	293	-	-	35.5

Table C-1: Microthermometric data for Butte, Montana, U.S.A and Bingham Canyon, Utah, U.S.A fluid inclusion assemblages (continued).

Sample	Chip	Cluster	Inclusion	Type	Tm_{NaCl}	Tm_{ice}	Tm_{clath}	$Th_{l\text{-}v(l)}$	Th_{crit}	$Th_{l\text{-}v(v)}$	wt.% NaCl
D152.2655	1	A	9	B	240	-	-	303	-	-	34.1
	1	B	1	B	268	-	-	378			35.9
			2	B	278	-	-	312			36.5
			3	B	273	-	-	341			36.2
			4	B	283	-	-	331			36.9
			5	B	296	-	-	318			37.9

APPENDIX D
ION CHROMATOGRAPHY

This section contains the ion chromatography data, quality analysis, and quality control. This section is divided into two sub-sections. Section **D1** contains the complete anion data set, and section **D2** contains the quality analysis and quality control calculations. The analytical techniques employed to determine the concentration of anions in fluid inclusion leachates are discussed in **Chapters 3** and **5**.

D1 Anion Data

Table D1-1: Anion data for Butte, Montana, U.S.A and Bingham Canyon, Utah, U.S.A.

Sample	crush (g)	water (ml)	F^- (ppm)	Cl^- (ppm)	NO_2^- (ppm)	Br^- (ppm)	NO_3^- (ppm)	PO_4^{-3} (ppm)	SO_4^{2-} (ppm)	Br/Cl ($X10^{-3}M$)
CZ1										
Crush 1	1.52	10	0.001	0.808	0.117	0.003	-	-	0.642	1.65
Crush 2	1.12	2	0.002	4.913	0.111	0.011	-	0.197	3.460	0.99
AL2										
Crush 1	1.52	10	0.016	1.183	0.093	0.005	-	-	0.515	1.88
Crush 2	0.20	2	0.040	2.534	0.227	-	-	-	1.630	-
X3564										
Crush1	1.59	10	0.033	0.960	0.078	0.003	-	0.048	0.530	1.39
Crush2	1.27	2	0.062	3.985	0.152	0.004	-	0.229	1.047	0.45
11172-3740										
Crush 1	1.53	10	-	1.562	0.082	0.003	-	-	82.700	0.85
Crush 2	1.00	2	0.004	9.611	0.172	0.009	-	3.953	32.133	0.42
11172-1871										
Crush 1	1.10	10	-	0.524	0.065	0.008	-	-	22.908	6.77
Duplicate	-	-	-	0.716	0.091	-	-	-	28.145	-
11052-7025										
Crush 1	1.67	10	-	4.916	0.091	0.009	-	-	2.120	0.81
Crush 2	2.24	5	-	12.675	0.043	-	-	-	4.109	-
11052-6215										
Crush 1	1.64	10	0.047	4.520	0.055	0.011	-	0.092	3.007	1.08
Crush 2	2.07	5	0.020	14.183	-	-	-	0.014	8.516	-
11135-4967										
Crush 1	1.69	10	-	2.946	0.084	0.004	-	-	0.885	0.60
Crush 2	2.31	5	-	7.358	0.127	-	-	0.006	2.253	-

Table D1-1: Anion data for Butte, Montana, U.S.A and Bingham Canyon, Utah, U.S.A (continued).

Sample	crush (g)	water (ml)	F^- (ppm)	Cl^- (ppm)	NO_2^- (ppm)	Br^- (ppm)	NO_3^- (ppm)	PO_4^{-3} (ppm)	SO_4^{2-} (ppm)	Br/Cl ($X10^{-3}M$)
Modoc-10649										
Crush 1	1.60	10	-	1.936	0.076	0.004	-	0.024	0.755	0.92
Crush 2	1.71	5	-	4.452	-	-	-	0.065	1.503	-
D415.2936										
Crush 1	1.74	10	-	5.604	0.068	-	-	-	19.327	-
Duplicate	-	-	-	7.358	0.085	0.003	0.404	-	24.815	0.18
D415.2982.5										
Crush 1	1.63	10	-	3.203	0.037	-	-	0.030	11.708	-
Crush 2	0.93	2	0.007	9.862	0.104	0.005	0.939	-	33.861	0.22
D415.3025										
Crush 1	0.99	10	0.019	2.526	0.084	0.005	-	-	7.884	0.88
Duplicate	-	-	0.012	3.368	0.113	-	0.737	0.006	9.926	-
D415.3050										
Crush 1	1.60	10	-	6.974	0.034	0.005	-	-	4.404	0.32
Crush 2	2.07	5	-	1.749	0.071	-	-	-	1.092	-
D420.4710										
Crush 1	1.57	10	0.225	11.791	0.295	0.067	-	5.252	15.900	2.52
Crush 2	2.07	5	-	1.749	0.071	-	-	-	1.092	-
D420.5079.5										
Crush 1	1.63	10	0.236	0.844	0.052	0.007	-	0.005	3.167	3.68
Crush 2	1.37	2	-	5.160	0.764	-	-	0.103	23.247	-
D430.3639										
Crush 1	1.49	10	0.006	1.511	0.059	-	-	0.006	1.953	-
Crush 2	0.83	2	-	4.303	-	0.004	0.914	-	5.074	0.41
D430.3768										
Crush 1	1.19	10	-	2.049	0.085	-	-	-	0.784	-
Duplicate	-	-	-	2.585	0.086	-	-	0.005	1.055	-
D152.2655										
Crush 1	1.63	10	-	58.217	-	0.084	-	-	4.129	0.64
D162.2991										
Crush 1	1.53	10	-	14.746	0.067	-	-	-	8.119	-
Crush 2	1.03	2	0.016	49.711	-	0.056	0.763	-	26.365	0.50
D162.3367										
Crush 1	1.10	10	-	2.441	0.059	0.006	-	-	-	1.09
Crush 2	-	-	-	3.021	0.045	-	-	-	5.656	-

D2 Data Analysis

This section is sub-divided into two sections: section **D2.1** contains accuracy calculations; section **D2.2** contains precision calculations.

D2.1 Accuracy

The accuracy of anion analyses performed by ion chromatography was calculated as the relative error between measurements of analytical standards measured as unknown solutions (Skoog et al., 1998):

Relative Error (%) = 100 * (measured value-accepted value) / (accepted value)

Relative error was calculated using a spreadsheet and is only presented for anions that were above detection limits.

Table D2.1-1: Accuracy of ion chromatography for determination of anion species calculated from replicate analyses of anion standards.

	Measured Value (ppm)		
Anion	**STD 2-A**	**STD 2-B**	**STD-3**
F^-	1.8017	1.7783	0.1116
	1.7271	-	-
Actual	1.6723	1.8898	0.1570
Average	1.7644	1.7783	0.1116
%error	**5.51**	**-5.90**	**28.92**
Cl^-	2.4951	2.3287	0.2293
	2.4943	-	-
Actual	2.2438	2.3307	0.2290
Average	2.4947	2.3287	0.2293
%error	**11.18**	**-0.09**	**0.13**
NO_2^-	10.7085	10.3474	1.0075
	10.7000	-	-
Actual	9.7988	10.4444	1.0206
Average	10.7043	10.3474	1.0075
%error	**9.24**	**0.94**	**-1.28**
Br^-	8.2079	7.643	0.7337
	8.2113	-	-
Actual	7.3901	7.6877	0.7673
Average	8.2096	7.643	0.7337
%error	**11.09**	**-0.58**	**-4.38**
NO_3^-	8.4083	-	-
	8.4246	-	-
Actual	7.537	-	-
Average	8.4165	-	-
%error	**11.67**	-	-
PO_4^{3-}	12.4801	11.0830	1.1528
	12.5606	-	-
Actual	11.1519	11.2207	1.0846
Average	12.5204	11.0830	1.1528
%error	**12.29**	**-1.23**	**6.29**
SO_4^{2-}	12.9105	12.1758	1.1826
	12.8605	-	-
Actual	11.5329	12.1211	1.1723
Average	12.8855	12.1758	1.1826
%error	**11.73**	**0.45**	**5.85**

D2.2 Precision

The precision of ion chromatography is determined from the analysis of sample replicates and is reported as relative standard deviation (RSD). Calculations were conducted using a spreadsheet program. When duplicate measurements are analyzed, RSD is calculated using the following equation (Skoog et al., 1998):

$$\mathbf{RSD(\%) = 100 * (D/\sqrt{2})/X}$$

Where: **D** = Difference between duplicates

X = Arithmetic mean of duplicate measurements

Table D2.2-1: Precision of ion chromatography for the determination of anions calculated from replicate analyses of fluid inclusion leachates and analytical standards.

Analyte	Run 1 RSD (%)	Run 2 RSD (%)	Run 3 RSD (%)	Run 4 RSD (%)	Run 5 RSD (%)	Run 6 RSD (%)
Cl^-	-21.9	-21.0	-19.0	-20.2	-16.4	-15.2
Br^-	-	-	-	-	-	-18.7

APPENDIX E
CHLORINE ISOTOPES

This section contains the complete chlorine isotope data set for fluid inclusion leachates from Butte, Montana, U.S.A and Bingham Canyon, Utah, U.S.A.

Table E-1: Chlorine Isotope data for Butte, Montana, U.S.A and Bingham Canyon, Utah, U.S.A.

Deposit	Sample	Alteration Zone	Crush	Delta ^{37}Cl (‰)
Butte (Montana)	*CZ-1*	Main Stage	1	-1.3
	AL2	Main Stage	1	-1.1
	X3564	Main Stage	1	-2.0
	11172-3740	potassic	1	-1.3
	11172-1871	potassic	1	-1.0
	11052-7025	pervasive sericitic	1	-1.6
	11052.6215	pervasive sericitic	1	-1.0
	11052.6215	pervasive sericitic	2	-1.6
	Modoc-10649	-	1	-2.2
	Modoc-10649	-	2	-2.3
	11135.4967	potassic	1	-1.0
	11135.4967	potassic	2	-0.6
Bingham Canyon (Utah)	*D152.2655*	intermediate argillic	1	-2.6
	D152.2655	intermediate argillic	2	-5.5
	D162.2991	potassic	1	-3.2
	D415.2829.5	potassic	1	-3.2
	D415.2936	potassic	1	-0.9
	D415.3025	potassic	1	-4.0
	D415.3050	potassic	1	-2.7
	D415.3050	potassic	2	-2.8
	D420.4710	potassic	1	-3.1
	D420.5079.5	potassic	1	-2.6
	D430.3768	potassic	1	-3.4